A Study of the Active Galaxy 3C111 with mm-VLBI

Masterarbeit am Lehrstuhl für Astrononmie
von
Robert Frank Schulz

Fakultät für Physik und Astronomie
Julius-Maximilians-Universität Würzburg

Würzburg, den 30. September 2012

Verantwortlicher Hochschullehrer   Prof. Dr. M. Kadler

Zusammenfassung

Diese Masterarbeit beschäftigt sich mit der Analyse von drei Beobachtungen der aktiven Galaxie 3C111 bei 86 GHz im Oktober 2007 sowie Mai und Oktober 2008. Die Messungen wurden mit dem Global mm-VLBI Array auf Grund eines Flussdichteausbruch Mitte 2007 im mm-Wellenlängenbereich durchgeführt. Das GMVA ist ein Zusammenschluss einzelner Teleskope in Europa und Nordamerika, die zweimal im Jahr Messungen mit Hilfe von *Very Long Baseline Interferomery (VLBI)* vornehmen. Diese Technik ermöglicht die höchste Winkelauflösung, die zur Zeit mit einem astronomischen Messinstrument erreicht werden kann.

Die Radiostrahlung aktiver Galaxienkerne (AGN) ist ein exzellentes Ziel für VLBI Beobachtungen, da es damit möglich ist, detaillierte Einblicke in die innere Struktur von AGNs zu erlangen, um die vorhanden, verschiedenen physikalischen Prozesse zu studieren. AGN unterscheiden sich von normalen Galaxien dahingehend, dass die nicht-thermische Strahlung vom Kern über das gesamte Spektrum hinweg dominiert. Das Standardmodell für AGNs sieht ein supermassives Schwarzes Loch im Zentrum vor, welches umgebende Materie akkretiert, umgeben von einem abschirmenden Torus. Dieser Prozess führt zum Ausstoß hochenergetisch geladener Teilchen, die sich in zwei sogenannten Jets entgegengesetzt vom Kern wegbewegen und Synchrotronstrahlung emittieren..

Der Kern von 3C111 ist der stärkste Emittent von Radiostrahlung bei mm-Wellenlängen von allen FRII Galaxien mit einer Variabilität im Bereich von mehreren Janskys. Auf der pc-Skala zeigt sich ein einseitiger Jet durch *Doppler-Boosting*, dessen Komponenten sich mit scheinbarer Überlichtgeschwindigkeit bewegen. Die geringe Rotverschiebung ($z = 0.049$) von 3C111 und hohe Flussdichte im Radiobereich macht 3C111 zu einem exzellenten Objekt, um die Kinematik und Evolution des Jets mit mm-VLBI unterhalb von 1 pc zu studieren.

Die Kalibration der gesammelten GMVA Daten zeigt den Jet von 3C111 in bisher unerreichter Qualität bei 86 GHz und einer projizierten Auflösung mit bis zu 50 mpc. Die Modellierung des Jets mit kreisförmigen Gauß-Komponenten ermöglicht es die Kinematik einzelner Bereiche genauer zu studieren. Zusätzlich wurden 15 bereits kalibrierte Epochen bei 43 GHz zwischen Juni 2007 und Februar 2009 modelliert, die mit dem Very Long Baseline Array (VLBA) aufgenommenen worden sind. Es ergibt sich ein selbstkonsistentes Model bei 43 und 86 GHz. Ein besonderes Merkmal ist eine komplexes Gebilde im Jet aus mehreren Komponenten, dessen Entstehung mit dem Ausbruch von 2007 assoziiert wurde. Zwar zeigen die 43-GHz-Daten, dass nach 2007 neue Komponenten ausgestoßen worden sind, aber ohne die Bildung einer derartigen Kurve. Darüber hinaus weisen vereinzelte Komponenten bei 43 GHz Beschleunigung entlang des Jets auf.

Abstract

This thesis presents results from an analysis of three 86-GHz observations of the active galaxy 3C111, obtained with the Global mm-VLBI Array (GMVA) in October 2007, May and October 2008 following a major outburst in flux density at mm-wavelenghts. The GMVA is an array of independent telescopes in Europe and North America, which observes twice a year utilising the technique of Very Long Baseline Interferometry (VLBI). VLBI provides the highest spatial resolution of any astronomical instruments available.

The radio emission from active galaxies is a favoured target of VLBI studies. AGN are excellent laboratories for a variety of sometimes even extreme physical processes. They differ from ordinary galaxies such that non-thermal emision dominates the overall spectral properties of the galaxy over the complete electromagnetic spectrum. The standard model of AGN comprises a supermassive black hole in the centre of the nucleus, which accretes matter and is surrounded by an obscuring torus. This leads to the ejection of two plasma streams of charged particles, which emit synchrotron radiation, called jets with opposite orientation to each other.

3C111 contains one of the brightest cores at mm wavelength of all FRII galaxies and variable emission of several Janskys. On pc-scales and below, a one-sided jet is observed due to Doppler-boosting with features moving with an apparent superluminal velocity. Combined with the close proximity 3C111 ($z = 0.049$), it is an excellent object to study the kinematic of its jet with mm-VLBI.

The data gathered with the GMVA is calibrated, yielding images of the source with unprecedented fidelity at this frequency and an projected resolution down to 50 mpc. In order to trace the movement of distinct features in the jet, each epoch is modelled with a set of circular Gaussian components. In addition, 15 self-calibrated epochs at 43 GHz, obtained with the Very Long Baseline Array (VLBA), between June 2007 and February 2009 were modelled as well to constrain the consistency of the 86-GHz kinematic. The jet is resolved into several distinct components and the formation of a bent in the jet stream is associated with the outburst in 2007. The 43-GHz model suggests that acceleration occurs along the jet. Ejection of new material into the jet stream occurred after the 2007 outburst, but the bend seems to be a unique structure caused by the outburst.

Contents

1. Introduction

Scientists and philosophers from every part of our planet have been studying the sky for millennia. While the technological leap in the last few centuries helped to improve our understanding of the Universe rapidly, there is still much more that mankind has yet to discover.

For centuries the only instruments available to astronomers have covered the optical part of the electromagnetic spectrum. It was not until the beginning of the 20th century, that other parts of the spectrum were discovered for astrophysical research.

The primary difficulty in measuring radiation from space one has to overcome is the Earth's atmosphere. While certain radio and optical emission can more or less penetrate the atmosphere and therefore, be detected from ground-based instruments, most of the electromagnetic spectrum cannot. In these cases satellites are necessary. At the highest energies it is nevertheless possible to detect cosmic radiation indirectly on Earth.

The increasing availability of several different instruments at the same time has made it possible to study the properties of astronomical objects not only in one wavelength regime, but over a broad range of frequencies. These extended multi-wavelength campaigns are able to gather their data even simultaneously allowing astronomers to better probe the various underlying physical processes and their connection, thus putting tighter constrain on theoretical models. Additionally, the growing database can be used for long term investigations as well.

One class of objects on which the aforementioned investigations focus are galaxies containing a so-called 'active nucleus'. The properties of these galaxies are predominantly determined by the galactic centre, which can not only shape the inner part but the large scale morphology, as well. A wonderful example is the focus of this thesis and is most commonly known as '3C111'. Although this object has already been observed numerous times, it is a well suited laboratory to test physical models. Thus, its investigation continues and this thesis presents results from high resolution radio observations.

The thesis at hand is structured in the following way: This introduction is succeeded by a chapter on the particularities of active galaxies including an overview on 3C111. Chapter 2 concentrates on the theoretical background of the underlying physical concepts. After elaborating on the utilized observation technique and the methods of data reduction in chapter 4, the subsequent results and an outlook are discussed in chapter 5 and 6 respectively.

1.1. Radio Astronomy

The discovery of radio emission for astronomical research began with Karl Jansky (1933) who was at that time an employee of a north-american telecommunications company. His actual task was to study the capability of transatlantic communication at meter-wavelength (14.6 m). However, Jansky's measurements revealed radiation that was not of terrestrial, but of interstellar origin. In addition the emission from the Milky Way would not have been possible to detect if the observations had not coincided with a minimum of solar activity. Usually, signals at this long wavelength are heavily disturbed by the Earth's ionosphere under the influence of solar radiation. Jansky's discovery is a wonderful example how a scientific breakthrough took place outside the scientific community.

Not long after Jansky's pioneering results it fell to an radio engineer for the next major step. Grote Reber built his own radio antenna in his backyard in 1937 and started to measure the sky at 160 MHz. This lead to the release of the first radio sky map, proving that stars are not the dominant source for radio emission. For a more personal summary of these early events see Reber (1988). Exemplary, Fig. 1.1 pictures an allsky map at 408 MHz based on Haslam et al. (1982) with data taken from observations with the Effelsberg, Jordrell-Banks and Parks antennas. The bright Galactic centre is clearly visible as well as other sources such as the active galaxy Cygnus A and the supernovae remnant Cassiopeia A.

Further major advances were the detection of the cosmic microwave background by Penzias & Wilson (1965) in 1965 as well the discovery of the first pulsar in 1967 by Hewish et al. (1968). These advances established observations in the radio regime as one of the backbones of astronomy equally complementing observations at other parts of the electromagnetic spectrum.

Though, to this date radio astronomy achieves the highest resolution in astronomy via the technique of Very Long Baseline Interferometry (see Chapt. 4), used by e.g the Very Long Baseline Array (VLBA), European VLBI Network (EVN) and the Global mm-VLBI Array (GMVA). While these arrays are not directly connected a variety of interconnected arrays exist, are in construction or planning such as the Expanded Very Large Array (VLA), the Atacama Large Millimetre/submillimetre Array or the Square Kilometre Array (SKA). Nevertheless, single-dish observations continue to play a crucial role.
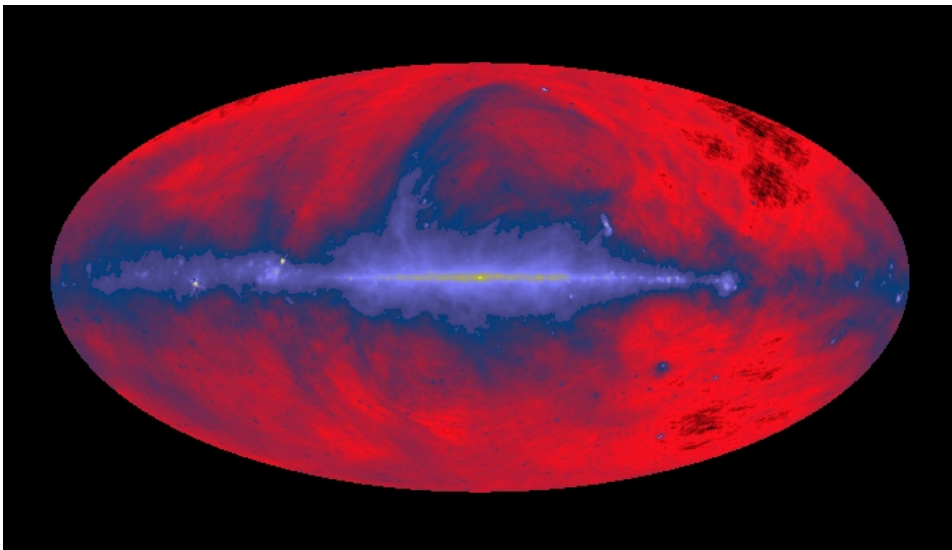
Figure 1.1.: Allsky survey at 408 MHz conducted by telescopes in Effelsberg, Jordrell-Banks and Parks. The map shows the bright Galactic centre, radio galaxies, pulsars and supernovae remnants. Credit: Haslam et. al, MPIfR, SkyView

2. Active Galactic Nuclei

The term *active galactic nucleus* (AGN) refers to one of the most extraordinary classes of astronomical objects, which will be reviewed in the following sections. AGN is the central region of a galaxy, but outshines its host over the complete electromagnetic spectrum. The appearances of AGN can be very diverse, but common features exists. After summarising the major classes, in which AGN are distinguished, the general properties as well as the unification of these classes are discussed. Unless otherwise mentioned the necessary information was taken from textbooks by Longair (2011), Krolik (1999) and Schneider (2008). For an historic overview of the research on AGN see Shields (1999). This chapter concludes with a presentation of the fascinating source 3C111 which is the center of attention in this thesis.

2.1. Types of AGN

The different types of AGN are above all based on their observational properties and especially on the spectral range (mostly optical or radio), in which they were first discovered. In addition, the information gained from observation are almost always biased either by condition of the selected sample or the capabilities of the instruments.

Quasars

The term quasar is short for *quasi-stellar radio source*. These objects were detected by radio surveys of the sky and could be associated with an optical point sources. Their optical properties revealed strong and broad emission lines, which were not typical for ordinary galaxies and at this time a redshift of unprecedented scale. However, until the 1960s the angular resolution of radio instruments was worse than their optical counterparts, which complicated the identification of these sources. 3C273 was the first quasar for which its redshift was determined to be $z = 0.156$ (Schmidt 1963). While quasars were detected first in the radio regime, objects initially identified with optical measurements due to weak radio emission were classified as *quasi-stellar objects* (QSOs). The difference between QSOs and quasars is primarily historic and now QSOs are more commonly refer to as *radio-quiet* quasars.

Seyfert Galaxies

Carl Seyfert (1943) examined optical data of a group of galaxies, which contained a bright quasi-stellar point-like nucleus. Their spectra revealed broad permitted and forbidden lines implying unusually high Doppler shifts compared to ordinary galaxies. Khachikyan & Weedman (1971) divided the group of the so-called Seyfert galaxies into two subclasses, based on the spectral properties of these galaxies. While *Seyfert 1* galaxies possess broad permitted lines and narrow forbidden lines, *Seyfert 2* galaxies show only narrow lines and weaker continuum emission compared to Seyfert 1. The distinction between Seyfert 1 galaxies and radio-quiet quasars is usually based on the detectability of a host galaxy, which is however independent of the object itself, but rather caused by the instrument in use. Further subdivision in intermediate classes has become necessary due to the availability of more data and larger samples. In the radio regime Seyfert galaxies show usually only weak emission, but radio-loud Seyfert 1 galaxies have been found with only weak broad line features classified as *radio-loud narrow line Seyfert 1* (RL-NLS1, see e.g. (Komossa et al. 2006)). Recently four RL-NLS1 have been discovered by Fermi/LAT to exhibit γ-ray emission ((Abdo et al. 2009a,b)).

Radio Galaxies

Radio galaxy show strong radio emission from the nucleus, which can be up to a few orders of magnitude higher, than the flux from the host galaxy. The closest AGN, Centaurus A, is often cited as a prototype for this class and it was among the first radio sources to be associated with an optical counterpart (Bolton et al. 1949). Radio galaxies can be viewed as a *radio-loud* version of Seyfert galaxies. They are generally divided into *broad line radio galaxies* (BLRG) and *narrow line radio galaxies* (NLRG). Their optical luminosity and extended radio emission up to several kpc from the nucleus distinguish radio galaxies from quasars.

While the differentiation in BLRG and NLRG is based on the optical spectra, the extended radio morphology, was taken as an initial point by Fanaroff & Riley (1974) to define two classes: *Fanaroff-Riley Typ 1* (FR1) galaxies feature a dominating, bright core, with two *jets* (see Subsect. 2.2.3) extending from either side of the core. The luminosity decreases along the jets with increasing distance. Radio galaxies with dominating lobes, usually only a single-sided visible, but weak jet and a less prominent core are referred to as *Fanaroff-Riley Typ 2* (FR2). Their overall luminosity increases with distance from the core. It is important to note that extended radio emissions in this case denote scales from kpc up to Mpc, though even sub-pc scales are resolvable with modern radio interferometry (see Sect. 3.3).

Blazars

Blazars were found to be compact radio sources as well as emitters up to the highest detectable energies, exhibiting strong variability. A distinction is made in *BL Lac* and

optically, violently variable object (OVV) for historic reasons. The former class is named after its prototype BL-Lacertae, which was initially labelled as a variable star, but was found to be a strong radio emitter. The broad band spectrum from radio to X-ray of these sources reveals almost no emission lines. OVV objects are highly variable objects as well, but exhibit broad emission lines. Both types have in common their strong polarized optical emission and the fact that BL Lac objects can contain weak emission lines.

2.2. General Properties of AGN

In order ot explain the diversity of AGNs it is necessary to identify key pieces and look for individual properties which can be used as global physical parameters.

2.2.1. The Central Engine

One of the most important questions about AGN concerns the source of their emitted energy. While the black hole paradigm was not the only one considered, it currently fits best the observed properties and is thus commonly preferred among astrophysicists. In this picture the strong gravitational potential attracts surrounding matter and forces the generation of an accretion disc, in which matter is transported inwards while angular momentum is transported outwards due to the viscosity of the medium. Once a particle reaches the innermost stable orbit, it is accreted into the black hole. The process leads to the generation of a disk of matter called *accretion disk*, in which viscous forces optical and X-ray emission thus cooling the accretion flow.

It raises the question of efficiency for matter to energy conversion. As a matter of fact, the most efficient process is the accretion of matter onto a source of strong gravitation. That alone implies compact objects like neutron stars besides black holes. However, the maximum luminosity, which can be emitted from an object with mass M in equilibrium with radiation pressure and in-falling matter gives an upper limit known as the *Eddington limit*: $L_{Edd} = 1.3 \cdot 10^{38} \frac{M}{M_\odot} \, \mathrm{erg\,s^{-1}}$ (Longair 2011). An assumed luminosity of $10^{46} \, \mathrm{erg\,s^{-1}}$ yields a central mass $10^8 \, \mathrm{M_\odot}$. Furthermore, the variability of AGN places a lower limit on the size of the emission region. Since the smallest size an object of mass M can take up is the Schwarzschild radius, it follows: $t \gtrsim 10^{-5} \frac{M}{M_\odot} s$ Longair (2011, chap. 19.2). However, both arguments do not include relativistic beaming of emission, which has to be considered especially in radio-loud AGN. Nevertheless, it shows the possibility of a *supermassive black holes* (SMBH) in the centre of these galaxies, which show similar characteristics to compact stellar systems, such as X-ray binaries (see e.g. (Marscher 2006)).

Following these conclusions even non-active galaxies may harbour a SMBH in their midst. The best opportunity to investigate it is given by our own Galactic centre known as Sagittarius A* (Sgr A*). In the infrared band the movement of stars around Sgr A*

was studied and the derived velocity dispersion were evidence of a SMBH ((Eckart & Genzel 1996; Ghez et al. 2000)). High-resolution VLBI at a wavelength of 1.3 mm enabled Doeleman et al. (2008) to determine the local size of Sgr A* at an impressive μas-scale.

Although accretion can be the most efficient way, it does not necessarily has to be. In the case of *advection dominated accretion flows* (ADAFs) the non-existing solid surface of a black hole can lead to an accretion rate, which exceeds the Eddington limit. However, this results in a low efficiency, i.e. only weak emission.

2.2.2. The Surroundings of the SMBH

The continuum spectrum of an ordinary galaxy is primarily defined by the accumulated stellar emission from. In contrast to that AGN show a continuum spectrum, which is to a high degree non-thermal. A peculiar peak in the optical/ultraviolet band can come from thermal emission from the accretion disk close to the black hole and is called the *big blue bump*, but is not always visible.

While moving away from the SMBH and its accretion disk, one crosses three important regions with decreasing particle density - the *broad line region* (BLR), the *torus* and the *narrow line region* (NLR). Their occurrence is the result of the gravitational potential of the SMBH binding surrounding gas clouds. The spectrum of the BLR and NLR reveal emission lines, usually observed in the optical and ultraviolet band, which are believed to be predominantly caused by *photo-ionization* by the continuum emission of the AGN itself. One major challenge, which has to be overcome, in order to analyse the observed line profiles from the BLR as well as the NLR is dust extinction along the line of sight, e.g. caused by our Galaxy and/or intrinsic to the AGN.

The Broad Line Region is a hot and very dense medium, which prevents the production of narrow forbidden lines. Thus, it lies closest to the nucleus following the accretion disc at a scale of $\sim$0.1 pc to 1 pc. The matter accumulated in this space has to be concentrated in clouds, because for a uniform medium *Thomson scattering* would make it optically thick for our observations. The broadening of the lines is thought to be the result of turbulent motion of the clouds as well as their high rotational velocity. Line width of $\mathcal{O}(1000\,\mathrm{km\,s^{-1}})$ are not unusual. Their variability indicates further that their emission region is close to the SMBH.

The Narrow Line Region exhibit narrow, but strong permitted as well as narrow forbidden lines of the order of $\mathcal{O}(100\,\mathrm{km\,s^{-1}})$. Therefore, it is a colder and less dense accumulation of gas clouds compared to the BLR. The NLR can extend from $\sim$100 pc up to several kpc. Especially for galaxies, in which the dimensions of the NLR reaches out this far *shock excitation* has to be considered to explain the observed line profiles.
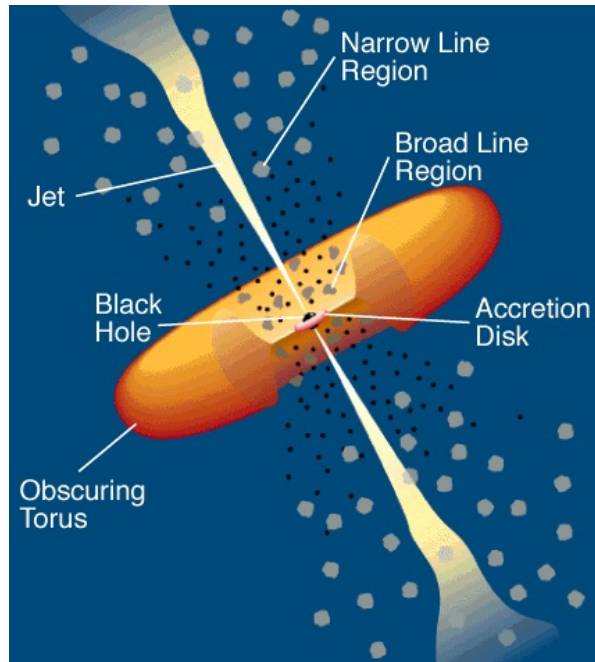
Figure 2.1.: Illustration of the different parts of a generic radio-loud AGN. In radio-quiet AGN the jet is usually missing, Credit: C.M. Urry and P. Padovani

2.2.3. The Jet(s) and Radio Lobes

One of the most spectacular attributes associated with radio-loud AGN on sub-pc and kpc scales is a highly relativistic and collimated outflow of particles from the nucleus, known as *jet*. As already indicated in Sect. 2.1, one-sided and two-sided systems are observed in AGN. AGNs with no jet classified as radio-quiet. It is, however, assumed that the twin-jet paradigm is valid for all AGN with the jet strength varying due to relativistic beaming (Subsect. 3.2.2). When interacting with the inter-galactic medium, the flow is considerably inhibited, producing lobes on either side. These lobes are not the result of a single event, but are probably constantly fuelled by the jet. For an account of the theoretical concept behind the production of jets see Sect. 3.2.

2.2.4. A Unified Model

Although a variety of observational quantities as well as a growing database exist, there are still not enough AGN explored and discovered to reach statistical significant conclusions on the unification of AGN. A major challenge in this matter is the diversity of instruments necessary to cover the electromagnetic spectrum. Hence, the quality of the data differs significantly, e.g. sensitivity, angular resolution. A complete discussion is beyond the scope of this thesis and in this case the above mentioned textbooks as

well as reviews specific to AGN unification by Antonucci (1993) and Miller (1994) can be recommended. In general the unification scheme assumes all AGN are similar the different appearances and spectra can be explained with the geometry of the AGN and its viewing angle towards the observer.

The sample of AGN can be divided in radio-loud and radio-quiet based on the strength of radio emission. The latter group mainly comprises Seyfert 1 and 2 galaxies. After observing the spectrum of the Seyfert 2 galaxy NGC 1068 Antonucci & Miller (1985) implied a connection with Seyfert 1 galaxies. A basic interpretation incorporates our viewing angle to the galaxy. Looking from the side, the torus prevents the detection lines from the BLR. Whereas, a more face on view permits the observation of strong narrow lines from the NLR as well as a look into the BLR inside the torus.

In radio-loud AGN the amplification of the received emission by means of *relativistic beaming* (see Subsect. 3.2.2) has to be taken into account. This effect depends on the position angle of the jet in respect to us. Therefore, it is a possible explanation for *superluminal motion* observed in a few low-angle AGN jets (see Subsect. 3.2.2). This interpretation can explain the different radio morphologies in FR1- and FR2-type AGN probably only to some extend. Doppler-boosting of emission from the jet oriented toward us and de-boosting of the counter-jet respectively is not as important on large scales, where deceleration effects may dominate. Depolarization, i.e. the reduction of the detected amount of polarization, of radio-lobes associated with the jet closer to us is smaller than on the weaker counter-jet side facing away from us due to the increased path length. Thus, the position angle of the jet is still important. The optical distinction in broad and narrow line radio galaxy (BLRG, NLRG) is caused by observing the galaxy somewhere between the direction of the jet and the torus, thus minimising the shielding of the torus from the BLR or completely from the side respectively. When we change the angle again in a way that we look from above almost directly into the jet and the central engine, we would be able to include Blazars in our unified model. Their strong and variable radio emission is probably due to beaming effects with additional strong continuum emission with no lines, but high polarization in the optical and radio band. It is necessary to remember that polarization studies at radio and optical frequencies play an important role in the unification process, but they are complicated by other effects beside orientation. For example, it is sometimes possible to explain depolarization by the passing of polarized emission through certain media along the line of sight.

2.3. Presenting 3C111

Since the 1960s various publications focusing either solely on 3C111 or as part of a sample have been published. This section presents a selection of results from the beginning of the study of 3C111 up to now, without claiming to be complete.
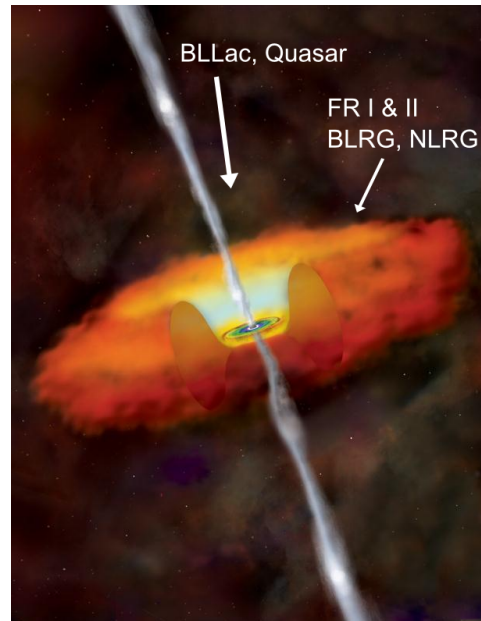
Figure 2.2.: Illustration of a radio-loud AGN (Credit: NASA/CXC/M.Weiss) with labels indicating how the various radio-loud AGN are connected with each other.
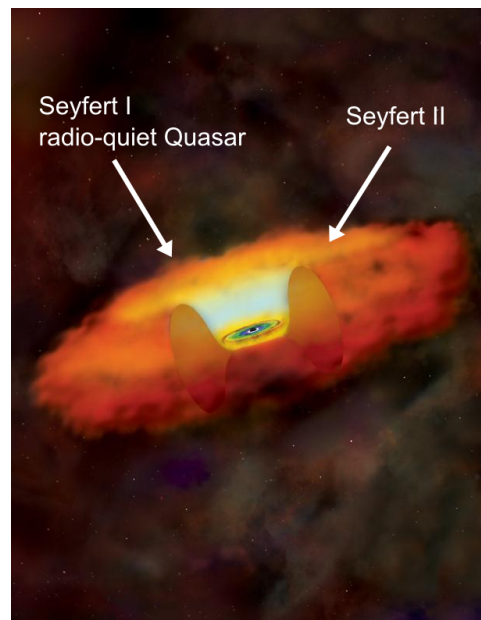

Figure 2.3.: Illustration of a radio-quiet AGN (Credit: NASA/CXC/M.Weiss) with labels indicating the relationship between different types

2.3.1. Early Studies of 3C111

3C111 it the 111th source in the 3rd Cambridge catalog Bennett (1962). Its coordinates[1] are given by RA=04h18m, DEC=38d01m (J2000). Early radio synthesis imaging at cm-wavelengths such as Mackay (1969) and Mitton (1970) revealed a triple structure with a prominent central component and bright north and south hotspots.

However, the optical association proved to be difficult. Although Wyndham (1966) reported a heavily obscured image, Longair & Gunn (1975) described the centre of 3C111 as "almost star-like". Following optical observations in the early 1970s between 450 nm and 750 nm by Sargent (1977) the redshift of 3C111 was determined to $z = 0.0485$ with a Seyfert 1 kind of spectrum. Ground based CCD observations ((Colina & Perez-Fournon 1990)) and early HST images by Martel et al. (1999) still were unsuccessful in gaining more structural information on the host galaxy besides establishing an elliptical configuration.

At higher energies Marshall et al. (1978) reported the first confident association of 3C111 with an X-ray source based on the first full-sky survey of the HEAO-1 satellite. Several X-ray observations were conducted in the following ranging from low to high keV with different satellites to model the spectrum. For a review on this matter see e.g. Reynolds et al. (1998) and Wozniak et al. (1998) with references therein. Especially the existence and shape of an Kα line has been subjected to an ongoing debate.

Early cm VLBI observation such as Pauliny-Toth et al. (1976) found that the centre can be decomposed into multiple components at the pc-scale. The next advancement in the study of the nucleus of 3C111 came with reports on superluminal motion of features in the radio jet ((Götz et al. 1987; Linfield 1987; Preuss et al. 1988)). This makes 3C111 one of the first AGN in which this effect was discovered.

Observations to determine polarization and rotation measure properties on the large scale structure began in 1978 ((Hogbom 1979)) and were deepened with VLA data in the 1980s (see (Linfield & Perley 1984; Leahy et al. 1997)). From these observations the VLA image by Leahy et al. (1997) at 3.6 cm remains to date the best map at kpc-scale (see Fig. 2.4). Linfield (1987) was one of the first to use the Fanaroff-Riley type II classification on 3C111.

In the mm-regime Wills (1975) was the first to show evidence for strong emission from the central component of the triple structure and its surprising strength being several orders of magnitude stronger than the nucleus of Cen A, but at even greater distance. Therefore, it was only logical to include 3C111 in the sample of AGN, which took part in an early global 86 GHz VLBI campaign in 1993, yielding the highest resolution image up until then ((Rantakyro et al. 1998)).

---

[1]taken from the NASA/IPAC Extragalactic Database (NED): http://ned.ipac.caltech.edu/
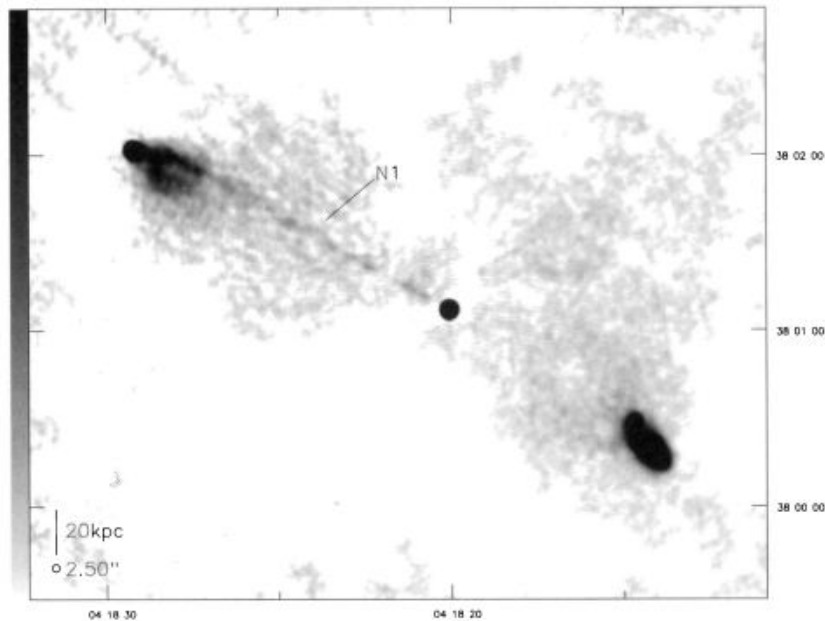
Figure 2.4.: Contour map of 3C111 at 3.6 cm obtained with the VLA from Leahy et al. (1997)

2.3.2. Recent Studies of 3C111

The modern exploration of 3C111 was shaped by a major flux density outburst above 10 Jy in January 1996 ((Alef et al. 1998)). The author's VLBA+Effelsberg observations at 7 mm in July and September 1996 revealed a significant evolution of the jet, which could not be explained simply by the motion of components. These changes were confirmed by Kharb et al. (2003), who observed the source at roughly the same time though with the VLBA at 43 GHz and 8.4 GHz, while analysing changes in the polarisation of the core and a jet component.

Jorstad et al. (2005) conducted the first densely sampled multi-epoch campaign for 3C111 at 7 mm as part of their bi-monthly polarimetric monitoring of 15 AGN with the VLBA and additional quasi-simultaneous 3 mm BIMA, 1.3 mm and 0.85 mm JCMT as well as optical measurements. Although their study was carried out between March 1998 and September 2001, the most prominent feature in the jet of 3C111 was still associated with the 1996 outburst. In addition, they suggested that acceleration of components moving away from the core takes place, because the derived time of ejection of this feature does not coincide with the earlier report of Alef et al. (1998). Moreover, stationary components close to the core as well as evidence of forward-and-reverse shocks were found. The latter has been predicted by hydrodynamical simulations ((Aloy et al. 2003)). At 86 GHz Lee et al. (2008) carried out a survey of compact radio source with the predecessor to the Global mm-VLBI Array obtaining snapshot images of 3C111.

At lower frequency 3C111 was subjected to long term monitoring as part of the VLBA 2 cm Survey and Mojave program resulting in observations ranging over one decade from Spring 1995 to Fall 2005 ((Kadler et al. 2008)). This study was able to trace the influence of the ejected material in 1996 on the evolution of the jet morphology basically over the complete time range, confirming the splitting of this feature into leading and trailing components as already reported by Jorstad et al. (2005). Furthermore, Perucho et al. (2008) used one-dimensional hydrodynamical simulations to model the forward and reverse shock based on the injection of a square perturbation followed by rarefied material into an otherwise steady jet. The latter leads to a separation of a primary component from a trailing component due to the rarefaction in-between. The results were in agreement with the observed behaviour. In addition, Kadler et al. (2008) discussed thoroughly different zones within jet showing that interaction with the ambient medium shapes the morphology a great deal and the existence of a Faraday screen has to be considered to explain the detected changes in the EVPA. This coincides with a study by Lewis et al. (2005) in the X-ray regime, who considered 3C111 to be partially covered by an absorber to explain large column densities derived from simultaneous RXTE and XMM-Newton data.

In July 2007 the last major flux density at millimeter wavelengths occurred with an increase in radio flux density above 10 Jy ((Trippe et al. 2011),(Kadler et al. 2007)). This outburst was the crucial factor for the observational data, analysed in this thesis. Grossberger et al. (2012) analysed data from the Mojave monitoring program at 2 cm with the VLBA and confirmed the ejection of a bright feature which split up into a leading and multiple trailing components.

While 3C111 was well established as an X-ray emitter the question remained, whether it is a source for γ-rays, as well. A first evaluation of data from the 3rd EGRET Catalog (3EG) by Hartman et al. (1999) reported an association with the EGRET Source 3EG J0416+3650 to be unlikely based on the confidence level of the positional offset. A multiwavelength campaign by Sguera et al. (2005) revised the EGRET data and searched for other possible sources within the error box of 3EG J0416+3650, but found 3C111 to be the most likely candidate. Moreover, they compiled the first non-simultaneous *spectral energy distribution* (SED) for 3C111 showing a blazar-like distribution of the collected data. In a further re-analysis of the EGRET data Hartman et al. (2008) decomposed 3EG J0416+03650 into at least three variable components, of which one was detected above 1 GEV and could be associated with 3C111, while the others were far more unlikely. In addition, a SED was compiled using non-simultaneous data and the revised EGRET data confirming the blazar-like nature of 3C111 (Fig. 2.5), which is supported by the low angle to the line of sight of $(18.1 \pm 5.0)°$ (Jorstad et al. 2005). In the context of the AGN unification scheme these results can be interpreted as 3C111 to be a an intermediate source between blazars and radio galaxies.

An important step in ascertaining γ-ray emission from AGN was the launch of the Fermi γ-ray satellite, which constantly monitors the sky with its Large Area Telescope (LAT) since 2008. Although 3C111 was included in the first Fermi/LAT catalogue
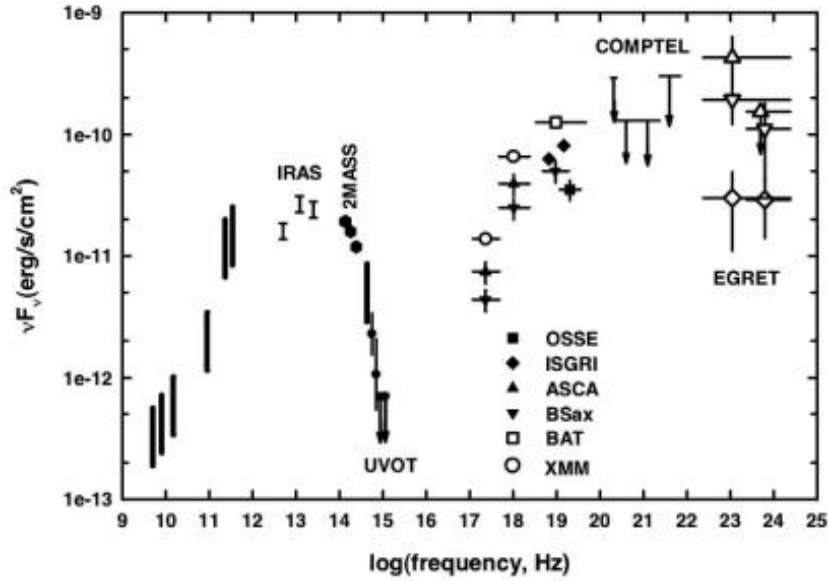
Figure 2.5.: Non-Simultaneous SED of 3C111 from Hartman et al. (2008), revealing a blazar-like distribution

((Abdo et al. 2010)), it was missing in the second ((Nolan et al. 2012)). Kataoka et al. (2011) analysed 3C111 as part of a sample of broad line radio galaxies using two years of Ferm-LAT data. Applying a binning of three month at an energy range above 100 MeV resulted in only three detections and five upper limits. Grandi et al. (2012) decreased the data binning to two months resulting in only one detection in September-November 2008, which coincided with an increase in millimetre, optical and X-ray flux. In combination with 43 GHz VLBA data they suggested that the emission region is located 0.3 pc away from the black hole and contained in a region within 0.1 pc. Their analysis of the radio data required a technique called *super-resolution* to resolve components in the jet.

In an earlier paper Chatterjee et al. (2011) reported a correlation of emission from the radio jet and the accretion disk based on optical, X-ray, multi-frequency radio flux measurements as well as 43 GHz VLBA monitoring between 2004 and 2010. Ejection of new material into the jet stream succeeded a dip in the X-ray light curve. Furthermore, the distance between the production site of the X-ray emission and the core region at 43 GHz was calculated to ∼0.6 pc and the mass of the central black hole was deduced to $m_{BH} = 1.8^{+0.5}_{-0.4} \times 10^8 M_\odot$. The disk-jet connection for 3C111 was previously suggested in a paper by Marscher (2006). Both studies sought out similarities of their results with the FR I galaxy 3C120 and Galactic BHXRBs. Tombesi et al. (2012) compared ultra fast outflow of X-ray emission from the accretion disk with VLBA data at 43 GHz between 2010 and 2012.

3. Theoretical Background

In order to properly interpret observational results it is essential to be familiar with the necessary physical concepts. Therefore, this chapter deals first with different kinds of radiation emitted by accelerated charged particles, followed by a discussion of the processes related to extragalactic jets and the spectral energy distribution of AGN. It becomes apparent that the physics of active galaxies is widespread from non-relativistic electrodynamics to general relativity due to the different building blocks of these objects (see Chapt. 2). Hence, astronomers and (theoretical) astrophysicists have in part specialised on certain aspects. Nevertheless it is required to be acquainted with at least the general basics.

This chapter is intended as a selective review of the most important concepts rather than a complete treatment, for which case one should refer to textbooks such as Rybicki & Lightman (1979), Krolik (1999) and Longair (2011).

3.1. Radiation of Charged Particles

If a charged particle is accelerated, it will radiate a certain amount of energy related to the acceleration process. This can happen under the influence of a magnetic field, i.e. cyclotron or synchrotron radiation or through interaction with other particles leading to bremsstrahlung. The former plays a vital role especially in the relativistic case in the emission from radio jets and the overall energy output of AGN. The latter has to be considered for example in X-ray production.

Consider a particle with charge q stationary at the origin of an arbitrary inertial frame of reference undergoing minor acceleration $\ddot{\mathbf{r}}$, i.e. to non-relativistic velocities. The resulting emitted energy per time through the area $r^2 \, \mathrm{d}\Omega$ at angle θ and at distance r yields:

$$\left(-\frac{\mathrm{d}E}{\mathrm{d}t}\right)_S = \int\limits_0^\infty \frac{q^2 |\ddot{\mathbf{r}}|^2 \sin^2\theta}{16\pi^2 \epsilon_0 c^3} \, \mathrm{d}\Omega = \int\limits_0^\pi \frac{q^2 |\ddot{\mathbf{r}}|^2 \sin^2\theta}{16\pi^2 \epsilon_0 c^3} 2\pi \sin\theta \, \mathrm{d}\theta \qquad (3.1.1)$$

$$\Rightarrow \left(-\frac{\mathrm{d}E}{\mathrm{d}t}\right)_S = \frac{q^2 |\ddot{\mathbf{r}}|^2}{6\pi \epsilon_0 c^3} \qquad (3.1.2)$$

where ϵ_0 denotes the electric constant, c the speed of light. Eq. 3.1.2 is known as *Larmor's* formula. One can also define $q|\ddot{\mathbf{r}}|$ as the electric dipole moment. Because the loss

rate per unit solid angle depends on $\sin^2 \theta$, no radiation is emitted along the acceleration vector. Furthermore, the emitted electromagnetic waves are polarized.

To derive the spectrum of the particle in terms of energy per unit time and unit bandwidth of the particle one can use the Fourier transform of the acceleration and Parseval's theorem, leading to the expression:

$$\frac{\mathrm{d}E(\omega)}{\mathrm{d}t\,\mathrm{d}\omega} = \frac{q^2}{3\pi\epsilon_0 c^3}|\ddot{\mathbf{r}}(\omega)|^2 \tag{3.1.3}$$

In order to calculate the spectrum from a sample of particles, it is necessary to integrate 3.1.3 over the whole distribution.

Lamor's formula needs adjustment to describe the radiation pattern from charged particles moving at relativistic velocities. Let the observer's reference frame be S and the particles instantaneous rest frame be S', for which Eq. 3.1.2 still holds. A Lorentz transformation is applied to the acceleration four-vector of the particle, whereas the energy rate is Lorentz invariant:

$$\left(\frac{\mathrm{d}E}{\mathrm{d}t}\right)_S = \left(\frac{\mathrm{d}E'}{\mathrm{d}t'}\right)_{S'} = \frac{q^2\gamma^4}{6\pi\epsilon_0 c^3}\left(|\ddot{r}_\perp|^2 + \gamma^2|\ddot{r}_\parallel|^2\right) \tag{3.1.4}$$

where $\gamma = (1 - v^2/c^2)^{-1/2}$ and the acceleration vector $\ddot{\mathbf{r}}$ is separated into a parallel $\ddot{\mathbf{r}}_\parallel$ and perpendicular $\ddot{\mathbf{r}}_\perp$ component.

3.1.1. Bremsstrahlung

Bremsstrahlung or free-free emission corresponds to radiation emitted by a charged particle being accelerated in the presence of a Coulomb-field, e.q. from a nucleus or other particle. A classical approach to this problem can be taken, but for the full derivation quantum mechanical corrections are necessary. These are usually incorporated in the *Gaunt* factor, which is a function of the energy of the electron and the frequency of the radiation.

Let n_e be the density of an electron distribution, moving non-relativistically at a fixed velocity v and an ion density n_i with an ion charge of Ze. Assuming small angle scattering and the low-frequency range, the energy loss per unit time, volume and bandwidth can be expressed as:

$$\frac{\mathrm{d}E}{\mathrm{d}t\,\mathrm{d}V\,\mathrm{d}\omega} \propto n_e n_i Z^2 g_{ff}(v,\omega) \tag{3.1.5}$$

where $g_{ff}(v,\omega)$ is known as the *Gaunt factor*. In order to evaluate the emissivity from thermal bremsstrahlung, i.e. bremsstrahlung from a Maxwellian velocity distribution at temperature T, we have to integrate Eq. 3.1.5 over the velocity distribution, which we

take to be isotropic:

$$\frac{\mathrm{d}E}{\mathrm{d}t\,\mathrm{d}V\,\mathrm{d}\omega} \propto Z^2 n_e n_i T^{-1/2} \exp\left(-\frac{h\nu}{kT}\right) \bar{g_{ff}} \tag{3.1.6}$$

where $\bar{g_{ff}}$ denominates the velocity averaged Gaunt factor. Integrating Eq. 3.1.6 over the appropriate frequency range results in:

$$\frac{\mathrm{d}E}{\mathrm{d}t\,\mathrm{d}V} \propto Z^2 n_e n_i T^{1/2} \bar{g_B} \tag{3.1.7}$$

where $\bar{g_B}$ is the frequency average of $\bar{g_{ff}}$. If one deals with relativistic electrons a correction factor of the form $(1 + \mathrm{const.} \times T)$ has to be applied to Eq. 3.1.7 in the low frequency limit. At high frequencies Klein-Nishina corrections are necessary.

Free-free absorption due to thermal bremsstrahlung can be of importance for example if the absorption is caused by the torus of an AGN. In the Rayleigh-Jeans approximation, i.e. at low frequencies, the Planck distribution in the absorption coefficient is reduced to

$$\alpha_\nu^{ff} \propto T^{-3/2} Z^2 n_e n_i \nu^{-2} \bar{g_{ff}} \tag{3.1.8}$$

showing a ν^{-2} dependence on the frequency.

3.1.2. Synchrotron Radiation

The detection of synchrotron emission represents a fundamental way for us to study active galaxies. It is produced by relativistic charged particles moving in a magnetic field $\mathbf{B}$ under the influence of the Lorentz force. The *gyrofrequency* ν_g of e.g. an electron, which spirals around the field lines of a uniform magnetic field from, is described by:

$$\frac{\mathrm{d}}{\mathrm{d}t}(\gamma m_e)\mathbf{v} = e(\mathbf{v} \times \mathbf{B}) \tag{3.1.9}$$

$$\Rightarrow \nu_g = \frac{e|\mathbf{B}|}{2\pi\gamma m_e} \tag{3.1.10}$$

where m_e is the mass and e the elementary charge of the electron. ν_g can be approximated to $\nu_g = 28\gamma^{-1}\,\mathrm{GHz\,T^{-1}}$. Using Eq. 3.1.4 together with Eq. 3.1.9 the energy loss yields:

$$-\left(\frac{\mathrm{d}E}{\mathrm{d}t}\right) = 2\sigma_T c\frac{B^2\gamma^2\sin^2\alpha}{2\mu_0}\left(\frac{v}{c}\right)^2\gamma^2\sin^2\alpha \tag{3.1.11}$$

where $\sigma_T = \frac{e^4}{6\pi\epsilon_0^2 m_e^2 c^4}$ denotes the Thompson cross section. The pitch angle α can be assumed to be randomised, thus isotropically distributed, for a sample of electrons, in

which case the pitch angle averaged loss rate yields:

$$-\left(\frac{\mathrm{d}E}{\mathrm{d}t}\right)_{\text{Sync}} = \frac{4}{3}\sigma_T c \frac{B^2\gamma^2\sin^2\alpha}{2\mu_0}\left(\frac{v}{c}\right)^2\gamma^2 \tag{3.1.12}$$

An important effect of emission from accelerated relativistic particles is called *beaming* caused by relativistic aberration between the laboratory rest frame (us, the observer) and the instantaneous rest frame of the particle. Recall the circumstances of Eq. 3.1.2, in which the intensity in the particle's rest frame S' scales with $\sin^2\theta' = \cos^2\phi'$ relative to the acceleration vector and the velocity vector respectively (Fig. 3.1a). Thus half of the intensity's maximum value comes from within $-\frac{\pi}{4} < \phi' < \frac{\pi}{4}$. The transformation into the laboratory frame results in a strongly elongated dipole pattern in the direction of motion with a significant amount of radiation coming from within a cone of $-\gamma^{-1} < \phi < \gamma^{-1}$ for $\gamma \gg 1$ (Fig. 3.1b). Now we can estimate the maximum Fourier component of the resulting spectrum based on the duration of the pulse. It follows that the gyrofrequency for arbitrary pitch angle α is shifted such

$$\nu_c \propto \gamma^2\nu_g\sin\alpha \tag{3.1.13}$$

where ν_c is referred to as the critical frequency for synchrotron radiation.

Until now we considered only one electron, but usually a distribution of electrons for example in a jet causes synchrotron radiation. To evaluate the spectral distribution it is often possible to approximate the electron population with a power-law

$$N(E)\,\mathrm{d}E = CE^{-p}\mathrm{d}E \tag{3.1.14}$$

where $N(E)dE$ represents the number of particles per unit volume with energy from E to $E + \mathrm{d}E$ and p the *particle distribution index*. Skipping a rather long derivation the key parameters of emissivity, i.e. the energy per unit time, bandwidth and volume finally is found to be described by:

$$\frac{\mathrm{d}E}{\mathrm{d}t\,\mathrm{d}\nu\,\mathrm{d}V} \propto B^{\frac{p+1}{2}}\nu^{-\frac{p-1}{2}} = B^{\alpha+1}\nu^{-\alpha} \tag{3.1.15}$$

with the *spectral index* $\alpha = -\frac{p-1}{2}$ and $B=|\mathbf{B}|$. Integrating Eq. 3.1.15 along the line of sight leads to the actual observable, the spectral flux density F_ν, which in the radio regime is given in units of *Jansky*, where $1\,\mathrm{Jy} = 10^{-26}\,\mathrm{J\,s^{-1}\,m^{-2}\,Hz^{-1}}$.

A prominent feature of synchrotron emission is its intrinsic polarization, which depends on the position of the observer with respect to the orientation of the magnetic field. Due to the pitch angle dependence the emission from a single particle is in general elliptically polarized. However, for a distribution of particles with varying pitch angle the net polarisation is almost completely linear. Therefore, we define the fractional polarization Γ to be the ratio of the difference of the emissivity parallel and perpendic-
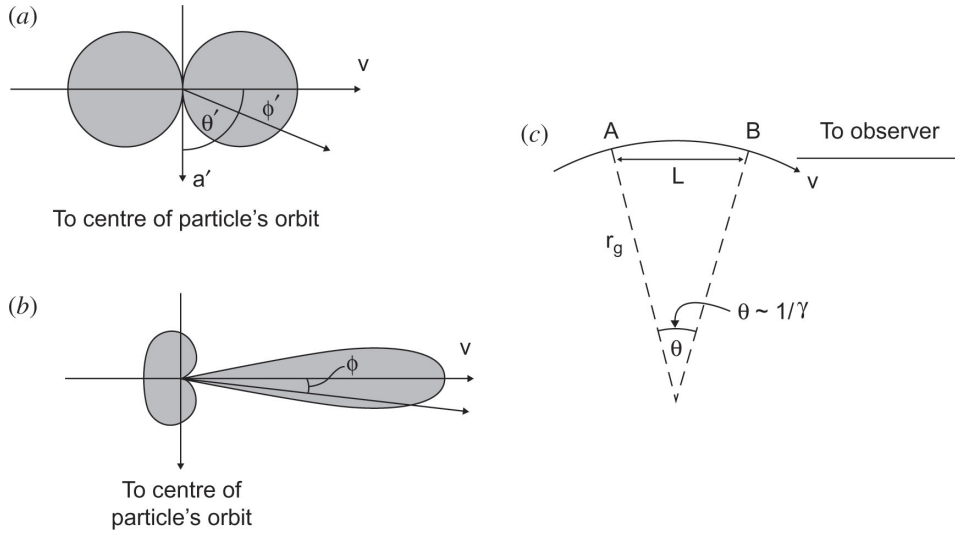
Figure 3.1.: Relativistic beaming of synchtrotron emission from Longair (2011). (a) shows the radiation from the particle in its instantaneous rest frame, (b) radiation pattern observed in the laboratory frame, (c) the path of the particle, when the beamed emission is directed to the observer

ular to the magnetic field orientation projected onto the plane of the sky to the total emissivity. This leads to the expression:

$$\Gamma = \frac{p+1}{p+\frac{7}{3}} = \frac{\alpha+1}{\alpha+\frac{5}{3}} \tag{3.1.16}$$

Polarization from synchrotron emission is an important tool for deducing properties of the underlying magnetic field configuration as well as the particle distribution.

Synchrotron Self-Absorption

The photons released by synchrotron emission can be absorbed by electrons from the same population that caused them. This process is called *Synchrotron Self-Absorption*. Naturally this leads to a fragmentation of the synchrotron into an emission and absorption dominated part respectively with a characteristic turnover frequency ν_T. In other terms, we can define the *optical depth* τ_ν as the absorption coefficient a_ν of a medium integrated along the light path:

$$\tau_\nu = \int_{s_{\min}}^{s_{\max}} a_\nu(s)\,\mathrm{d}s \tag{3.1.17}$$
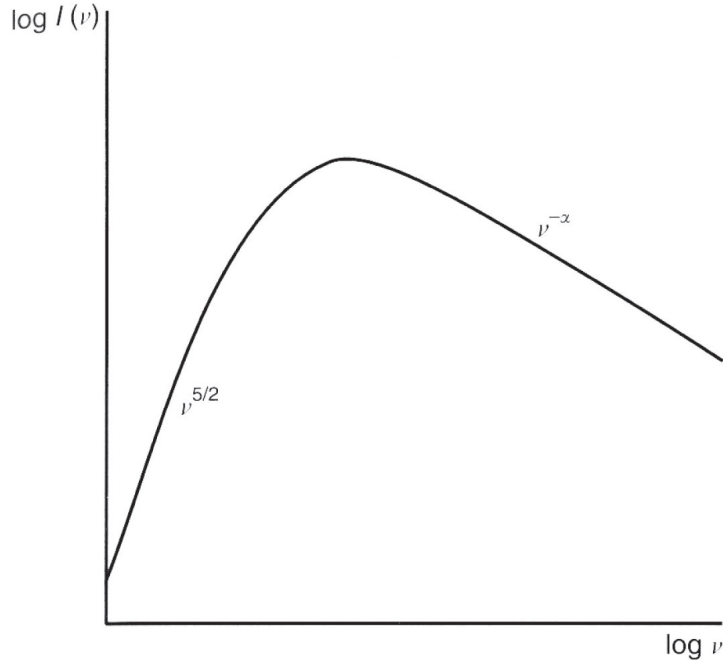
Figure 3.2.: Synchrotron Self-Absorption leads to $\nu^{5/2}$ slope in the spectrum of a source, indicating an optically thick medium. Above the turnover frequency the spectrum resembles a power-law distribution $\nu^{-\alpha}$, where α denotes the spectral index (from Longair 2011)

For $\tau_\nu > 1$ a medium is said to be *optical thick*, while $\tau_\nu < 1$ stands for *optical thin* media. The $\tau_\nu = 1$ region is characterised by ν_T in the energy spectrum, whereas the distribution below and above ν_T behaves like (Fig. 3.2):

$$F_\nu \propto \nu^{-\alpha} \quad \text{for } \nu > \nu_t \tag{3.1.18}$$

$$F_\nu \propto \nu^{\frac{5}{2}} \quad \text{for } \nu < \nu_t \tag{3.1.19}$$

If an astronomical object shows such a spectral distribution, one should be able to deduce immediately synchrotron emission from relativistic electrons as a likely cause. However reality is as usual much more complicated. The radio spectrum of some active galaxies is usually flat with only minor turnovers. Nevertheless such a behaviour is thought to be the result of synchrotron self-absorption. A possible explanation lies in the fact that our calculation assumed a single homogeneous medium. The observed spectrum can be the sum of spectra from different regions of the source with varying absorption properties. Recently Angelakis et al. (2012) reported on the spectral evolution of a sample of 78 AGN as part of the F-Gamma monitoring program between 2.64 and 142 GHz. They observed that the shape of the spectrum especially in regards of an excess in flux density differs within the sample. Based on this they suggested a classification scheme.

Inverse Compton and Synchrotron Self-Compton Emission

A photon with energy $E_{ph} = h\nu$ and an electron with rest mass $E_0 = m_e c^2$ is considered in the centre of momentum frame of reference.

If $E_{ph} \ll E_0$ it is safe to assume that in the classical limit the low energy photon can be scattered of the stationary electron without a change of energy. This elastic process is called *Thomson scattering*, for which the *Thomson cross-section* holds:

$$\sigma_T = \frac{e^4}{6\pi\epsilon_0^2 m_e^2 c^4} \approx 6.7 \times 10^{-29} \text{m}^2 \tag{3.1.20}$$

. In general, the process is inelastic and leads to a decrease in energy of the scattered photon with respect to the incident photon. Thus, some of the energy is transferred to the electron. This effect is known as *Compton scattering*. Quantum relativistic corrections yield the *Klein-Nishina cross section* σ_{KN} with $\sigma_{KN} \to \sigma_T$ if $E_{ph} \ll E_0$. In the other extreme σ_{K-N} shows, that Compton scattering becomes less efficient at high energies.

If the electron moves at highly relativistic velocities *inverse Compton scattering* will be of relevance. In this case, the electron looses some of its kinetic energy by transferring it to the scattered photon. Assuming $E_{ph} \ll E_0$ the intriguing beauty of the energy loss rate of inverse Compton

$$-\left(\frac{\mathrm{d}E}{\mathrm{d}t}\right)_{IC} = \frac{4}{3}\sigma_T c u_{\mathrm{rad}} \left(\frac{v}{c}\right)^2 \gamma^2 \tag{3.1.21}$$

rests in its similarity with the synchrotron rate in Eq. 3.1.12, where the factor $\frac{B^2}{2\mu_0}$ denotes the energy density of the magnetic field u_{mag} similar to the energy density of the radiation field u_{rad} in Eq. 3.1.21. Hence, it is possible to show that for a power-law distribution of electrons the spectral index of the radiation is again $a = \frac{p-1}{2}$, though the photon flux density follows a spectral index of $a_{ph} = \frac{p+1}{2}$. An impressive conclusion regards the relationship between the incident and the up-scattered photon, which goes as $\nu \sim \gamma^2 \nu_0$. Therefore, inverse Compton can change infrared/optical photons e.g. from the continuum emission into X-ray/γ-ray radiation assuming a sufficiently high Lorentz factor.

Finally, we consider the case, in which photons interact with the same relativistic electrons in the jet plasma, which originally produced them via synchrotron emission. This time, these electrons increase the energy of the photon field via inverse Compton. The process is called *Synchrotron Self-Compton* and may be an important factor in explaining the high-energy emission of AGN such as Blazars. Via the ratio

$$\eta = \frac{(\mathrm{d}E/\mathrm{d}t)_{\mathrm{IC}}}{(\mathrm{d}E/\mathrm{d}t)_{\mathrm{Sync}}} = u_{\mathrm{photon}} \frac{2\mu_0}{B^2} \tag{3.1.22}$$

it is possible to estimate the magnetic flux density assuming it is possible to determine the synchrotron and inverse Compton energy loss rate through observations. If η surpasses 1 the energy loss of the seed electrons increases dramatically in favour of the production of high-energy photons.

For a synchrotron self-absorbed radio source $\eta = 1$ leads to the *critical brightness temperature* $T_{\mathrm{b,crit}}$

$$T_{\mathrm{b,crit}} = 10^{12} \left(\frac{\nu}{\mathrm{GHz}}\right)^{-1/5} \qquad (3.1.23)$$

which may place an upper limit on the brightness temperature of radio sources. Hence, this result can be important, when one wants to model the measured jet emission (see Sect. 4.3).

Studies of the spectral energy distribution (SED) make use of all these mechanism model the emission of AGN (most of all radio-loud quasars) from radio frequencies to gamma-rays and beyond (e.g. Wilkes (2004))

3.2. Physics of Jets in AGN

Jets belong to the most remarkable features of AGN. Several theoretical models on jet formation and propagation have been developed over the years, but probably the greatest challenge remains our ability to verify them. These theories probe the boundaries of our physical knowledge in *general relativity* (GR), *magnetohydrodynamic* (MHD) and *electrodynamics*. Therefore, the following section will summarise the current research status rather qualitatively based on excellent reviews such as Marscher (2009), Krolik (1999) and Begelman et al. (1984). For a general review on the topic of jets in various astrophysical systems with their similarities and differences see Pudritz et al. (2012).

3.2.1. Theories on the Formation of Jets

Key questions, which models on the formation of jets in AGN have to account for, are the following:

1. Where does the material for the jet come from?

2. How are jets initially produced?

3. What processes are responsible for the collimation of the jet's plasma?

4. How are the particles in the jet accelerate up to relativistic velocities?

Unfortunately, none of the currently available theories can satisfactorily explain these questions neither separately nor combined, but considerable effort is made to change

this. Therefore, it is worth reviewing the current status quo keeping in mind that it is a rapidly evolving subject.

An obvious choice as an answer to question 1 is the matter accumulated in the accretion disc. The search for a mechanism connecting it with the jet automatically leads to question 2. While Begelman et al. (1984) and Longair (2011) considered gas pressure gradients in the accretion disc as a suitable ansatz among others, Marscher (2009) as well as Longair & Gunn (1975) thought it to be unlikely in the case of highly energetic jets such as in blazars. The former process requires that the mean kinetic energy of the particles exceeds their gravitational energy due to the high temperatures of the gas, which can occur in the X-ray emitting regions. Magnetic fields are regarded as an essential component for the formation of jets and perhaps the primary reason (Marscher 2009). The advantage rests within the magnetically driven energy flux governed by the Poynting-flux, which travels automatically at the speed of light (Krolik 1999). If the energy density of the poloidal magnetic field in an accretion disc is high enough, particles will travel along those field lines extending further away from the disc. The rotation of the disc strengthens the toroidal component of the magnetic field, which results in an inward force focusing the ejected material. The toroidal field strength surpasses the poloidal field further away from the starting point causing an inward force to collimate the newly formed jet. This process was originally suggested by Blandford & Payne (1982) and does not intrinsically require the existence of a black hole in the centre of the disc. A few years earlier Blandford & Znajek (1977) presented a model, in which the magnetic field is tied to a spinning black hole rather than an accretion disc. They demonstrated that if the field energy is high enough, electron-positron pair production and a subsequent cascade is possible, delivering the material for the jet plasma. In this case the jet feeds on the rotational energy of the SMBH. Both models currently represent the most prominent attempts to explain the earliest stage of jet formation (see Krolik 1999 and Pudritz et al. 2012 for further literature).

Up to this point questions 3 and 4 have been neglected. Following Marscher (2009) the previous theories lead to an overall helical magnetic field configuration with toroidal field component providing a force toward the jet axis. At the same time the field expands with increasing distance from the origin of the jet, thereby decreasing the energy density of the magnetic field. The resulting pressure gradients will be able to accelerate the jet plasma up to highly relativistic velocities, if the energy density of the field is significantly larger than the rest-mass energy density of the material. As long as this imbalance exists, the plasma flow will spiral along the field lines. It is possible that bends in the plasma flow, which are caused by instabilities in the current, which transfer magnetic field energy into internal energy of the plasma (Hardee 2006). At the point of equilibrium between energy density of the magnetic and particle field, magnetic acceleration will discontinue and magnetic field structure may be more or less irregular. This region can be labeled as the *acceleration and collimation zone* (ACZ) (Marscher 2009). Gas pressure dynamics can still be of importance regarding collimation in acceleration. This happen in the form of *external shocks*, due to interaction with interstellar medium and *internal shocks*,

because of inhomogeneous velocity distribution in the plasma or newly injected material.

The above description allows the production of a highly relativistic jet with Lorentz factor $\gamma \sim 10$, confined within $\sim 1°$ in the inner $\sim 1\,\mathrm{pc}$ (Jorstad et al. 2005). Additionally, they observed that the opening angle of the jet is inversely related to the Lorentz-factor, which is a prediction of magnetic and gas pressure driven systems. A visualisation of the jet paradigm is depicted in Fig. 3.3 with the above and bottom panel giving a structural and radiative overview respectively on a logarithmic distance scale in magnitudes of Schwarzschild radii.

As stated earlier jets remain stable from pc to kpc scales far beyond the ACZ expanding along the way as long as the gas pressure of the jet exceeds the ambient pressure. With increasing distance current-driven instabilities are replaced by *Kelvin-Helmholtz instabilities* (KHI) due to the interaction of the jet plasma with the interstellar or intergalactic medium. They arise, if two fluids with different velocity distribution are connected via a discontinuity. As long as the Mach number, Lorentz factor and/or the magnetic field are high enough, KHI do not have a strong effect (Marscher 2009; Hardee 2006, see also Begelman et al. 1984). This is probably one reason for jets in strong FR2 galaxies such as 3C111 to be well collimated up to kpc scales. Nevertheless, Kadler et al. (2008) interpreted the behaviour of jet components about 3 pc away from the core in terms of KHI. The FR1 source 3C31 shows a two-sided jet, which expands rather straight from the core until it becomes unstable on both sides at kpc scales Laing et al. (2008). The example of 3C31 shows very well that magnetic fields are still of importance at this scale. It is however currently very challenging to extract these information from polarimetric data at all scales.

3.2.2. Characteristics of Jets

Based Marscher (2009), Krolik (1999) and Longair (2011), it is convenient to pick out important features, which are observed in jets of AGN.

The Core is the most compact component of the jet visible at radio images. Blandford & Königl (1979) initially associated the core with a transition region along the jet from optical thick to optical thin (Sect. 3.1.2), where $\tau = 1$. Therefore, it should move further down the jet with increasing frequency. This so-called *core shift* is however not always observed (Marscher 2009). Kovalev et al. (2008) were able to obtain statistical results on core shifts. They searched in a sample of 277 AGN and detected a variable core position in 29 sources. The shift between 2.3GHz and 8.6GHz goes as high as 1.4 mas with a median of 0.44mas. 3C111 did not belong to the 29-source-group.

The core shift r_c can be expressed in terms of the observing frequency ν_{obs} (e.g. Lobanov 1998)

$$r_c \propto \nu^{-\frac{1}{k_r}} \tag{3.2.1}$$

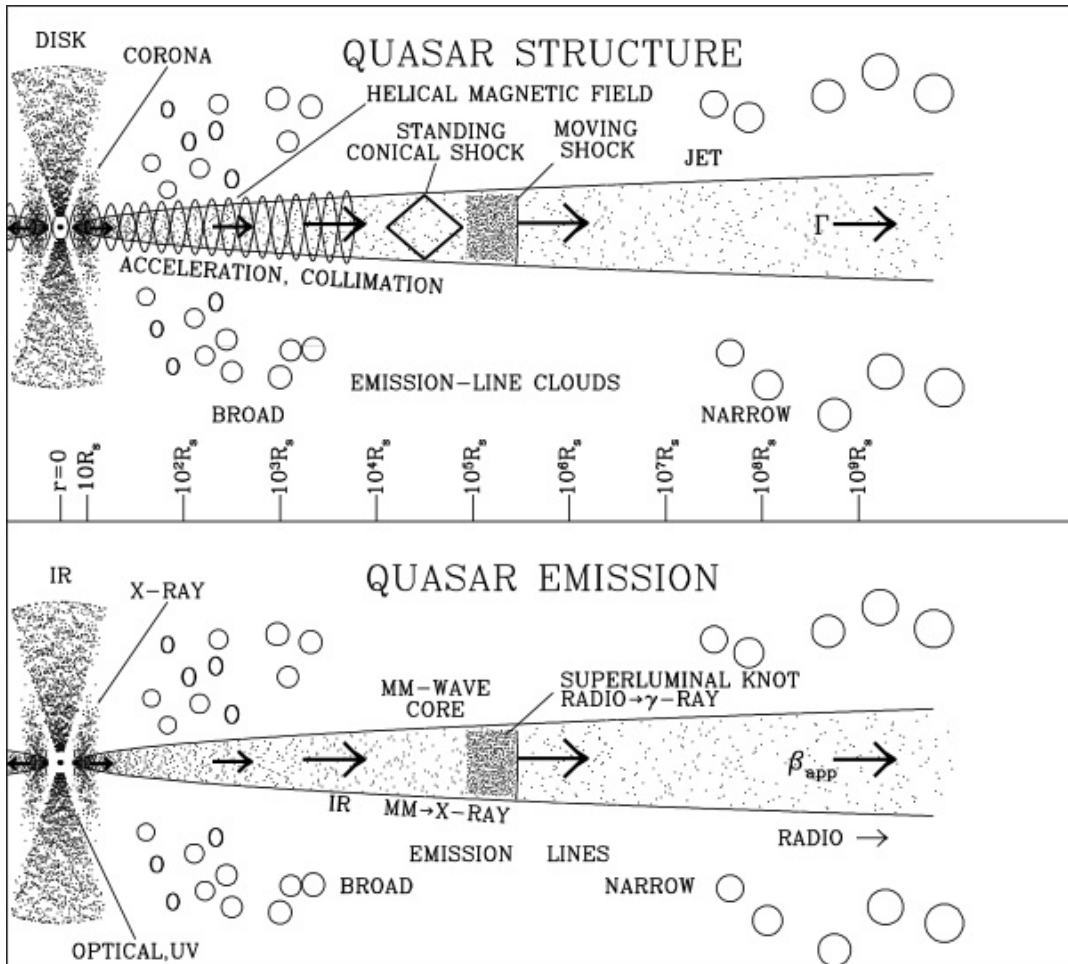where the index k_r depends on the magnetic field and particle density distribution.

Figure 3.3.: Illustration of jet formation and expansion from Marscher (2009). The distance from the SMBH is scaled logarithmically in magnitude of Schwarzschild radii. The top panel shows structural properties of the jet, while the bottom panel shows the emission properties of the jet
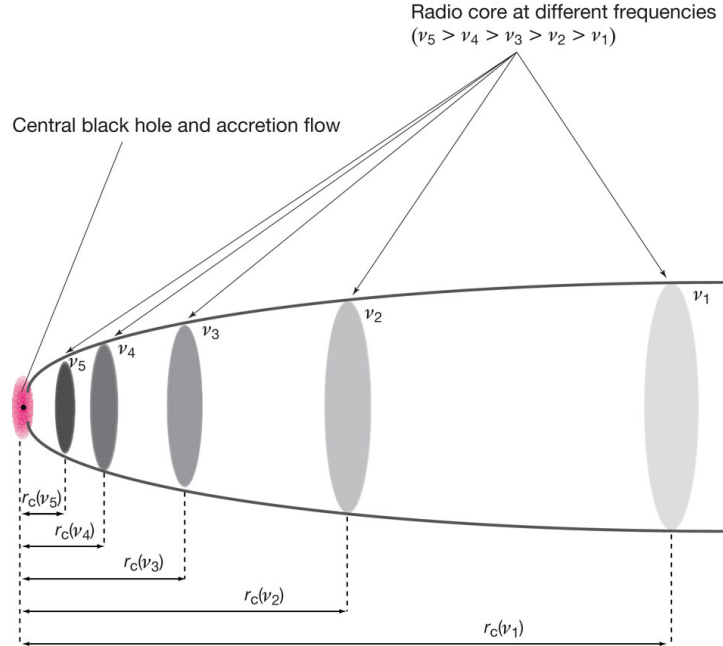
Figure 3.4.: Principle of core shift in a radio jet from Hada et al. (2011). With increasing
frequency the radio core moves closer to the jet base.

Hence, the k_r can be determined, by measuring the core shift at two different frequencies.

An example of a core shift is given by the close active galaxy M87. Recently Hada et al. (2011) used a six-frequency VLBA campaign to determine the change in position of the core with an accuracy of $20\,\mu$as. The distance of the shift decreases with higher frequency with a dependency of roughly ν^{-1} consistent with Blandford & Königl (1979).

Quasi-Stationary of Slowly Moving Features have been reported on several occasions (e.g. Lister et al. 2009; Jorstad et al. 2005), besides the relativistic motion of the jet plasma. Their occurrence can probably be interpreted in terms of shocks and instabilities, which would accelerate the particles. As will be explained in Sect. 4.3. the process of obtaining the propagation velocity of the jet components is rather difficult.

On large scales the most obvious stationary feature of radio jets are the *radio lobes* caused by the interaction with the intergalactic medium. In FR1 sources the jet continues until it reaches an instability, which destroys any confinement and the jet plasma is decelerated. The transition from jet to lobe occurs more or less smoothly. Again 3C31 is a good example for this type Laing & Bridle (2002). The strong jets of FR2 galaxies behave somewhat differently. The propagation of the jet stops abruptly, causing a strong shock that leads to the high luminosities of radio lobes observed. The point, where the luminosity has its maximum is usually associated with the termination of the jet and called *hot spot* (see Fig. 2.4).
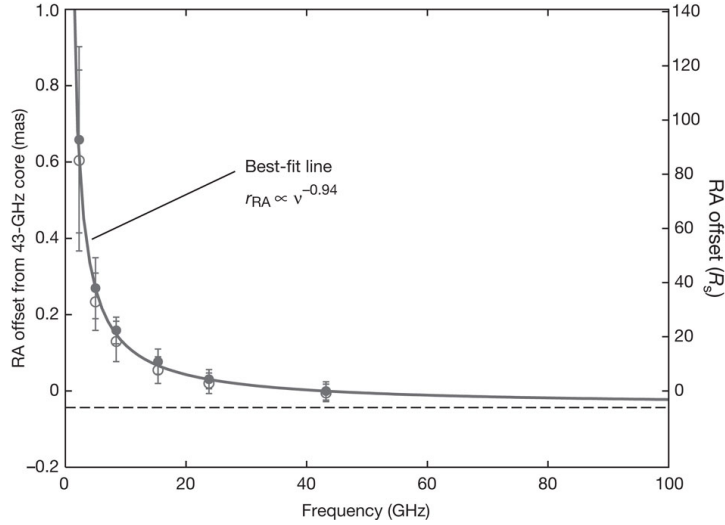
Figure 3.5.: Core shift of M87 from Hada et al. (2011), who used VLBI observations between 2.3 and 43 GHz. The solid line is fit to the data, with the slope moving asymptotically to the horizontal line. The core at 43 GHz is set as the point of reference

Superluminal Motion is at first sight perhaps a confusing feature of radio-loud AGN: Components of the jet can propagate at velocities apparently above the speed of light. It was predicted originally by Rees (1966) and confirmed five years later by Whitney et al. (1971). The effect can be explained by considering one blob stationary at time $t = 0$ in the laboratory frame of reference with distance d to the observer. A second blob is emitted and travels a distance of $\beta \Delta t \sin \theta$ projected on the sky within the time Δt, where θ is the angle to the line of sight. This leads to an apparent velocity of (Krolik 1999):

$$\beta_{app} = \frac{\beta \sin \theta}{1 - \beta \sin \theta} \tag{3.2.2}$$

As mentioned earlier, 3C111 is one of only two radio galaxies in the flux-limited Mojave 1 sample of AGN on the northern sky exhibiting superluminal motion. The majority of the 135 sources showing superluminal motion belong to BL Lacs and quasars. The maximum apparent speed was measured to $\sim 50c$ (Lister et al. 2009). Whereas the Mojave programs observes at 15 GHz, Jorstad et al. (2005) collected a smaller sample of 15 AGN for studying at 43 GHz. The distribution of β_{app} had its median peak in both reports at $\sim 10c$ (Lister et al. 2009). As stated in Marscher (2009) the components in the jet plasma exhibiting superluminal motion can be explained via the injection of turbulent, concentrated plasma into the jet stream. Electrons in these 'blobs' may be accelerated by second order Fermi acceleration. Other interpretations uses shock waves, in which the electrons are accelerated within the discontinuity of the shock front. As a result electrons will loose the ability to radiate at high frequency once they leave the
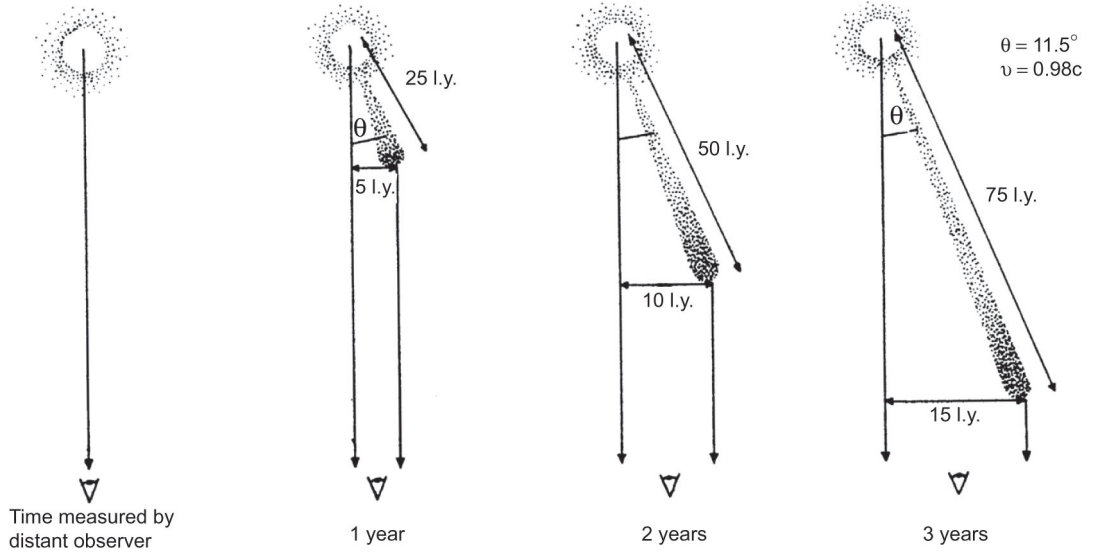
Figure 3.6.: Illustration of the projection effect involved with apparent superluminal motion from Longair (2011) of a source moving at $v = 0.98c$ close to the speed of light at an angle of $\theta = 11.5°$

shock. Frequency stratification leads to a division of the shock front, in which electrons with highest energy distribution can be found in a thin layer close to the shock, while the energy of the electrons decreases with increasing volume.

Relativistic Beaming and Doppler boosting A particular effect caused by emission from relativistic particles, is called *relativistic* . The *Doppler factor* is defined as the frequency change of radiation with angle θ to the line of sight due to the transformation from the rest frame (primed) to the observer's (unprimed) frame of reference, is given by:

$$D = \frac{\nu}{\nu'} = \frac{1}{1 + \beta \cos \theta} \tag{3.2.3}$$

This alters the observed spectrum significantly. In the case of optical thin synchrotron emission (Subsect. 3.1.2) the flux density F_ν behaves as $F_\nu \propto \nu^{-\alpha}$. In addition, Rybicki & Lightman (1979) showed that $F_\nu \nu^3$ is Lorentz invariant. According to Lind & Blandford (1985), this leads to a beamed spectrum of:

$$F_\nu \propto D^{3+\alpha} \nu^{-\alpha} \quad \text{for moving plasma} \tag{3.2.4}$$
$$F_\nu \propto D^{2+\alpha} \nu^{-\alpha} \quad \text{for stationary plasma} \tag{3.2.5}$$

Another implication derived from this solution is the following. If plasma is ejected from the core into symmetrically two-sided jet with one side closer to us than the other one,

the ratio between boosted ($F_{\nu,1}$) and de-boosted ($F_{\nu,1}$) emission is given by (Longair 2011)

$$R = \frac{F_{\nu,1}}{F_{\nu,2}} = \left(\frac{1 + \beta\cos\theta}{1 - \beta\cos\theta}\right)^{3+\alpha} \tag{3.2.6}$$

As an immediate consequence of Eq. 3.2.6, the possibility of detecting flux from the counter-(deboosted)-jet can be assessed, if the flux of the jet and the spectral index is known.

3.3. Concepts of Very Long Baseline Interferometry

The data analysed in this thesis are obtained with a technique called Very Long Baseline Interferometry (VLBI), which is a special branch of radio interferometry. It allows radio telescopes from all over the world, which share no direct connection, to observe the same object. Before the particularities of VLBI are discussed, a basic overview of interferometry is necessary. The classical textbooks by Thompson et al. (2001), Burke & Graham-Smith (2010) and Taylor et al. (1999) are recommend for an in-depth introduction into this subject and represent the basic literature for this section.

3.3.1. The Two-Element Interferometer

Modern Interferometers comprise a number of stations, many times the factor of two, but the basic principles can be reduced to the case of two telescopes. In general, Interferometry is the measurement of the *spatial coherence function* of an incident radiation field, for which the far-field approximation is assumed to be valid. That is why, only information on the two-dimensional extent of a source can be obtained at best.

Fig. 3.7 depicts the setting, in which the distance between the two telescopes is labelled $\mathbf{b} := \vec{b}$ and is called the *baseline* between station one and two. The direction of the incident radiation is given by the unit vector $\mathbf{s}$, which is defined relative to the so-called *phase-tracking centre* $\mathbf{s_0}$ (e.g. the absolute position of the source on the sky) with the displacement given by $\sigma = \mathbf{s} - \mathbf{s}_0$.

Radiation from the source does not reach both telescopes at the same time. Because of the far-field approximation the resulting *geometrical delay* τ_g can be expressed in terms of $\tau_g = \frac{\mathbf{b} \cdot \mathbf{s}}{c}$. The signal, received by the antennas, is amplified and filtered through a bandpass $\Delta\nu$ around the centre frequency ν_0. The *correlator* multiplies the signal $E_1(t) = \epsilon_1 \exp(-2\pi\imath t)$ and $E_2(t) = \epsilon_2 \exp(-2\pi\imath(t - \tau_g))$ from two stations and averages it in time. The output function R can be expressed in terms of the brightness $I(s)$ of the source in units of $\mathrm{W\,m^{-2}\,Hz^{-1}\,s^{-1}}$ coming from within a solid angle $d\Omega$ and received by an array of telescopes with an effective reception pattern $A_{eff}(\mathbf{s})$:

$$R = \Delta\nu \exp(2\pi\imath\mathbf{b} \cdot \mathbf{s}_0) \int_S A_{\mathrm{eff}}(\sigma)I(\sigma)\exp(-2\pi\mathbf{b} \cdot \sigma)\,d\Omega \tag{3.3.1}$$

Eq. 3.3.1 includes the expression for the geometrical delay and neglects any kind of constant gain factor. Furthermore, it assumes, that emission originating in different parts of the source is uncorrelated. The rotation of the Earth causes τ_g to vary in time, leading to a fringe pattern of the correlator signal R. In principle, it is possible to correct τ_g by inserting a delay τ_i into the signal path of the affected station.

As Eq. 3.3.1 reveals, Fourier transformation is essential in analysing an interferometer. This equation represents a convolution of the interferometer's reception pattern modulated by the fringe function with the brightness distribution of the source. The convolution theorem states that an equal result is obtained by Fourier transforming both parts separately and multiply them afterwards.

The spatial coherence of the incident field is given by the integral in Eq. 3.3.1 and denotes the *complex visibility V*:

$$V = |V|\exp(\imath\phi_V) = \int_S A_{\mathrm{eff}}(\sigma)I(\sigma)\exp(-2\pi\mathbf{b}\cdot\sigma)\,\mathrm{d}\Omega \tag{3.3.2}$$

At this point, a more convenient system of coordinates may be chosen. The baseline vector between two telescopes provides a set of coordinates (u, v, w) given in units of the observing wavelength. It is a convenient choice to define a coordinate system in terms of baseline vectors, i.e. the relative distance between two telescopes. The coordinates of this right-handed system (u, v, w) are given in units of the observing wavelength, where the (u, v) plane is normal to $\mathbf{s}_0$, i.e $\frac{\mathbf{b}\cdot\mathbf{s}_0}{\lambda} = w$ and $\frac{\mathbf{b}\cdot\sigma}{\lambda} = ul + vm + w\sqrt{1 - l^2 - m^2}$. Here, l and m represent the direction cosines of u and v forming a plane, which lies tangential on the celestial sphere at the phase-tracking centre. If it is reasonable to assume, that all baselines are confined to the (u, v) plane[1], the complex visibility simplifies to:

$$V(u, v) = \int\int I(l, m)\exp(-2\pi\imath(ul + vm))\,\mathrm{d}l\,\mathrm{d}m \tag{3.3.3}$$

where the reception pattern and coefficients of the Jacobi determinant are incorporated into $I(l, m)$. The inverse Fourier transformation[2] can be applied to determine the intensity distribution of the source from the measured visibility function:

$$I(l, m) = \int\int V(u, v)\exp(2\pi\imath(ul + vm))\,\mathrm{d}u\,\mathrm{d}v \tag{3.3.4}$$

Unfortunately, Eq. 3.3.4 becomes even further complicated, because $V(u, v)$ is turned into a discrete function by the sampling function $S(u, v)$ of the array, i.e. $S(u, v) = 0$ where no baseline exists in the (u, v)-plane. It leads to the so-called *dirty image* $I_D(l, m)$,

---

[1] This assumption is in general not valid, but such a discussion goes too far here, but can be found e.g. in Thompson et al. (2001).

[2] The choice of the minus sign is usually arbitrary, but follows the convention in the given literature at the beginning of this section.

which is the convolution of the intensity distribution of the source and the *synthesized beam* $B(l, m)$:

$$I_D(l, m) = \int \int V(u, v) S(u, v) \exp(2\pi\imath(ul + vm)) \, \mathrm{d}u \, \mathrm{d}v = I(u, v) * B(l, m) \quad (3.3.5)$$

where the asterisk denotes the convolution. Solving Eq. 3.3.4 for $I(l, m)$ is an inversion problem, for which different solutions have been developed. One of them is called CLEAN and is discussed in Subsect. 4.3.2.

The rotation of the earth improves the density of the sampling, because of the movement of the array with respect to the source. The more stations are contained in an array, the better the sampling of the visibility. This technique is called *Earth rotation synthesis*. The observing time of an array is thus limited to the point, when the source disappears behind the horizon for the telescopes. For VLBI observation it allows a source to be measured for up to 12 hr. In addition, the half power width of the synthesised beam determines the resolution of the array in the form of the longest baseline $b_{\max}$

$$\theta_{HPBW} \approx \frac{\lambda}{b_{\max}} \quad (3.3.6)$$

Eq. 3.3.5 is usually further modified in terms of a weighting function of the visibilities, which accounts for inhomogeneous sampling in the (u, v)-plane. Especially VLBI arrays are less well sampled on longer baselines than on shorter ones.

3.3.2. Particularities of VLBI

The most basic difference between VLBI arrays and other interferometers is the scale of the spatial distribution of individual stations, which is only limited by the circumference of the Earth (at least for ground-based arrays). These telescopes from independent institutions can be combined to observe the same source without any necessity of direct connectivity. The separately sampled data are afterwards shipped to the correlator. VLBI arrays provide the highest spatial resolution of any astronomical instrument, though it faces a few more challenges than for connected arrays, which are examplarily discussed in the following text:

VLBI relies on accurate measurements of the phases of the visibility. Therefore, a model of the location of each station around the Earth is vital in order to obtain precise measurements of the baselines and, hence, the geometric delay. The two-dimensional (u, v)-plane in the prior subsection becomes a projection of the three-dimensional distribution of the antennas onto the two-dimensional (u, v)-plane. On the other side, a precise positioning model makes it possible to determine movements of the tectonic plates.

Throughout the observation of a VLBI array, each station may face different weather

conditions. Especially VLBI at mm wavelengths is sensitive to changing weather, because of the already short atmospheric coherence length of $\sim 10\,\mathrm{s}$ (Martí-Vidal et al. 2012). Therefore, opacity effects have to be considered in calibrating the phases.

In an inhomogeneous array, each station can comprise different electronic systems and utilises different ways of measuring the time of the measurements.

Since the correlator cannot account for all of these influences, delay errors occur. This topic is very well reviewed by Cotton (1995) and Thompson et al. (2001). Delay and phase are related via $\phi(t, \nu) = 2\pi\nu\tau(t)$. After differentiation and first order expansion, the change in phase can be expressed by:

$$\Delta\phi(t, \nu) = \phi_0 + \frac{\partial\phi}{\partial\nu}\Delta\nu + \frac{\partial\phi}{\partial t}\Delta t \tag{3.3.7}$$

where ϕ_0 is a phase error for the point of reference in time and frequency, $\frac{\partial\phi}{\partial\nu}$ and $\frac{\partial\phi}{\partial t}$ denotes the change of the phase of the visibility in frequency and time. Both quantities are known as the fringe rate and the fringe delay, respectively. The process of estimating the fringe delay and rate is called *fringe fitting*. Schwab & Cotton (1983) developed the *global fringe fitting* algorithm to account for these effects. A detailed discussion of this vast subject is beyond the scope of this thesis.

Closure relationships are not unique to VLBI, but have a profound impact on the calibration of the obtained data. They describe relationships of the phases and amplitudes of the visibilities between a certain number of stations of the array in a closed loop (see also Pearson & Readhead 1984).

An array of N stations comprises $N(N-1)/2$ baselines, which lead to the same number of visibility phases $\psi_{ij} = \Phi_{ij} + \phi_i - \phi_j + \epsilon_{nm}$, where Φ_{ij} denotes the desired phase value of the visibility on this particular baseline, ϕ_i and ϕ_j represent station-dependent errors and ϵ_{nm} is a noise term. Within a triangle of stations, the *closure phase* Ψ_{ijk} does not contain any station-dependent errors of the visibility phase:

$$\Psi_{ijk} = \psi_{ij} + \psi_{ik} + \psi_{jk} = \Phi_{ij} + \Phi_{ik} + \Phi_{jk} + \epsilon_{ij} + \epsilon_{ik} + \epsilon_{jk} \tag{3.3.8}$$

Calibration of the phases is now possible by setting an arbitrary chosen visibility phase e.g. to zero. Usually, there is no redundancy in VLBI arrays, i.e. the same baseline is covered by a different set of telescopes. Therefore, the use of closure phases results in a loss of information on the absolute position of the source. That is why, the comparison of data from different frequencies becomes much more complicated. The aforementioned core shift (Subsect. 3.2.2) is a possible way to compensate this effect at least between two or more frequencies.

Within a loop of four stations, the closure amplitude A_{ijkl} can be calculated to con-
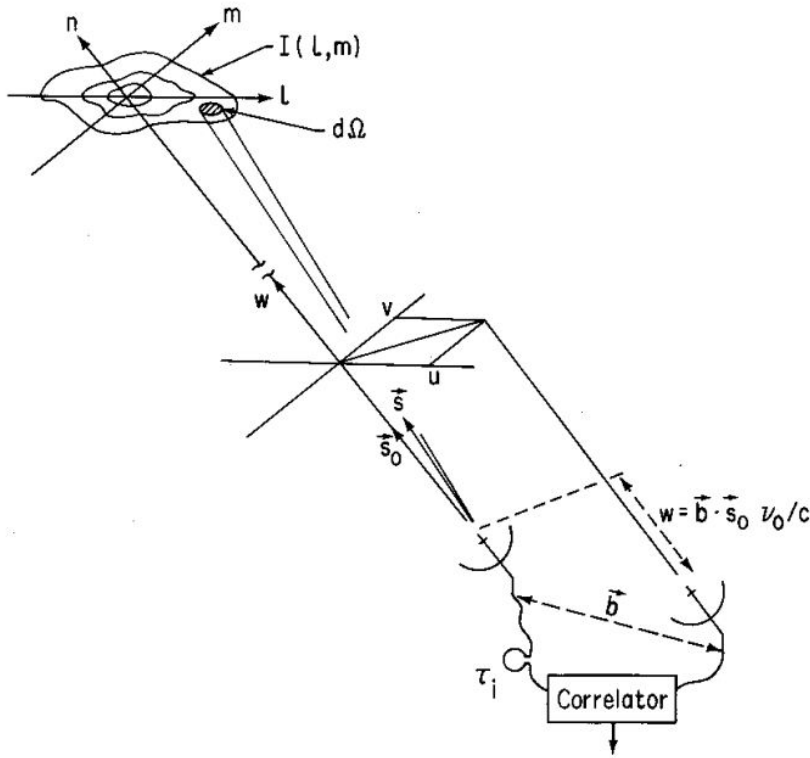
Figure 3.7.: A diagram of the 2-element interferometer taken from Taylor et al. (1999), showing the geometric delay between the two telescopes, the setting of the (u, v) and (l, m)-plane.

strain the antenna gain factors, which have to be applied:

$$A_{\mathrm{ijkl}} = \frac{|V_{\mathrm{ij}}| \cdot |V_{\mathrm{kl}}|}{|V_{\mathrm{ik}}| \cdot |V_{\mathrm{jl}}|} = \frac{|\Gamma_{\mathrm{ij}}| \cdot |\Gamma_{\mathrm{kl}}|}{|\Gamma_{\mathrm{ik}}| \cdot |\Gamma_{\mathrm{jl}}|} \tag{3.3.9}$$

where Γ denotes the gain factors for each antenna. Three closure amplitudes can be calculated for a set of four stations, but only two are independent.

Closure phases and amplitudes are an integral part of self-calibration, discussed in Subsect. 4.3.2.

4. Observation and Data Processing

Three observations at 86 GHz performed by the Global mm-VLBI Array (GMVA), are the foundation of this thesis. Therefore, the chapter includes first of all a short review of the GMVA. Afterwards a summary of the observation of 3C111, used for this thesis, is given. Finally, the last section features a review of the various procedures involved in processing the data.

4.1. The Global mm-VLBI Array

The *Global mm-VLBI Array* (GMVA[1]) is an array of various European and North American telescopes. It is capable of observing at 43 GHz and 86 GHz and currently consists of the stations listed in Tab. 4.1. Their distribution is indicated in Fig. 4.1. The eight US telescopes represent a subset of the total 10 VLBA stations. The missing two (Hancock and St. Croix) are not equipped with receivers for measurements at 86 GHz.

The configuration of the GMVA leads to a maximum baseline of $\sim 10900\,\mathrm{km} \approx 3100\,\mathrm{M}\lambda$ between Plateau de Bure and Manua Kea. Thus, it is currently the largest coordinated array to observe at 86 GHz with an angular resolution down to $\sim (40-70)\,\mu\mathrm{as}$ (Martí-Vidal et al. 2012). For prominent VLBI sources such as SgrA* (distance d = 8 kpc, Doeleman 2008), M87 (redshift $z = 0.0044$) and 3C111 ($z = 0.049$) this translates into a linear scale of $\sim (0.4-0.7)\,\mathrm{AU}$, $\sim (0.01-0.02)\,\mathrm{ly}$ and $\sim (40-70)\,\mathrm{mpc}$, respectively.

While the VLBA is a homogeneous array, i.e. it consists of telescopes of the same type, the antennas used by the GMVA differ in construction. Because of the distribution of the telescopes, it is usually not possible that all telescopes can observe the same source together the whole time. Therefore, the splitting into two sub-arrays (Eu, US) is inevitable, which becomes very important in the process of data reduction (Sect. 4.3, Martí-Vidal et al. 2012).

The participating stations belong to independent institutions. Hence, the GMVA is only capable of observing twice a year. Nevertheless, it has been active since the 1990s (e.g. Lobanov et al. 2000), back then in the form of the *Coordinated mm VLBA Array* (CMVA). However, polarimetric 86 GHz VLBI observations are by far not standard (Martí-Vidal et al. 2012) and thus they are continuously developed further.

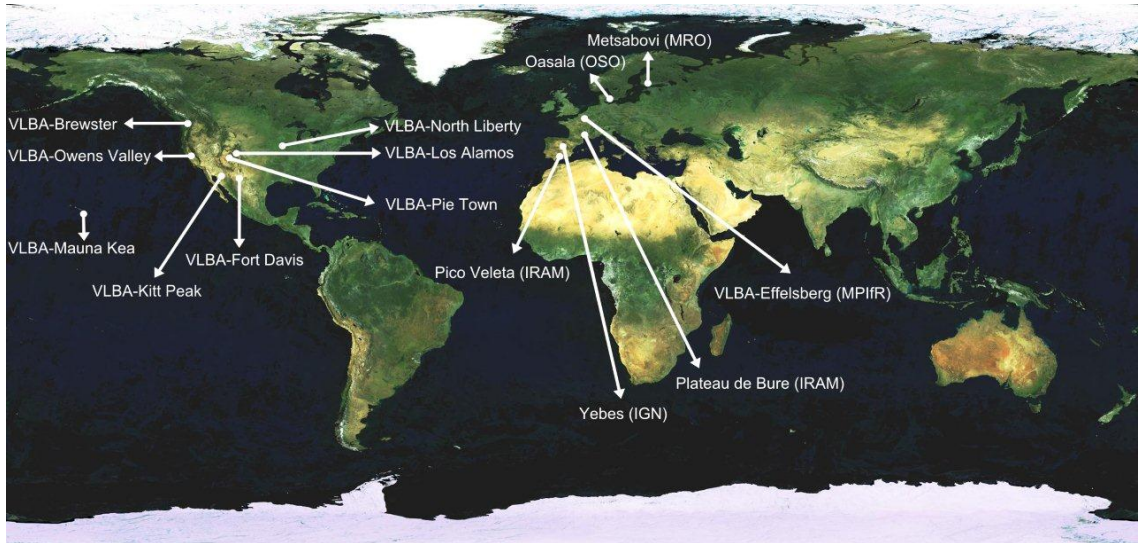[1]http://www.mpifr-bonn.mpg.de/div/vlbi/globalmm/

Figure 4.1.: Overview of the stations participating in the GMVA with their location in Europe and North America. Credit for the map of the Earth: ESA

Station	Location	Institute	Diameter
Europe			
Effelsberg	Germany	MPIfR	100 m
Pico Veleta	Spain	IRAM	30 m
Plateau de Bure	France	IRAM	6×15 m (phased)
Metsähovi	Finland	MRO	14 m
Onsala	Sweden	OSO	20 m
Yebes	Spain	CAY	40 m
USA (8×VLBA)			
Fort Davis	Texas		
North Liberty	Iowa		
Pie Town	New Mexico		
Los Alamos	New Mexico	NRAO	each 25 m
Brewster	Washington		
Owens Valey	California		
Kitt Peak	Arizona		
Manua Kea	Hawaii		

Table 4.1.: A list of the individual GMVA stations, including their location, institute and diameter of the dish. Plateau de Bure participates as a phased array of six antennas, with an effective diameter of 34 m (Martí-Vidal et al. 2012)

Session	Date	Calibrators
1st Epoch	2007-10-13; 2007-10-15/16	NRAO150, 0420-014
2nd Epoch	2008-05-11/12	NRAO150
3rd Epoch	2008-10-14/15	NRAO150, OJ287*

Table 4.2.: Overview of the GMVA sessions. Epoch one includes two single scans on 2007-10-13, but the majority of on-source time was on 2007-10-15/16. OJ287 requires further explanation, which can be found in Subsect. 4.3.1

4.2. GMVA Observation of 3C111

In early 2007, 3C111 exhibited a major flux density outburst above 10 Jy, which is about a factor of two higher than any flare since 1997 (Trippe et al. 2011, Alef et al. 1998). As a result Kadler et al. (2007) submitted a successful *Target of Opportunity* (ToO) proposal for the GMVA session in Oct. 2007. In addition, a follow-up proposal was approved with the goal to observe the evolution of the flare over the next GMVA sessions. Thus, the GMVA conducted measurements of 3C111 in Oct. 2007, May 2008 and Oct. 2008. At this time, Yebes was not yet part of the array. All measurements were obtained in dual polarization mode, though, Onsala has only single polarization receivers available.

A summary of the 3C111 sessions of the GMVA relevant for this thesis can be found in Tab. 4.2. Fig. 4.2 shows a curve of 3C111 at 86 GHz between 2007 and mid 2011. The plot was created by C. Grossberger with data collected by the F-GAMMA program[2]. The embedded lines indicate the time of the GMVA observation. A discussion of the outburst in terms of the light curve can be found in Appendix B.

0420-014 and NRAO150 were used as calibrators for epoch one, NRAO150 in epoch two, NRAO150 and OJ287 in epoch three. A perfect calibrator fulfils two primary conditions: The flux density remains high and constant on long time scales and the source is almost point-like, i.e. unresolvable by the array. The former sets the flux density scale for the observed source. The latter is necessary, because the calibrator works as a reference point for the phase information. However, at mm-wavelengths both conditions become increasingly difficult to meet for known sources. For example NRAO150 is known to show a small jet feature, which seems to swing around the core (Agudo et al. 2007).

Since three observations are not sufficient to yield a robust kinematic analysis, 43 GHz VLBA data from the monitoring program by A. Marscher of the Blazar Group (henceforth BG)[3] at Boston University is used. Although the 43-GHz-BG data were obtained at a lower frequency, they can be used to constrain the kinematic evolution of the 86 GHz jet (see Chapt. 5) via cross-identification of characteristic jet features at both frequencies.

---

[2]http://www3.mpifr-bonn.mpg.de/div/vlbi/fgamma/fgamma.html
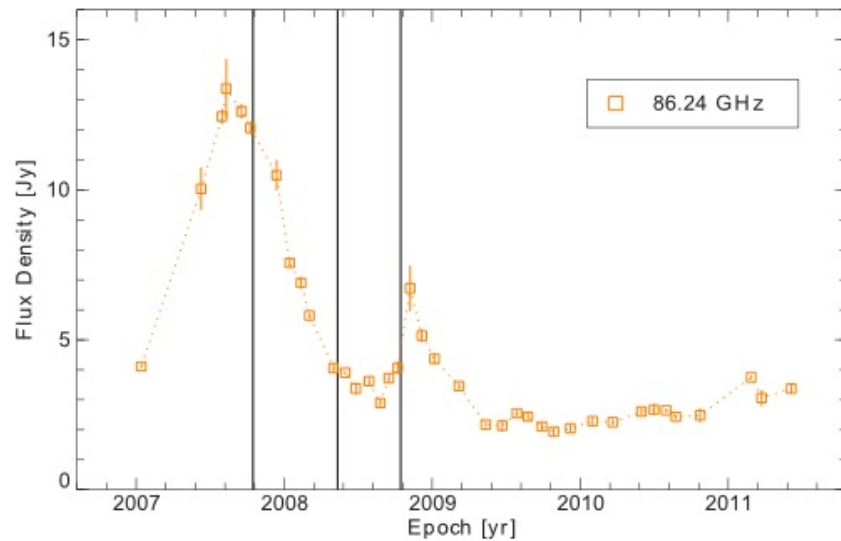[3]http://www.bu.edu/blazars/VLBAproject.html

Figure 4.2.: Light curve of 3C111 at 86 GHz . The lines indicate the observations of the GMVA. The dashed lines between the data points are not a fit. Image by C. Grossberger with data from the F-GAMMA monitoring program

4.3. Data Reduction and Processing

The processing of the gathered VLBI data can be divided into four major parts. Following the correlation at MPIfR, the data are loaded into the *Astronomical Image Processing System* (AIPS[4]) provided by NRAO. This powerful tool includes methods for amplitude calibration, atmospheric correction and fringe fitting (Subsect. 4.3.1). Amplitude and phase self-calibration (Subsect. 4.3.2) as well as the modelling of the imaged jet with Gaussian components (Subsect. 4.3.3) are performed in DIFMAP[5] (Shepherd et al. 1994). Although it is possible to do the last two steps with AIPS, DIFMAP includes a more user friendly environment and is less demanding on computational resources, since it is especially designed to perform these tasks.

A general introduction into the vast topic of calibration of VLBI data is given by classic text books such as Thompson et al. (2001) and Taylor et al. (1999).

4.3.1. A-priori Calibration and Fringe Fitting

The AIPS software uses so-called *verbs* as internal functions to execute specific scripts, which are programs of their own within the AIPS environment and are called *tasks*. Each task contains certain parameters (*adverbs*) as input variables. The list of parameters can be extensive for certain tasks, which allows a single task to be used for a variety of

---

[4]http://www.aips.nrao.edu/index.shtml
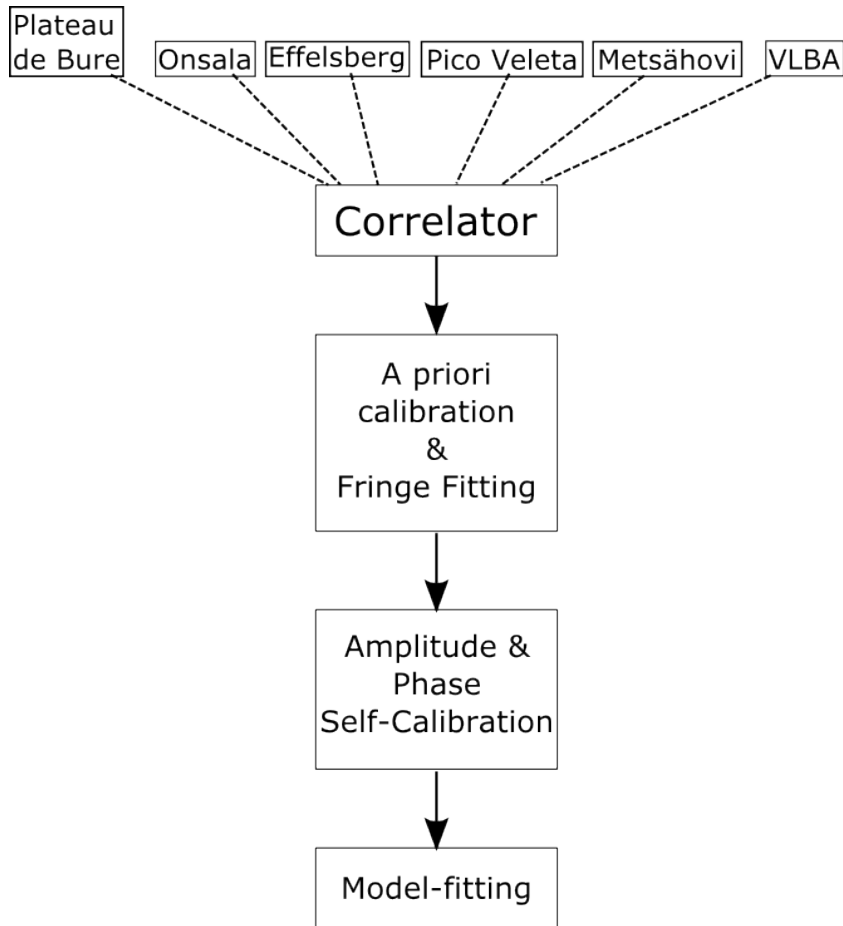[5]ftp://ftp.astro.caltech.edu/pub/difmap/difmap.html

Figure 4.3.: The diagram visualises the different parts of data reduction and processing. The data from each GMVA station is correlated followed by a-priori calibration (Subsect. 4.3.1) and self-calibration (Subsect. 4.3.2). Model-fitting uses the self-calibrated data for further analysis (Subsect. 4.3.3).

goals. Thanks to the complexity of AIPS, it can be utilised for processing various kinds of astronomical data (see the extensive cookbook NRAO 2011). With the development of ALMA and the EVLA, a new software package has been developed - the *Common Astronomy Software Application* (CASA[6]). However, so far CASA does not incorporated the necessary tasks to perform fringe fitting, which is essential for VLBI data reduction.

AIPS usually stores and loads data in the *Flexible Image Transport System* (FITS) format. Internally, the data are stored as specifically formatted tables. Each task in AIPS produces *extension files*, which contain the necessary information to modify the data. These files are applied to the data, either to produce new files or to export the calibrated data. However, they do not change the original data at any time. This is an important advantage, because it allows the user to return to previous steps in the reduction, if necessary, without starting from the beginning (in contrast to DIFMAP). The disadvantage of this management system is the increase in disk space with each new file, depending on the amount of information stored[7].

The amplitude and phase calibration in AIPS was performed for all three GMVA observations by T. Krichbaum at MPIfR. Martí-Vidal et al. (2012) report on the basic principles of calibrating GMVA data and present a script that will be able to perform several calibration steps automatically. This script was not available at the time of the 3C111 data analysis.

For each epoch, this part of the data reduction process goes as follows, with a more detailed description of selected steps afterwards:

1. The data are loaded into AIPS using the task FITLD.

2. The default setting for the mount type of Pico Veleta is wrong and has to be changed to Nasmyth by hand. The task CLCOR is used to correct for changes in parallactic angle of each telescope.

3. The *manual phase calibration* is performed with the FRING and CLCAL tasks, to correct for instrumental single-band delays and rates, i.e the change of phase with respect to frequency and time.

4. The *multi-band phase fringe fitting* corrects delays and rates between subbands due to inaccurate modelling of the array or atmosphere (FRING, CLCAL).

5. Information on antenna gain and system temperature are loaded into AIPS via ANTAB. APCAL carries out the amplitude calibration and correction for opacity of the atmosphere based on weather information for each station.

6. In dual polarization data, the single handed bands (i.e. RR, LL) are calibrated. However, the cross-hand visibilities have to be corrected for any residual delays.

---

[6]available from http://casa.nrao.edu/

[7]For example, the file size of the correlated data of the first epoch, before loading into AIPS, is approximately 5 GB. The final file including all tables and the original data is roughly 11 GB larger.

This is done, using the procedure VLBACPOL, which includes a number of AIPS tasks. This step is not discussed further, because the polarization of 3C111 was not analysed in this thesis.

7. SPLIT allows the data to be divided into separate single-source files, which are written out as uv-FITS files with FITTP. All extension files and the original data are saved with FITAB.

Manual Phase Calibration   (step 3) and multi-band phase fringe fitting (step 4), are specific requirements of VLBI data reduction (Sect. 3.3) and they are probably the most time consuming steps. Excellent reviews are available on this matter by Walker (1989), Cotton (1995), Taylor et al. (1999, chap. 22) and especially regarding the GMVA by Martí-Vidal et al. (2012). The fringe fitting algorithm was initially written by Schwab & Cotton (1983). Nevertheless, scripted phase calibration of VLBI data at mm-wavelengths is still under development.

Instrumental errors cause the phases to change with frequency and time. Under the assumption that these changes remain constant, FRING is set to look for solutions within each IF of one particular scan and stores them in a SN table. CLCAL takes these single-band solutions and applies them on the complete data set with the correction factors stored in a CL table. After FRING has found solutions for the rates, the rates are set to zero. This single-band delay calibration or manual phase calibration requires a reference antenna. At this point, the configuration of the GMVA can become a challenge. Due to the different rising time of sources in Europe and the US and the scheduling, the observations of all telescope may not necessarily overlap the whole time. This leads to *sub-arraying* of the GMVA. In addition, solutions are found on a strong signal, usually from the calibrator. Therefore, the chosen reference antenna should ideally be located in the centre of the array and possessing high *signal-to-noise ratios* (SNR) on all baselines. Unfortunately, this is generally not the case.

The solution is to perform the manual phase calibration sequentially on the sub-arrays. For example, a reference antenna for the European instruments is defined and calibrates first this part of the array. Then, one looks for promising transatlantic baselines to fringe-fit them. Already at this moment, the previously chosen reference antenna can be changed to another European one, if needed. As soon as at least one VLBA telescope is calibrated with a European one, the VLBA delays and rates can be corrected independently. Sometimes a further subdivision has to be done, which was in fact necessary for all three epochs. Each fringe fit is accompanied by CLCAL, though solutions found by FRINGE were only applied to those telescopes, which were part of the fringe-fit.

In order to find a reasonable starting point with high SNR, an initial fringe fit was performed for the whole array. Another important aspect of FRING is the definition of the integration time, which depends on the coherence length of the signal through the atmosphere. At 86 GHz, this value becomes very small ($\sim 10\,\text{s}$). However, experience has shown, that an integration time of 2-4 min still produces very good results, though

this depends strongly on the weather conditions (Martí-Vidal et al. 2012). Prior to each FRING call, the phase distribution per IF within a chosen integration time is displayed using the task POSSM, either to check, whether the last fit worked or to find the next combination of reference antenna and baselines. With SNPLT the solutions as well as their SNR can be displayed after each fringe fit. Considering the number of scans per observations available with an average scan length of $\sim 7\,\text{min}$, this step can take a lot of time.

The most difficulty for the GMVA data at this stage came from Onsala, Metsähovi and Manua Kea.

Multi-band phase fringe fitting (step 4) accounts for errors in the atmospheric and geographical station model of the correlator, which leads to delays between IFs. Some residual single-band delays may be still left over. The multi-band calibration uses a global fringe fit, i.e. no particular scan, source and sub-array is specified and one solution is found for all IFs. A good reference antenna may have been found due to the results of step three. In addition, FRING allows the user to define antennas, which will be used as an alternative reference, if the primary fails. However, the exhaustive baseline search in AIPS produced better results only for epoch three.

FRING always finds a number of "bad" solutions. To improve the amount of "good" solutions, the delay and rate intervals have to be adjusted carefully and several trial runs are usually necessary.

Amplitude calibration and opacity correction (step 5) become increasingly important at higher frequencies and for large arrays with stations facing different weather conditions. As stated above, the attenuation of the atmosphere is significant for 86 GHz.

First, information on the antenna gain curve and system temperature is loaded into AIPS via ANTAB, which generates a GC and TY file. The calibration itself is carried out by the APCAL task, which requires an additional file on the weather conditions for each stations to correct for the absorption of the atmosphere. Because no information on the gain curve were available for Metsähovi, a constant opacity value was applied to the system temperature. The provided gain curve of Onsala was already opacity corrected. Thus, these stations were excluded in APCAL in terms of opacity.

Seperation into single-source files (step 7) is necessary, because DIFMAP cannot process files, which contain data from multiple sources. Up to this point, each scan consists of four IFs. For the purpose of reducing disc space and processing time, the data are averaged across the IFs. In addition, it accounts for variations among the IFs.

The GMVA epochs differ most notably in time sampling and (u, v)-coverage.

The first epoch does not contain any data by Pico Veleta after the correlation, though bad weather occured only at the time of observation of 3C111. The time sampling and

Type	Description
SN	Stores solutions found by calibration tasks such as FRING, APCAL
CL	Calibration file, which includes correction factors for the data (CLCAL)
AN	Includes general information on the antennas
TY	Stores system temperature for each station (created by ANTAB)
GC	station dependent gain curves (created by ANTAB)
WX	local weather information for each station, necessary for opacity correction (APCAL)

Table 4.3.: Overview of particular AIPS extension files used for calibration

resulting (u, v)-coverage at the end of this part are depicted in the left panel of Fig. 4.4 and Fig. 4.5, respectively. The former shows two scans on 13th October, which were flagged already at the start of imaging, because of their two-day separation. All in all, the first epoch presents the best sampled observation of all three epochs. However, especially Onsala, Metsähovi in Europe and the VLBA station Manua Kea contain a lot of noise in their phase-data, which made them difficult to fringe-fit.

Epoch two includes only a small number of scans for Pico Veleta, while Onsala and Plateau de Bure had to be flagged all-together. Data from all other stations are available. The sampling of this epoch is intermediate in reference to the other epochs.

The third epoch suffered the most data loss already during observation. First, Plateau de Bure did not take part in that GMVA session due to technical problems. Second, Metsähovi lost all of its data, because of technical problems. Although Pico Veleta observed the source, there were no data available on 3C111 after correlation. In addition, the right-hand polarization data of Onsala were flagged, which is why total intensity imaging was not possible with Onsala. Effectively, epoch three contains data from Effelsberg and the VLBA subset (right panel in Fig. 4.4). The resulting decrease in (u, v)-coverage is shown in the right panel of Fig. 4.5. Since Effelsberg is still available, data on long baseline remain, but especially intermediate baseline are less dense compared to the first epoch. One particularity of GMVA-3 is its calibrators. For unknown reasons the correlated data file did not contain the calibrator NRAO150. Missing scans could be recovered, which were a part of a file of another observation, which included OJ287. However, OJ287 was observed a full day prior to 3C111 and NRAO150. Nevertheless, one scan with OJ287 was used during single-band fringe fitting between Effelsberg and Pico Veleta. In fact, data from Pico Veleta was only available for OJ287.
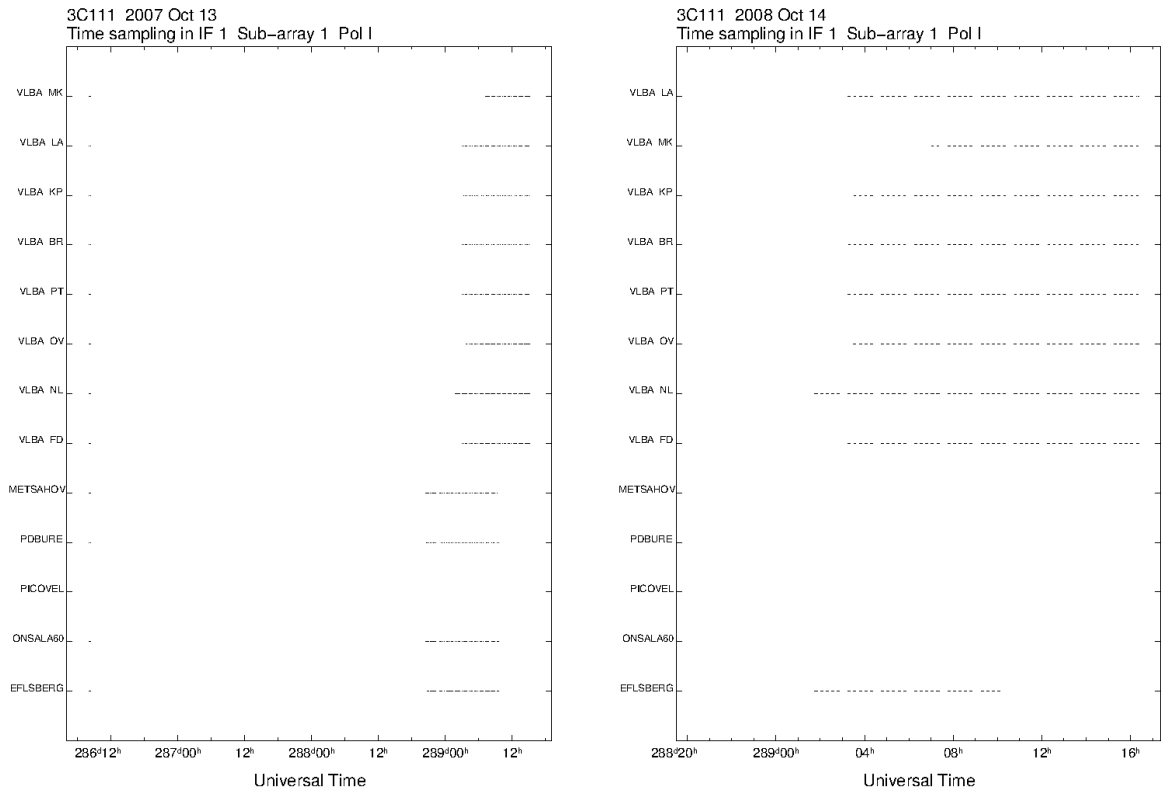
Figure 4.4.: Time sampling of the first (2007-10-15) and third (2008-10-14) from DIFMAP, after initial re-binning
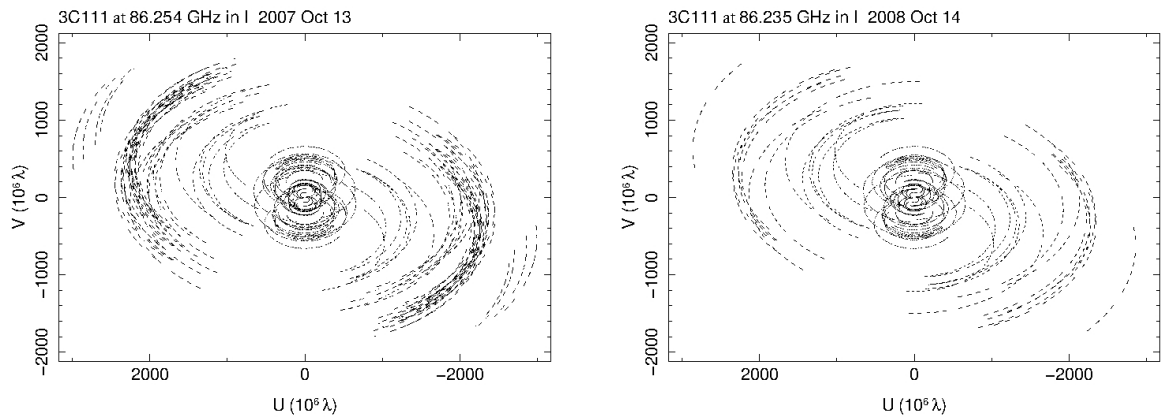

Figure 4.5.: (u, v)-coverage of the first and third GMVA observation from DIFMAP, after initial re-binning

4.3.2. Imaging and Self-Calibration

Following the procedure outlined in the previous section, separate data files for each source (3C111 and calibrator(s)) of each epoch can be further processed in DIFMAP. An introduction and overview of DIFMAP can be found in Shepherd et al. (1994), Shepherd (1997) and Taylor (1997). The process is structured into the following steps:

1. The data are averaged with a reasonable interval and the resulting data points have newly calculated errors. Furthermore, the size of the image and of its pixels as well as a weighting scheme for the visibilities are defined.

2. A model of the source, consisting of δ-functions, is constructed using the CLEAN algorithm and *phase self-calibration* alternately until a satisfying model is produced.

3. *Amplitude and phase self-calibration* are performed and outliers of the visibilities are edited. Until the residual flux reaches noise level, step 2 and 3 are repeated.

4. Otherwise, a final CLEAN-image can be produced.

Initial settings for the imaging process are set in step one. A re-binning of the data in DIFMAP is necessary, because the assigned errors for each data point by AIPS are unrealistically high. Therefore, DIFMAP computes the statistical error based on the averaged data within one bin. The integration time is chosen to be within the coherence length of the data, hence 10 s are used for all data sets.

The size of one pixel is determined to be small enough, that four to five pixels are covered by the minor axis of the synthesized beam. In order for the image to contain all relevant structure of the source, the number of pixels are ascertained in the first trials. A map size of 2048 pixels[8] with a cell size of 0.01 mas were chosen for imaging 3C111.

Imaging of VLBI data usually utilises two different schemes. In *natural weighting* the visibilities are weighted according to their distribution in the (u,v)-plane. This produces images with the highest sensitivity, because the density of data points is usually higher on shorter baselines in most interferometers. Contrary, *uniform weighting* leads to the best resolution, because it accounts for the density distribution of the visibilities. To this purpose, a binning of two pixels is chosen. In addition, the amplitudes are weighted by their error to the power of -1. 3C111 was imaged using both weightings.

Before continuing with the next step, it is instructive to take a look at different plots. The UVPLOT function in DIFMAP shows the sampling distribution of the array (Fig. 4.5). RADPLOT displays all visibilities projected on the (u,v)-radius, whereas PROJPLOT reveals the visibility distribution along a particular (u,v)-radius. The latter is especially helpful in gathering initial information on the extend of the source (Fig. A.1). TPLOT shows at which time over the complete observation, data exists (Fig. 4.4).

---

[8]DIFMAP allows only values such 2^n for the pixel number

Modelling the visibilites with δ-functions represents the essential part of creating an image of the source (step 2). It is based on *difference mapping* using the CLEAN algorithm by Högbom (1974)[9], which is in turn applied to the data with phase self-calibration.

CLEAN is a solution to the deconvolution problem, i.e. finding the true intensity distribution, which, convoluted with the synthesised beam of the array, yields the "dirty" image (Sect. 3.3). The "dirty" image itself is a convolution of the source model with the "dirty" beam, i.e. the sampling function of the array. The purpose of CLEAN and of difference mapping is to model the source with the "dirty" image without making assumptions of the absolute value of the source's intensity. Hence, a point source of 1 Jy at the centre of the map is set at the beginning. Now, CLEAN creates a model component and assigns to it a fraction of the peak flux density in the "dirty" image. The reloaded "dirty" image, which may now be designated as the *residual map*, shows this new component and remaining flux. If the new intensity peak is located at the position of the component, it will be updated. Otherwise, a new component at the coordinates of the peak will be created. The fraction of flux, which is subtracted from the peak intensity, as well as the number of iteration, in which CLEAN will search for new components, are defined by the user. The former is known as the *loop gain*.

Even after the calibration of the phases in Subsect. 4.3.1, residual errors remain. The quality of the fit is improved with the help of closure phases, i.e. within a triangle of antennas station-dependent errors cancel each other out (Sect. 3.3). The phases of the visibilities are fit to the model on the condition that the closure phases remain constant. This is called phase self-calibration.

CLEAN and phase self-calibration is repeated until the increase in flux density is not significant any more. For the purpose of enhancing the convergence, CLEAN-windows are drawn in the image plane around the location of flux related to the source. CLEAN will only proceed within these windows. The difficulty in defining this area is twofold: First, it is possible to allow CLEAN to build a model, which would deviate from the actual source. This can be circumvented in part by checking the quality of the fit to the visibilities and setting windows only at those positions, where the peak flux is significantly above the noise level of the residual map. The latter introduces a certain bias in the structure of the source, which yields the second difficulty. However, cross checking with available data of images at this or other frequencies helps. For 3C111, the existing data base of the MOJAVE program and BG monitoring provide a lot of support. Nevertheless, the better resolution of the GMVA data resolves structural details, which cannot be seen in other images. Therefore, a lot of care and repetition go into finding a good CLEAN-model. Another advantage of restricting the area for model components is that it prevents CLEAN to take flux into account, which comes from calibration errors. The size of these windows is varied on purpose. At earlier stages of the imaging process

---

[9]Variations of the original algorithm by Högbom (1974) as well as alternatives exists, but are not available in DIFMAP

larger windows allow for as much flux as possible to be included, while after further amplitude and phase self-calibration smaller windows yield better stability.

Before continuing with step three, a taper in form of a Gaussian function is often applied, which weights down visibilities at longer baselines. If prominent diffuse emission becomes visible in the tapered "dirty" image, using CLEAN may improve the fit. Though, the quality of the fit has to be watched intensively, because too much CLEANing will destabilise the fit especially at longer baselines.

It is possible that CLEAN creates components with negative flux. While they are physically wrong, the convergence of CLEANing sometimes benefits from them as long as their fraction remains minimal and they are evenly distributed.

Amplitude and phase self-calibration (step 3) utilises the existence of closure relationships for a closed loop of four and three stations to perform an amplitude and phase self-calibration, respectively (Subsect. 3.3.2). The amplitude and phase of the visibility are changed to better fit the model, depending on the closure relationships and solution interval. The interval is set to the full length of the observations and is subsequently decreased. In principle, the first interval leads to one correction factor for each telescope applied to all of its data. Therefore, a special function (GSCALE) is available in DIFMAP. Because of the sub-arraying condition of the GMVA, it was not used. Instead, the first solution interval was set to 720 min, which represents the approximate time of observation of each sub-array. Consecutive intervals were 180 min, 60 min, 20 min, 10 min, 5 min, 1 min and 0 min. The 0-min-interval means that each data point is fitted independently in time. CORPLOT is used regularly to find out, how the gain factors of the amplitude vary for each station. In case of strong outliers, the data of this telescope were inspected. Prior to each self-calibration step, negative components are deleted from the model.

Each time, when amplitude and phase self-calibration were performed, the visibility and the fit are inspected using either VPLOT, RADPLOT and/or PROJPLOT. VPLOT displays the amplitude and phase distribution in time for one particular baseline and, if available, for a particular IF. This depiction is especially helpful in editing corrupt data points in detail, while the other plotting function allows to better determine, whether data from complete stations are infected. Additionally, early editing is performed after an initial model was constructed in order to enhance the model quality before the first amplitude self-calibration.

This is probably the most critical step throughout the whole imaging process. All correction factors obtained by self-calibration are directly applied to the data (contrary to AIPS). Therefore, amplitude and phase self-calibration can force the data to fit the model, emphasising the importance of taking good care of step two. In addition, the self-calibration routine in DIFMAP was set to flag all data from station, which could not be connected with two or three other stations. DIFMAP only provides a function to reverse the last self-calibration step. Therefore, settings, model and data are continuously saved

at crucial stages (e.g. after editing data, before and after amplitude self-calibration). A cross check is available such that the total flux should remain roughly constant before and after self-calibration.

Amplitude self-calibration has the huge advantage that with subsequent shorter intervals, the model improves and the noise level decreases until it reaches approximately the thermal noise level. This in turn, allows weaker emission from the source to be detected in the "dirty" image. After each self-calibration, the process of building a model is repeated from step 2, except after self-calibration with zero solution interval.

The final CLEAN-image   (step 4) is obtained after the last amplitude and phase self-calibration. It consists of final editing and CLEANing as described in step two and three, respectively.

Once the final model is conceived, all windows are deleted. A CLEAN with a high number of iterations, but small loop gain is performed on the complete map, followed by one phase self-calibration and one last CLEAN with the same settings. This improves the overall image fidelity.

The CLEAN-image can be constructed by convolving the model's intensity distribution with the CLEAN-beam and adding the noise from the residual map. The CLEAN-beam is a fit of an elliptical Gaussian distribution to the "dirty" beam. The CLEAN-image represents the resulting intensity distribution of the source. In fact, it is helpful to check the development of the CLEAN-image throughout the modelling and self-calibration process. However, this should not be done too early to prevent biasing the source structure.

At this point, the quality of the image is checked by loading the original data together with the model. If the model is higher than the data suggested, it may be due to too much CLEANing. Single-dish measurements provide a cross-check of the total flux density. In addition, the residual flux in the "dirty" image should be evenly distributed. Noise in the CLEAN-image should not show particular symmetric or asymmetric features. However, due to the imperfectness of array such as the GMVA, the complexity of this and the previous calibration process, residual errors cannot often be prevented. In this case denser, homogeneous arrays have an advantage. Taylor et al. (1999) provides a reasonable start into the vast topic of error recognition in VLBI images.

Imaging of the GMVA data   differed in its demands from epoch to epoch.

The first and second epoch were particular problematic concerning the total flux of the CLEAN-image. The total flux of the CLEAN-image differs from the expected single-dish value by a different amount (see Sect. 5.1). Therefore, it is unlikely to be a systematic issue.

The third epoch contained the least number of telescopes (VLBA+Effelsberg) after finishing the a-priori calibration. Nevertheless, the visibilities of Fort Davis and North Liberty of the VLBA stations were below the average of the other stations at the same

baselines, which is why they were flagged. This significantly improved the image fidelity. It was less difficult to reach a total flux close to the single-dish value and to image the data compared to the other two epochs.

All three epochs were imaged by setting a few small additional windows in the opposite direction of the jet structure, though close to the core. This not only improved the stability of CLEAN, but was sometimes even necessary due to residual flux. Due to the high resolution of the GMVA, a small elongation is visible in this direction, most notably in epoch two and three. A discussion of this structure, in particular in the context of a possible counter-jet or the brightest feature not being the core, is featured in Chapt. 5.

A summary of relevant image parameters is given in Tab. A.1.

The set of 43 GHz data contains 15 epochs from June 2007 to February 2009.

The data had already been imaged and self-calibrated by the Blazar group. The visibility data and CLEAN-model were publicly available. However, all provided CLEAN-maps were somehow shifted in coordinates. Thus, new CLEAN-images were produced by loading the visibility and CLEAN-model into DIFMAP. A pixel size of 0.03 mas was chosen, allowing at least three pixel to be covered by the minor axis of any beam from each epoch, while the number of pixels were set to 1024. A complete list of all image parameters is given in Tab. A.5.

4.3.3. Model-fitting

The final part concerns the analysis and modelling of the self-calibrated data and is refer to as *model-fitting*. The basic principle is to define a model depending on a certain number of parameters and to fit this model to the visibility distribution. Model-fitting can be used as an independent way of analysing uncalibrated VLBI data, but this is not done here. A general introduction is given for example by Pearson (1995). In the context of this thesis, model-fitting is used as an addition to imaging with CLEAN and self-calibration in order to gain better quantitative information on the jet morphology. The fixed number of parameters for the model allows the user to compare much better the model-fits from different epochs with each other.

In DIFMAP, a model component[10], as it is used in this thesis, is described by the following set of parameters[11]: Flux (in Jy), radial distance from the core (mas), position angle (deg), major axis of the component (mas), axial ratio of the component (mas), position angle of the component's axis (deg). DIFMAP permits circular and elliptical Gaussian components as well as δ-components to be used for model-fitting. Depending on the type of component used, not all parameters are variable, i.e. for a circular Gaussian component the axial ratio is fixed at one.

---

[10]In the context of CLEAN as described in Subsect. 4.3.2 the term "model component" always designates a delta function. However, this is not necessarily the case for the technique of model-fitting.

[11]In principle DIFMAP allows additional parameters such as a spectral index e.g. in case of multi-IF data, but those are not used here and hence they are neglected.

The fit is performed by the method MODELFIT, which employs the Levenberg-Marquardt least square fit algorithm (Levenberg 1944). The quality of the fit is given by the reduced χ^2. In general, the technique is applied under the assumption that the data are well calibrated. However, even after careful imaging and self-calibration, residual errors in the phases of the visibility may remain. Thus, phase self-calibration is carried out after a certain number of iterations of MODELFIT, which improves the stability of the model and supports its convergence.

A number of issues have to be addressed in order to properly assess the validity of the derived model: First, the set of parameters, which describe the model, are certainly a reasonable choice, but are not the only one. Second, there is not just one model, which can be derived with these parameters to describe the data. It strongly depends on the goal for the analysis and is, thus, subject to the researcher. Therefore, consistency in the way the model-fits are produced is essential: In this thesis, the components of the model for the GMVA and the BG data fulfil the following conditions:

C1. All model components consisted of circular Gaussian components.

C2. A component was generally considered to be invalid, if the flux becomes negative, the position deviated from the CLEAN-image of the jet, the size of the component became infinitesimal small.

Two approaches were taken to fit the data:

A1. Each epoch was modelled independently at first, by adding component after component in the residual map.

A2. A model from a previous or consecutive epoch was applied. If components of this model became invalid, they were deleted, until a stable model was reached. If necessary, new components were added iteratively in the residual map.

Components were added as long as significant flux remained at a position, which coincided with a feature in the CLEAN-image. Each time a new component was created, several iterations of MODELFIT and phase self-calibration were performed until either a component becomes invalid or the parameters of the model components are approximately stable. Only after the fit was stable, a new component was added, if necessary. The number of components was increased in order to describe the jet as detailed as possible using only circular Gaussian components. In addition, the overall quality of the model was judged by the following criteria:

Q1. No parameter was fixed, when MODELFIT was carried out, except if it was due to the nature of the component.

Q2. The model-fit should resemble the morphology of the jet in the CLEAN-image as detailed as possible, depending on A1 or A2.

Q3. The χ^2-value of the model-fit should be close to the CLEAN-model.

Q4. The total flux of the CLEAN-map should be matched by the model.

The CLEAN-map of the model-fit may deceive, because the map is not created by the CLEAN-model, which is taken to be the "best" approximation of the true intensity distribution. Therefore, Q2 is tested by plotting the model-fit over the CLEAN-image. Q4 cannot always be met, because each new Gaussian component changes the parameters of all others, including the flux of each component. A certain amount of deviation cannot be prevented. As stated before, it is important to remember, that a stable model obeying Q2 and Q4 with less or other types of components than another fit is not wrong per se. It is above all a different representation of the underlying visibility distribution.

The approach to model-fitting the GMVA and BG data in the form of A2 naturally improves the comparison of different epochs. This is especially helpful for a kinematic analysis, in which the movement of one component is tracked by associating it with another one in a subsequent or previous epoch. Nevertheless, it biases the fit by assuming structural similarities between two epochs. Therefore, fits obtained by A1 differed from those by A2 for the GMVA as well as the BG data.

All models presented in the next chapter are based on A2, i.e. using neighbouring models as starting point. The BG models were obtained first. Then, the fit of the GMVA model began by taking a neighbouring BG model. Although, this method might bias the GMVA model in terms of the BG one up to some degree, it was always necessary to delete a certain number of components and create new ones. Thus, the GMVA model-fits can still be considered separately from the BG fits.

The BG epochs were imaged with uniform weighting. Hence, the same weighting was used to model-fit them. In contrast to that, the model-fits for the GMVA data were based on natural weighted imaging data. Since the sensitivity of VLBI observations decreases at higher frequency, it is a reasonable approach. Recently, Chatterjee et al. (2011) published a kinematic analysis of components above 100 mJy. Instead of using these models, new fits were obtained to compensate for the ambiguity of the process. A cross check with the results of Chatterjee et al. (2011) will be performed in Sect. 5.2.

The analysis of uncertainty of the model parameters is complicated by the facts, that DIFMAP does not provide any means to determine intrinsic positional or flux density errors. In fact, it is in general not trivial to obtain errors for these parameters, because the model highly depends on the fidelity of the underlying calibrated data (Lister et al. 2009) and Fourier transformations are involved.

In case of the GMVA data, it was particularly helpful to constrain the model with the CLEAN-image. In addition, the stability of a new component was sometimes improved by simultaneously adding another one at a reasonable (in terms of flux), but not necessarily close, position.

5. Results and Discussion

The broad-line radio galaxy 3C111 was observed with the Global mm-VLBI Array (GMVA) at 86 GHz in October 2007, May and October 2008 following a major flux density outburst around mid-2007 above 10 Jy at mm wavelenghts (Fig. 4.2). The obtained images from self-calibration of the data are discussed in Sect. 5.1.

In addition, circular Gaussian components were fitted to the self-calibrated data of each epoch to study the movement of features in the jet Subsect. 5.2.1. However, three epochs prevent a robust kinematic analysis, for which five are needed (Lister et al. 2009). Therefore, publicly available self-calibrated data of 3C111 at 43 GHz obtained with the VLBA between June 2007 and February 2009 by the Blazar Group[1] (BG) were model-fitted as well. A kinematic analysis of a total of 15 available 43-GHz-epochs was performed (Subsect. 5.2.2), which allow to put constrain on the quality of the 86-GHz-analysis and a possible core shift (Sect. 5.3). This chapter concludes with a discussion of jet precession and collimation at 43 and 86 GHz.

The low redshift $z = 0,049$ of 3C111 (Eracleous & Halpern 2004) translates into linear scale[2] of 1 mas = 0.95 pc, assuming a cosmological model with a Hubble constant of $H_0 = 71 \, \mathrm{km \, s^{-1} \, Mpc^{-1}}$ and the density parameters $\Omega_m = 0.27$, $\Omega_\Lambda = 0.73$.

5.1. Imaging

The images gained by naturally weighting of the visibilities are depicted in Fig. 5.2 and Fig. 5.3 and are primarily used throughout the following discussion. The latter magnifies the inner 2 mas of Fig. 5.2. The same magnification is chosen for Fig. A.2, which displays all three images after self-calibration with uniform weighting. A complete list of relevant image parameters is given in Tab. A.1. The size of the elliptical CLEAN-beam defines the lower resolution limit in each epoch. The natural weighted CLEAN-beam varies from (0.15×0.045) mas (major axis times minor axis in mas) in the first epoch (2007-10-15) to (0.17×0.067) mas in the third epoch (2008-10-14) with an average of (0.16×0.057) mas for three epochs. This is about a factor of two for the major beam axis and about a factor 3 for the minor axis better compared to the 43 GHz VLBA data (Subsect. 5.1.4).

The total flux S_tot of the self-calibrated images differs from the expected value $S_\mathrm{86,SD}$ from the F-GAMMA light curve (Fig. 4.2). The CLEAN-model from both weighting schemes of the first epoch contains ∼8.1 Jy of expected ∼12 Jy (from 2007-10-09) and

---

[1] http://www.bu.edu/blazars/VLBAproject.html
[2] http://www.physics.purdue.edu/astro/MOJAVE/sourcepages/0415+379.shtml

the second GMVA epoch yields ∼1.9 Jy of ∼4.1 Jy (2008-05-02). This is a discrepancy of ∼30 % and ∼50 %, respectively. The third observation is the exception with ∼3.8 Jy (natural weighting) and ∼3.6 Jy (uniform weighting) of an expected ∼4.1 Jy (2008-10-07), which is a difference of ∼10 %. It is currently not clear, why the CLEAN-model of the first and second epoch does not reach the expected flux density. Although it was possible to reach a total flux density close to the single-dish value prior to the first amplitude-self-calibration, the flux denisty decreased in subsequent steps. In addition, several baselines in all three observations show variability in the amplitudes ranging up to a few Jy, which are not just fluctuations of a single scan and have a slope over several scans. Even after flagging these data points in favour of visibilities with a high flux and stable phases, the improvement of the model in terms of the flux density was not significant and only minor changes in the jet morphology were observed. Therefore, the calibrated data used in the following discussion and subsequent kinematic analysis were gained after conservative flagging of the visibilities and phases.

The 1st 86-GHz-GMVA epoch reveals a bright and compact core with extended structure up to ∼ 1 mas (top panel in Fig. 5.2, Fig. 5.3). Throughout the second (2008-05-11) epoch the jet evolves and expands radially at an angle of about 60° to the north east (middle and bottom panel in Fig. 5.2, Fig. 5.3). Because of the well-resolved structure of the 86-GHz-jet, the jet is visually divided into three distinct parts as illustrated by an image of the second epoch in Fig. 5.1:

1. The "central region" contains emission within |0.2 mas| (∼0.095 pc) relative right ascension (R.A.) from the origin.

2. The "inner jet" includes emission, which exhibits a direct connection to the central region with only minor gaps. Hence, it extends from 0.2 mas to 1 mas in epoch one and up to 2 mas in epoch three.

3. The "outer jet" denotes distinct emission features further down the jet stream, which becomes more important in case of the 43-GHz jet.

The different parts are examined in the following subsections. While a detailed analysis of the jet morphology and evolution is conducted as part of Sect. 5.2, a qualitative discussion is instructive already at this point.

5.1.1. The Central Region

In the first epoch, the central region exhibits the strongest emission, with its maximum localised in an area smaller than the beam size, but extended emission is visible. This is consistent within all three observations (Fig. 5.3). However, the flux density varies especially in comparison with the jet. In the third epoch, the contrast between emission in the central region and the rest of the jet is most pronounced. Almost all the emission comes from within the central region. The light curve in Fig. 4.2 indicates that the
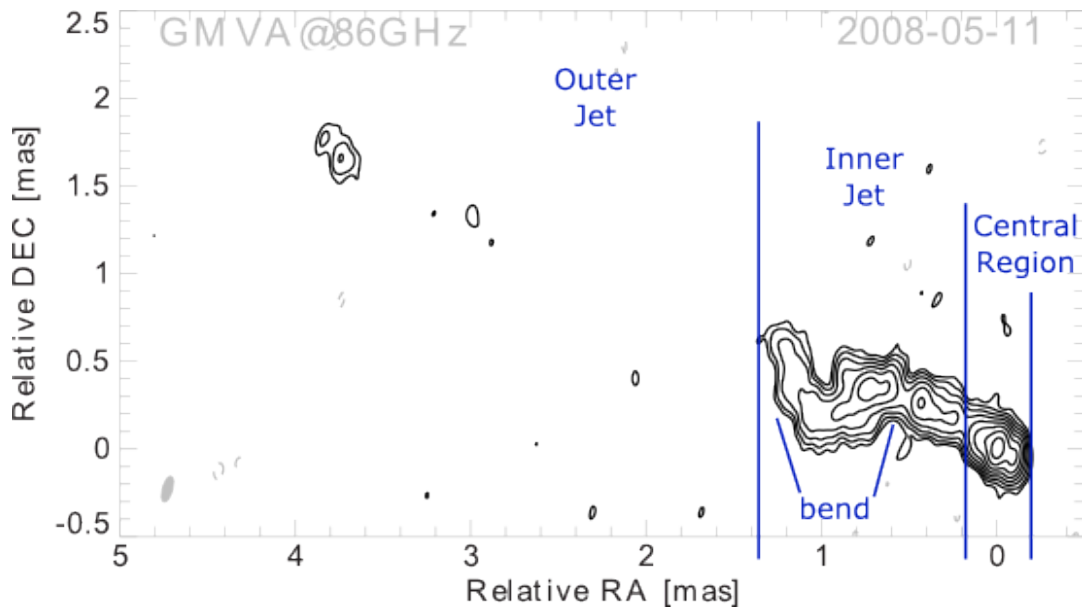
Figure 5.1.: 3C111 image from the 2nd GMVA observation (2008-05-11) at 86 GHz as an example of the three main parts of the jet as they are discussed in the text, i.e. a central region (including the core), an inner jet and a (diffuse) outer jet. This division is used for the jet at 86 and 43 GHz (BG data). In addition, the bend is most prominent in this epoch and indicated as well. The lowest contour levels are set to 3σ of the rms noise, increasing logarithmically by factor of two.

measurements were performed on a rising slope of flux density. It seems that the increase in emission is localised inside this part of the jet.

Furthermore, the position angle with respect to the point of origin of the extended emission in the central region seems to change from the first to the subsequent epochs. In contrast to that, the alignment of the central region seems to be almost unchanged between the second and third epoch. In both cases the orientation seems to be aligned with the inner jet (except for the bend, see Sect. 5.4).

An equally interesting feature is the emission in opposite direction from the jet (white arrows furthest to the right in Fig. 5.3). It is most noticeable in the second epoch and least in the first one. Naturally, the question arises, whether this could be a counter jet. There is, however, currently no report in literature on the confident detection of a counter jet in 3C111. Another possible interpretation considers this feature as the region, where the jet emission at a particular frequency (here 86 GHz) becomes optically thin (T. Krichbaum, private communication). The challenge in assessing, whether it is a real feature is the ambiguity in the CLEAN process, discussed in Subsect. 4.3.2. It was possible to obtain images, where this region was much smaller, but the image quality was lower in these cases. In all three epochs, the imaging process was improved, when allowing DIFMAP to CLEAN in this region. Therefore, it is considered to be genuine. As Sect. 5.2 will show, the feature was defined as the core. However, such a shift is not incorporated into Fig. 5.2, Fig. 5.3 and Fig. A.2.

5.1.2. The Inner Jet

A remarkable feature is the bend clearly visible at ~ 0.50 mas relative in the first epoch. The structure begins ~ 0.2 mas relative R.A. away from the point of origin and shapes the complete jet morphology. Seven months later this feature has moved as far as ~ 1.0 mas relative R.A. in the second epoch. Another five months later it is localised at ~ 1.5 mas, where it has merged into one larger structure (Fig. 5.3).

The top panel in Fig. 5.3 demonstrates, that the inner jet in this epoch can be decomposed into at least three distinct and strong features at around 0.3, 0.4 and 0.6 mas relative R.A. (three white arrows from the left). The picture changes in the second epoch. An elongated stream of jet plasma connects the bend and the central region in a rather straight line. The emission in the bend itself is more or less smeared out and decreases further out. The brightest feature is localised at the beginning of the bend (~ 0.7 mas relative R.A., left arrow) and seems to exhibit even stronger emission than the intermediate region. In the jet stream of the third epoch, which connects the larger structure at the end and the central region, two to three faint features are visible at about 0.4, 0.6 and 1 mas relative R.A.. Even though the structure at ~ 1.5 mas does not resemble a bend any more, at roughly three distinct features may be identified.

The travelled projected distance of the bend is ~ 1 mas, which leads to an estimated apparent velocity of ≈ 3 c. The underlying assumption in this case is that the bend in each epoch consists of the same plasma flow and not newly ejected material. The

distance between the bend and the core increases with each epoch and thus the apparent velocity of new ejecta to create this shape would have to be $\sim 5\,c$ for the second and even $\sim 10\,c$ for the third epoch. The latter value is much higher than the highest value detected so far at 15 GHz (Kadler et al. 2008) and 43 GHz (Chatterjee et al. 2011). Even the assumption, that the bend of the second and third epoch resemble the same structure, is not likely. This would require the movement of the feature to be slowed down significantly, which has not been reported so far (see Jorstad et al. 2005, Kadler et al. 2008). The determination of the interrelationship of these components will be the main goal of the next section.

While it was possible to gain some flux in the gap of the bend by allowing DIFMAP to CLEAN there, it did not seem to improve the image quality. Even when full CLEANing of this space was allowed throughout the whole self-calibration procedure, the central morphology of the bend and jet flow did not change, though the jet emission smeared out perpendicular to its orientation. Therefore, it was disregarded for the moment.

5.1.3. The Outer Jet

The region beyond the inner jet is surprisingly featureless in all three epochs although residual emission in this area was imaged with tapered baselines. Hence, this abrupt termination is likely to be true. The features are indicated with white arrows in Fig. 5.2. They are both aligned with the inner jet structure. Additionally, the features overlap with emission at 15 GHz[3] and 43 GHz[4].

The two regions are a good example of how self-calibration improves the detection of faint structure. In the case of epoch two and three the emission appeared in an advanced stage of the self-calibration process. Hence, in a rerun of the calibration process, it was DIFMAP allowed to CLEAN there from the beginning.

5.1.4. Comparison with Mojave and BG maps

average BG beam $(0.31 \times 0.17)\,\mathrm{mas}$

An impressive demonstration of the improvement in resolution of the GMVA data with respect to other observations offers Fig. 5.4. Here, an image of the first 86-GHz-GMVA epoch (bottom panel) is combined with the closest MOJAVE image (15 GHz, VLBA, top panel[5]) and BG map (43 GHz, VLBA, middle panel) in time. The dashed lines indicated the area, which is magnified with increasing frequency (and (u, v)-coverage). The size of the CLEAN-beam at 15 GHz is (0.90×0.56)mas and at 43 GHz (0.39×0.21)mas compared to $(0.15 \times 0.045)\,\mathrm{mas}$ at 86 GHz with the GMVA.

---

[3] http://www.physics.purdue.edu/astro/MOJAVE/sourcepages/0415+379.shtml

[4] http://www.bu.edu/blazars/VLBAproject.html

[5] Because the MOJAVE program provides self-calibrated FITS-data files of the CLEAN-image, it was only necessary to plot the data in the required format.

The 15-GHz-jet extends straight from the core with no bend visible at this level. Interestingly, the angle of the jet stream at 43 GHz changes a bit after $\sim$0.8 mas. Prior to this change, a bend within 0.5 mas as in the 86-GHz-map is not visible. Although the orientation of the core region differs significantly from the other two epochs, the jets of all three epochs are aligned.

43 GHz Jet Morphology   The evolution of the jet morphology as depicted by the BG data between June 2007 and February 2009 likewise exhibits dramatic changes (Chatterjee et al. 2011, see also contour plots in Fig. 5.9 and Fig. 5.10). A complete list of important image parameters is listen in Tab. A.5 (see Subsect. 4.3.2) The division of the jet morphology, as it was done in the last section, can be applied here again. Subsect. 5.2.2 will show that the core is not identified with the brightest feature, but a bit further to the west.

A misalignment of two parts in the jet is detected until January 2008. However, it does not occur at the same position as in the images at 86 GHz. There, the change in position angle takes place between the core and the inner jet, whereas at 43 GHz it happens at a transition region, where the already weak flux is further depressed. In these epochs, the region is located around $\sim 0.8 - 0.9$ mas.

In the first epoch (2007-06-13) the inner jet extends as far out as ~ 1 mas, moving out to ~ 2.2 mas in the last observation (2009-02-22). The bend, prominent in all GMVA epochs, is visible as early as epoch six at of the 43-GHz-BG data (2007-11-01). While the intermediate region between the core and the bend shows variable substructure, the bend itself is conceived merely as one large structure.

It is important to note, that the 43 GHz images indicate at least four ejections over a period of 1.7 yrs. The last ejection, which seems to occur between epoch 12 and 13 (2008-11-16, 2008-12-21) is especially interesting. As stated before, in the last GMVA epoch the jet became weak and almost all flux was concentrated in the core. The light curve at 86 GHz in Fig. 4.2 shows, that this observation was taken at a rising slope in flux density with its maximum probably around November 2008. However, the F-GAMMA light curve data at 43 GHz available in our group does not contain any data between August 2008 and July 2007, but the total flux density of the CLEAN-map increased up to $\sim$6 Jy, which is within errors of the 86-GHz-maximum in 2008-11-07 ((6.71 ± 0.76) Jy). An ejection of new matter into the jet stream is apparent in the 13th epoch (2008-12-21) at 43 GHz. Prior to this, the jet weakens and the emission in the central region increased from epoch eleven (2008-09-10) to 12 (2008-11-16).

The outer jet structure at 43 GHz begins around 1 mas in the first and 2.2 mas in the 15th epoch. This does of course not mean, that no emission exists at 86 GHz, but optically thin emission decreases with $\nu^{-\alpha}$ (Sect. 3.1.2), falling below the sensitivity of the array. These features are not part of Chatterjee et al. (2011), but will be analysed in the next section as well.
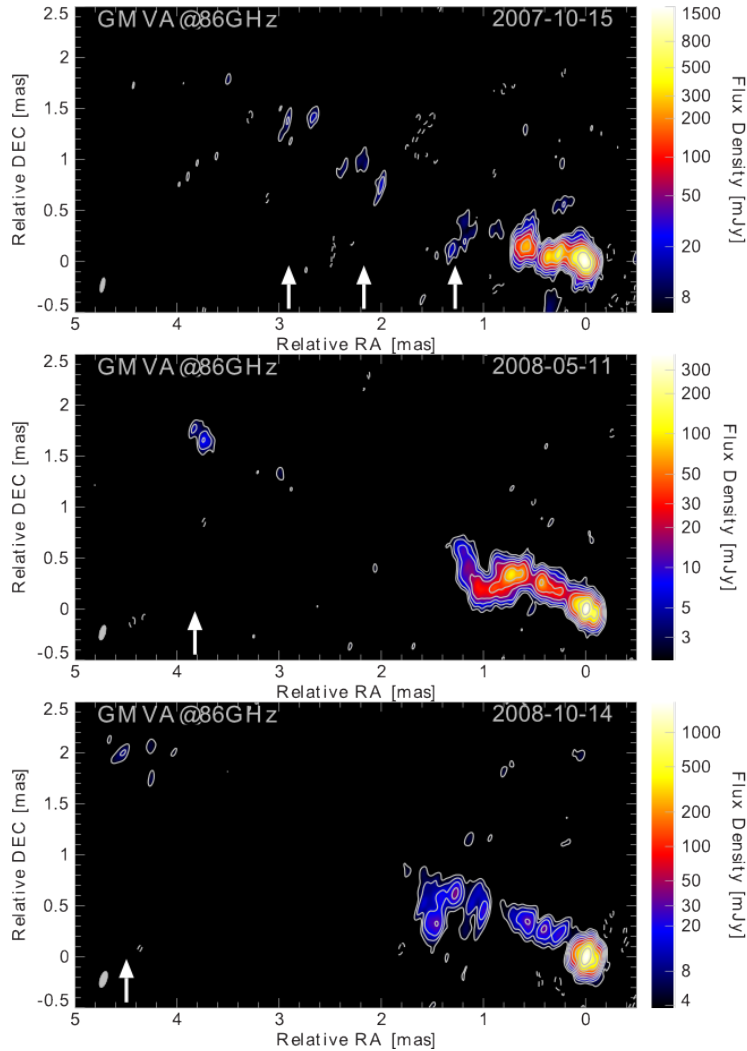
Figure 5.2.: Images of 3C111 at 86 GHz from the first (top), second (middle) and final third (bottom) GMVA observation with natural weighting. The spacing of the images is uniform and not scaled to the temporal separation of the observations. The colour code indicate the flux density in units of Jy/beam. The lowest contour levels are set to 3σ of the rms noise, increasing logarithmically by factor of two. Tab. A.1 lists all related image parameters. All three images are convoluted with their intrinsic beam, i.e. $(0.15\text{x}0.045)$ mas (top), $(0.015\text{x}0.60)$ mas (middle), $(0.17\text{x}0.067)$ mas(bottom).
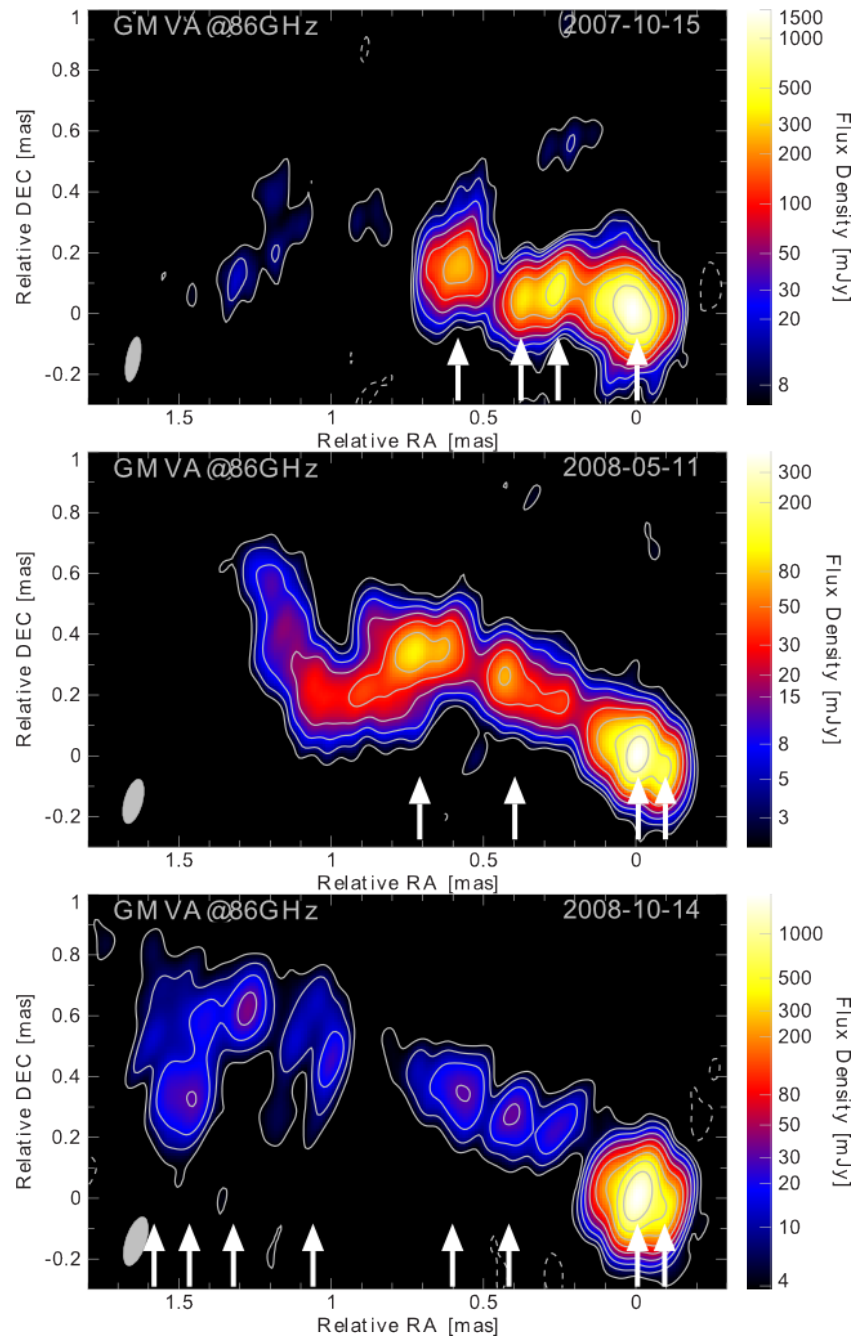
Figure 5.3.: The same setting as in Fig. 5.2, but the central region and inner jet are magnified, revealing the finer sub-structure in detail
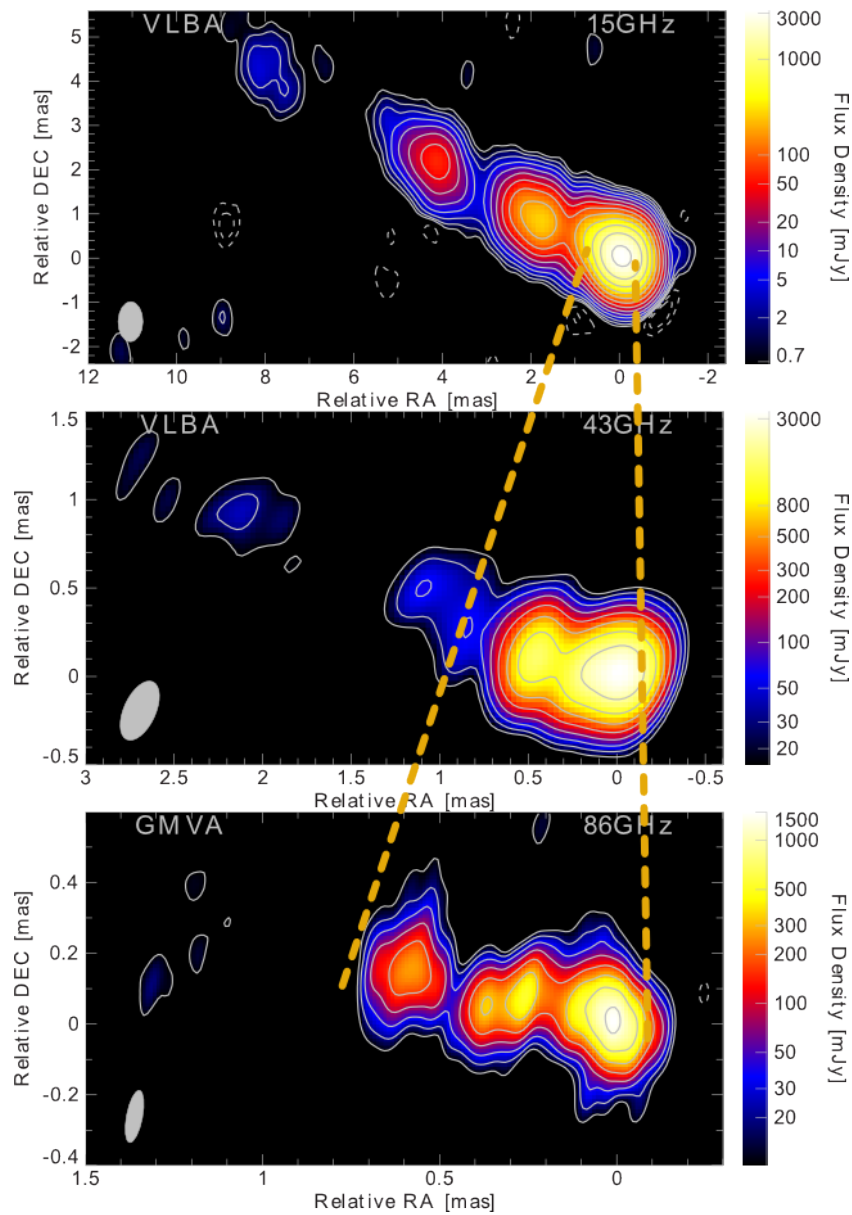
Figure 5.4.: 3C111 images at three different frequencies with the additional two maps being closest to the first GMVA epoch. Top: 15 GHz VLBA from 2007-06-09 (Credit: MOJAVE Team); Middle: 43 GHz VLBA uniform weighted image from 2007-09-29; Bottom: GMVA epoch one at 86 GHz from 2007-10-15 (natural weighted). The dashed lines indicates the zoom into the jet of 3C111 with increasing frequency (and coverage). The contour levels increase logarithmically by a factor of two with the minimum level set to 5σ.

5.2. Kinematic Analysis

Experience from large multi-epoch VLBI surveys such as the MOJAVE program and its predecessor shows, that a robust kinematic analysis requires one model-fitted component to be associated in at least five consecutive observations (Kellermann et al. 2004, Lister et al. 2009). Although, only three 86-GHz-GMVA observations are available, estimates for the kinematic evolution of the jet based solely on the GMVA data, are obtained. Following this discussion, the 15 43-GHz-BG epochs are used to constrain the kinematics of the source at 86 GHz by developing a self-consistent multi-epoch and multi-frequency model.

As Subsect. 4.3.3 elaborates, the modelling of the jet is first of all influenced by the type of components used, i.e the set of parameters, which describe them and their number. For this analysis, circular Gaussian components were used for all data sets, it is important to remember that there exists other ways to model the brightness distribution. The model-fits used for the kinematic analysis, were obtained for one epoch by taking a model-fit from a previous or succeeding observation as a starting point (approach A2 in Subsect. 4.3.3).

The association of model-fit components from different epochs is not done automatically. As the discussion in the previous section revealed, the comparison of the morphological development in CLEAN-images from adjacent observation, provide indications for possible associations. Features in the jet can be traced through model-fit components over successive epochs. The procedure works well for slowly changing and moving features, if the observations are close in time and if the image fidelity is roughly equal. Even in these cases the visual association becomes rapidly complicated with increasing number of components per image, i.e. the more detailed the jet is modelled. Therefore, it is sometimes helpful to accept a decrease in fit quality for an individual observation in order to improve the self-consistency of all epochs.

A first association was performed by comparing the model-fitted components overlapped with their corresponding CLEAN-image between two or more adjacent epochs. Additional cross checks were provided by plotting the radial distance from the core over time as well as the spatial distribution of all components. Furthermore, the flux density of components moving away from the core should decrease, but this is not known to be the case for 3C111 ((Kadler et al. 2008)). Another way to compare the flux density of components from different epochs is the brightness temperature T_b, which incorporates the full width at half maximum (FWHM) of the Gaussian components θ_{FWHM}. Since, only circular components are used, the equation for T_b ((Kovalev et al. 2005)) of a single component at wavelength λ reduces to

$$T_b = \frac{2\log 2}{\pi k_B} \frac{S_{\mathrm{Comp}}\lambda^2(1+z)}{\theta_{\mathrm{FWHM}}} \tag{5.2.1}$$

where k_B is the Boltzmann constant, S_{Comp} denotes the flux density of the component

and z is the redshift of the source. Associated components are primarily compared in terms of their brightness temperature distribution, because it compensates for the different FWHM of the model-fits.

The beam size of the image has to be considered in terms of resolving two closely spaced components. Here, the elliptical nature of the FWHM of the beam helps, if the components are distributed along the minor FWHM. Methods exist, which use intrinsic information of the image, such as the noise to increase the resolution beyond the image beam (e.g. (Lobanov et al. 2000), (Martí-Vidal et al. 2012)). However, this so-called *super-resolution* can generally not be carried much below 1/5 of the beam, but is not considered here.

Once a sufficient number of associations was reached, a linear regression fit was performed of the distance travelled by a particular component over time. Because DIFMAP does not provide any means of determining the uncertainties of the model-fit parameter, all model-fit components are weighted equally. Hence, the resulting errors of the fit parameter are statistical uncertainties and largely underestimate the components uncertainties. It is important to note, that linear motion is the lowest order approach. As stated in Sect. 2.3, acceleration has been observed in 3C111, but the low data density of the GMVA observation and the particularities of 43 GHz sampling makes linear regression an appropriate starting point.

For a better comparison especially of the associated components at 43 GHz, Tab. 5.2 lists the components relevant for this thesis from Chatterjee et al. (2011).

5.2.1. 86 GHz GMVA Data Only

Fig. 5.5 shows the evolution of the inner $\sim$2 mas of the jet at 86 GHz between October 2007 and October 2008. The position and size of model-fit components are overlaid on contours of the CLEAN-image. The separation of each image is scaled according to the time interval between observations. Components without any associations in other epochs are not labelled and coloured in grey. The difficulties in the imaging process of the GMVA observation influence the model-fit. The lowest contours of the underlying CLEAN-image was set at $10\sigma_{\text{noise}}$ for the first and $5\sigma_{\text{noise}}$ for the second and third epoch images, respectively. Components in the outer jet are weak and therefore not considered in the kinematic analysis.

An overview of all components contained in a model per epoch is listed in Tab. A.2 to Tab. A.4. A list of associated components, including the parameters of the linear regression fit is given in Tab. 5.1. Except for Fig. 5.5 and Fig. 5.7 all other plots connect associated components with a simple line from one data point to another. An interpolation scheme is used in the former plot, while the latter shows the linear regression fit of associated components.

The central region is composed of multiple components in all three epochs, accounting for the extended structure discussed in Subsect. 5.1.1. The core of the jet is defined to be

the model-fit component farthest to the west. All components were shifted accordingly and the models are thus aligned at this point. The parameter listed in Tab. A.2 to Tab. A.4 belong to the original model prior to setting the new point of reference. A complete list of all model-fit components for each epoch is given in Tab. A.2 to Tab. A.4 in order of radial distance from the core.

Component G1 was set to be the core of the radio jet at 86 GHz. The next association is labelled G2 and contains the generally brightest components. The model-fit of epoch one and three required two components in this region with a spatial separation below the minor axis of the CLEAN-beam. As a result, they were both considered for G2 in the linear regression fit, which yields a very low apparent velocity below the speed of light. Combined with the distant estimated time of ejection, G2 can be considered stationary. The existence of such components was suggested by Jorstad et al. (2005) at 43 GHz. The large errors result from taking the two close components in GMVA-1 and -2 into account for the linear regression.

The inner jet's most prominent feature is the bent as discussed already in Subsect. 5.1.2, changing strongly over the period of one year. This complicates the association of components.

The best association is given by the lower part of the bend in the form of G4. In addition, Fig. 5.6, which displays the relative distance in R.A. and declination (Dec) from the core, allows to track G4 back to the core almost linearly. In contrast to that, G3 and G5 are less well aligned and the linear regression fit is not as good as in the case of G4, especially G5. The combination of the GMVA and BG model-fits will better constrain the association of G4.

Component K6 in Chatterjee et al. (2011) coincides with the outburst in the middle of 2007 at 43 GHz with an ejection date of 2007.66 ± 0.09 and an apparent velocity of (4.18 ± 0.11) c. G3 and G4 are the most likely candidates to be the components associated with the outburst. At this point, they do not coincide with the ejection date and the velocity of K6 within their errors, which does not have to be the case at 86 GHz.

It is obvious from Fig. 5.5 and the CLEAN-images from the previous section, that a jet stream connects the core with the bent. It was assumed, that this jet stream can be traced with G6. However, the linear fit is only slightly better than for G3. It moves at the lowest apparent speed of all components. Based on the available data, an unambiguous association is not possible. Interestingly, G6 and G3 are consistent in the estimated ejection time with component K6 in Chatterjee et al. (2011) within their errors, but not regarding their apparent velocity. G6 and G3 demonstrate best the difficulty in identifying components, which belong together solely based on the three GMVA epochs.

The brightness temperature over time is shown for all associations in Fig. 5.13, whereas the evolution of the flux density is plotted in Fig. A.4.

Name	$v_{\mathrm{app,est}}$ [mas yr^{-1}]	$\beta_{\mathrm{app,est}}$ [c]	$t_{0,\mathrm{est}}$ [yr]	σ_{d} [mas]	counts
G2	0.006 ± 0.028	0.018 ± 0.087		0.028	5
G3	1.19 ± 0.15	3.70 ± 0.48	2007.54 ± 0.11	0.11	3
G4	1.1923 ± 0.0039	3.696 ± 0.012	2007.4233 ± 0.0031	0.0027	3
G5	1.208 ± 0.046	3.74 ± 0.14	2007.225 ± 0.044	0.032	3
G6	0.620 ± 0.077	1.92 ± 0.23	2007.55 ± 0.11	0.054	3

Table 5.1.: Associated components at 86 GHz from all three GMVA epochs are listed with apparent velocity and time of ejection derived from a linear regression in the radial-distance-time-plane. The errors are calculated from the errors of the fit parameter. The asterisk denotes that two components in the first and third epoch are identified G2. $v_{\mathrm{app,est}}$ denotes the estimated apparent velocity of the component and $t_{0,\mathrm{est}}$ its estimated ejection time. As only three epochs are available the results have to be considered as estimates (Lister et al. 2009). σ_{d} is the standard error for each component with respect to the linear regression fit

G1 and G2 evolve almost similar in terms of their brightness temperature, with G2 being the stronger component of them both. In the first two epochs both decrease similar to the other four components, but in the third one, their brightness temperature increases contrary to the other components. Since this epoch was taken prior to another peak in flux density, which was lower than the outburst in 2007, it becomes clear that the increasing flux density is currently confined within the region of G1 and G2, with G2 still being the stronger component. The similar distribution of the brightness temperature in time of both components supports, that G1 is not a possible counter-jet feature, but in fact the region, where the 86-GHz-jet becomes self-absorbed.

Another interesting behaviour is exhibited by G3, which has a higher T_b-value G6 in the first two epochs although G3 is located further away from the core than G6. G3 is the brightest moving component, which suggests that it was ejected after high flux density outburst.
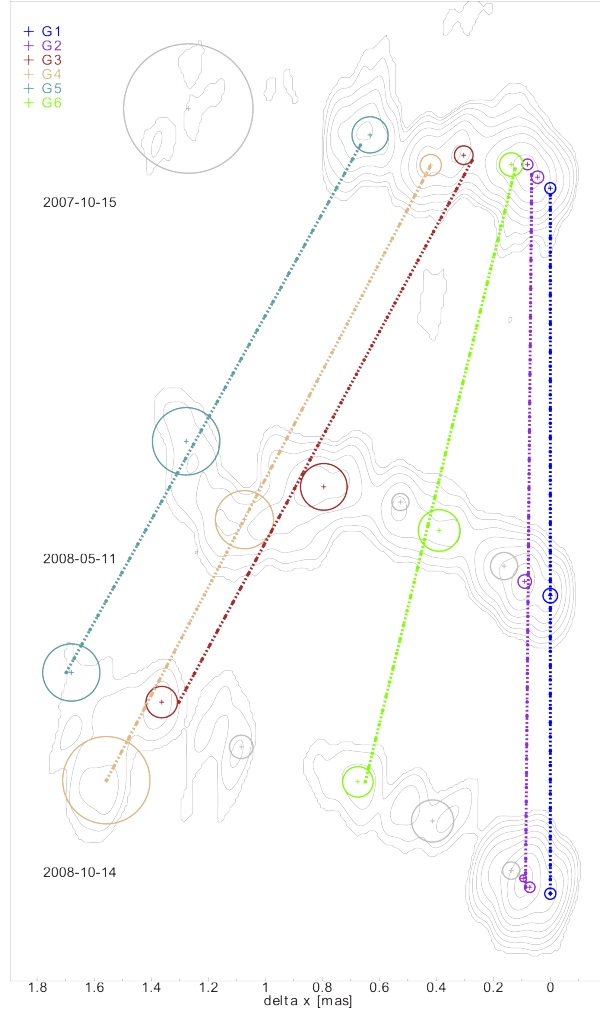
Figure 5.5.: Time evolution plot of CLEAN-images and model-fits of 3C111 at 86 GHz based on the GMVA observations. Associated components possess the same colour with their designation shown in the legend in the top right corner. The reference point for each contour plot and overlayed model-fits is the core identified as G1 (dark blue), which is set to zero distance in all epochs. The dashed line indicates an interpolation of associated components. The separation of each epoch is scaled accordingly. Due to the fidelity of the CLEAN-images the lowest contour lines for the first epoch are set to 10σ and otherwise 5σ of the rms noise. Components, which were not associated and are located further away from the are left out.
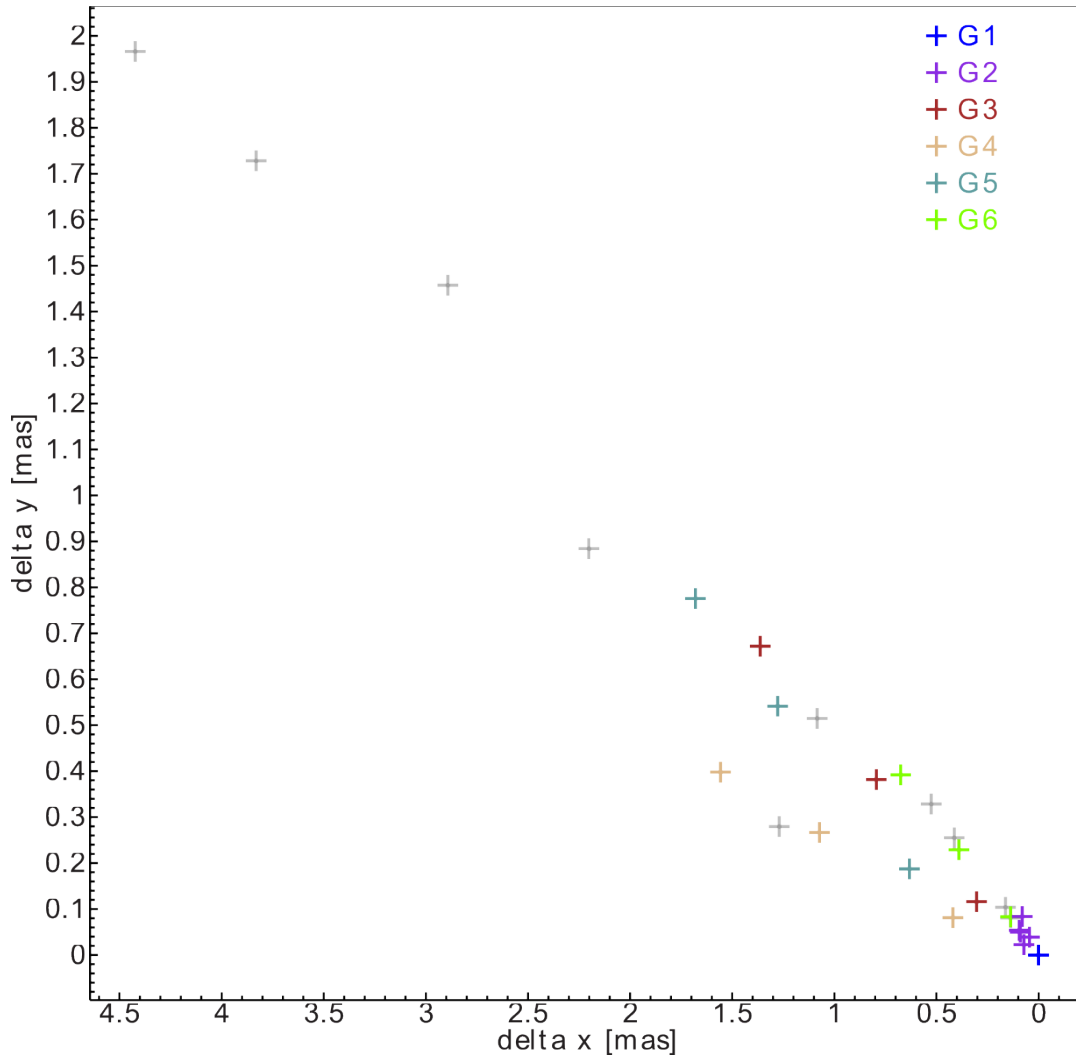
Figure 5.6.: All model-fitted 86 GHz components are plotted with relative angular distance to the core. Coloured data points indicate associated components, while no possible identification was found for gray-coloured components. The legend reveals the designation of each associated component.
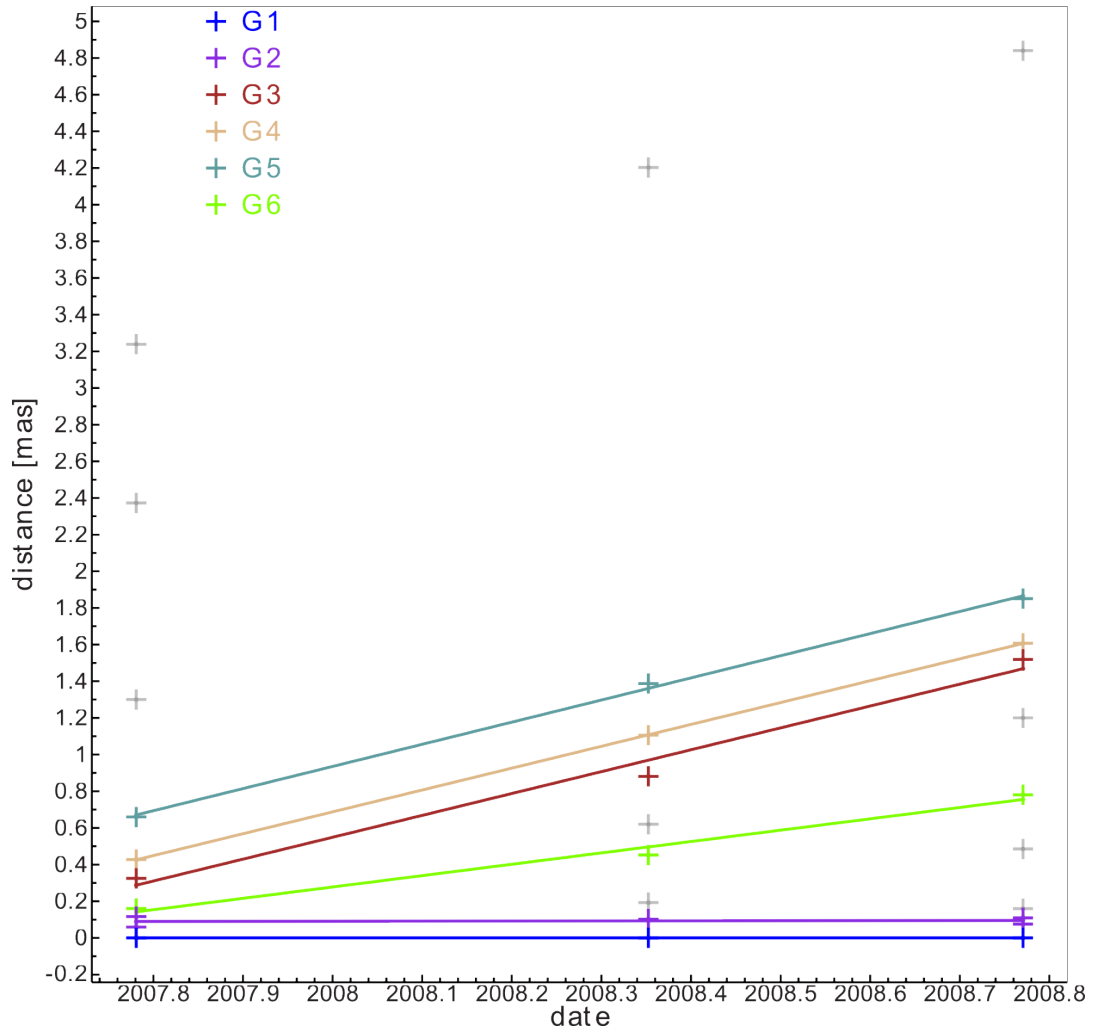
Figure 5.7.: The radial distance from the core of all 86 GHz components is plotted against the time of observation. Associated components are colour-coded as in Fig. 5.7. The continuous line represents a linear-regression fit of these components to obtain the apparent velocity and time of ejection as listed in Tab. 5.1.
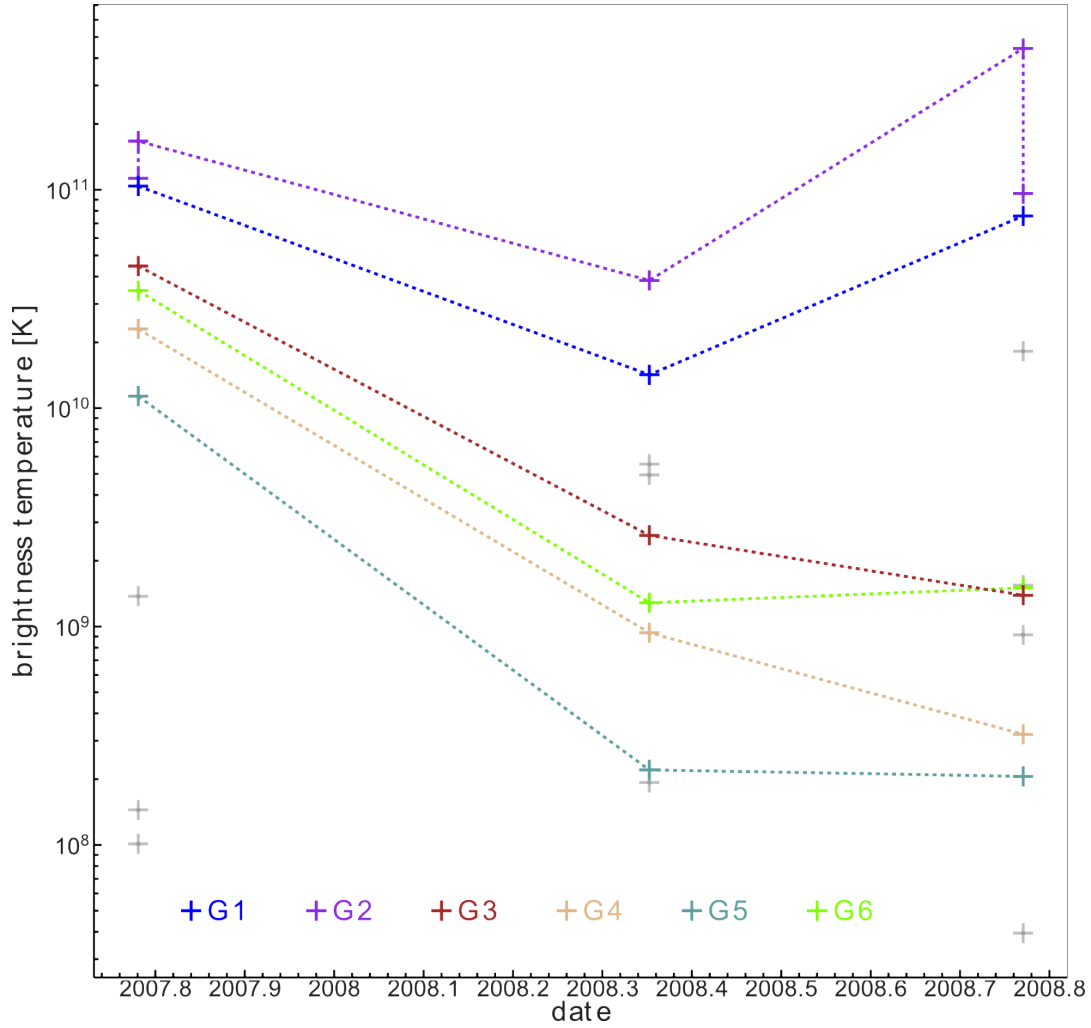
Figure 5.8.: The brightness temperature of all GMVA components is plotted on a loga-
rithmic scale against time. The dashed coloured lines are a direct connection of model-fit
components for each association

5.2.2. 43 GHz VLBA Data Only

The BG data set is in a sense naturally split in two time frames, because there are no observations available between February and May 2008. In addition, the morphology changes significantly from epoch seven (2008-01-17) to eight (2008-06-12). Therefore, the identification of components were performed separately for the first part of the data set, i.e. until Janurary 2008 and the second part, i.e. from June 2008 on (Fig. 5.9 and 5.10). Components without any association are not labelled. All components for each model-fit are summarised in Tab. A.6 through Tab. A.20, whereas Tab. 5.3 lists the linear regression fit of the associations. Similar to the analysis at 86 GHz at least three components are required for an association. Since those do not fulfil the five-component-criteria, the corresponding values for apparent speed and ejection time have to be considered as estimates. Therefore the number of individual model-fit components, which are associated is given in the last column of Tab. 5.3. As will be shown in the following discussion, the association of components from one time frame to the other is not straightforward.

Another challenge in comparing the model-fits of both parts is the varying image fidelity with the first part being of lower quality. It was tried to improve the fidelity for a few epochs exemplary by building an own CLEAN-model based on the self-calibrated data and perform one amplitude self-calibration without no average in time as well as editing of the data, if necessary. However, in these test cases, the fidelity did not improve, which is why the data was taken as provided by the Blazar Group.

The central region contains the core B1 and a stationary component B2 similar to 86 GHz. G1 is not always the brightest component, but at times (Fig. 5.13). Epoch six contains one model-fit component westwards of the core, but due its single occurrence, it was not considered further

These components are the only two connected throughout the gap in sampling. In contrast to Jorstad et al. (2005), Chatterjee et al. (2011) do not comment on the possibility of a stationary component in their analysis of the same data, which was used in this thesis.

The inner jet develops into a multi-component structure as already hinted by Subsect. 5.1.4 with most components moving radially from the core with similar position angle. However, the components, which form the bend are not moving radially from the core within the 0.5 mas. This aspect is shown in Fig. 5.11.

One feature can be traced all the way through the first part: B3. At the beginning it can be separated from B4, but both seem to merge in the end. Even though, two components were necessary until epoch six, both components are only resolvable prior to epoch three. It is therefore unclear, whether B4 is stationary. It is not trivial to assess, which component belongs to B3 in the second part, but from Fig. 5.12, 5.11, 5.9 and 5.10 it is most likely B12. However, it would require B3 to increase its apparent

velocity by roughly $0.5\,\mathrm{mas\,yr^{-1}}$. There seems to be no counterpart for B3 in the analysis by Chatterjee et al. (2011).

The bend itself seems to form in the first time frame with components B3, B7 and B8, though only three components are available for B8. B7 seems develop into the southern part of the bend. A comparison with Chatterjee et al. (2011) show component K5 to be the supposed counterpart to B7 and K6 regarding B9. The linear fit obtained for B7 does not coincide with t_0 and β_app of K5 in the first part. The picture changes after taking the second part of the BG model-fits into account. A valid assumption based on the morphological evolution of both components is the association of B7 with B11. Interestingly, B11 coincides with the ejection date from Chatterjee et al. (2011) in Tab. 5.2 of K6 as well as the apparent speed within its errors, though B10 would be the more likely candidate based solely on the model-fits. Chatterjee et al. (2011) did not consider the region described by B10 and B11 separately, but as one component from epoch eight on. As can be seen in Fig. 5.10, both features can be resolved by the intrinsic beam of the corresponding CLEAN-image (see Tab. A.5) until the last BG epoch. Chatterjee et al. (2011) used super-resolution down to a circular beam of $0.1\,\mathrm{mas}$ for their analysis, which would make it possible to resolve both components even better.

Fig. 5.12 shows, that plotting the distance over time can be misleading for B10 and B11. At this point, Fig. 5.10 and Fig. 5.11 demonstrate their strength in associating components. Here B10 and B11 are clearly separated, with B10, being the faster one ultimately catching up with B11. Whether B8 belongs to B10 or not cannot be answered using a linear fit. B8 moves slightly above $1\,\mathrm{c}$, whereas B10 moves at an apparent speed of roughly $5\,\mathrm{c}$, which would require a great deal of acceleration in-between. The average t_0 of B10 and B8 yields $t_{0,\mathrm{B12,B7}} = 2007.576 \pm 0.084$, which agrees with the given value for K6. This indicates, that B10 and B8 describe the outburst in 2007, but the component moves slower at lower distance from the core. B11 does not fit the date from Chatterjee et al. (2011) after being averaged with B7. In terms of brightness temperature, B10 succeeds B11 only until epoch eleven, where both B10 begins to overtake B11.

There are several components moving along the jet plasma between the core and the bend, which are not considered by Chatterjee et al. (2011), but part of this fit. These are B14, B17, B18 and B19. The former is one of the fastest components in the sample, but it cannot be completely traced back in terms of model-fit components. The latter three are equally interesting, because the derived ejection time of B17 agrees with B18 and B18 coincides with B19 within their errors. The estimated t_0 of all three components approximately coincide with a minor outburst (Fig. B.2), though the light-curve sampling is not precise enough to give a better estimation. B19 is the first one, which is detected of this trio, and the fastest of all associated components with an apparent velocity above $7\,\mathrm{c}$.

It is interesting to note, that the major flux density outburst did not lead to components with the fastest apparent speed, which is supported by the results of Chatterjee et al. (2011). Since the outburst lead to a complex structure, which is not seen in subsequent ejections, it is possible that interaction either with the ambient medium or within

Name	β_{app} [c]	t_0 [yr]
K4	2.24 ± 0.44	2006.61 ± 0.09
K5	2.71 ± 0.38	2007.01 ± 0.04
K6	4.18 ± 0.11	2007.66 ± 0.09
K7	4.54 ± 0.38	2008.83 ± 0.07

Table 5.2.: A list of kinematic results from tab. 10 of Chatterjee et al. (2011) relevant for comparison.

the jet itself plays a significant role. The only major flux density outburst prior to 2007, which is studied with a multi-epoch VLBI campaign, occurred in 1996. While the MO-JAVE covered the outburst at 15 GHz very well (Kadler et al. 2008), the closest 43-GHz campaign was done by Jorstad et al. (2005) and spanned three years between 1998 and 2001. Jorstad et al. (2005) were able to identify a complex feature with the outburst in 1996. Subsequent ejections of new components during their observations did not form a similar structure. Even though, minor outburst seem to occur regular, it is perhaps the magnitude of the event in 1996 and 2007, which is responsible for the complex structure, seen in Jorstad et al. (2005) and this study. However, no VLBI monitoring at mm-wavelength was done in-between these two events to test this speculation.

The feature B20 fits K7 by Chatterjee et al. (2011) in apparent speed as well as ejection time, even though only four components could be associated.

The outer jet was much more difficult to associate, because the model-fit components are relatively weak. Therefore, their position cannot be trusted as much as in case of stronger components. Nevertheless, four components have been identified (B5, B6, B15, B16). B5 and B6 move relatively slow compared to the rest of the sample, but their linear regression fit is not as good as for B15 and B16. These two components move at approximately 5 c.
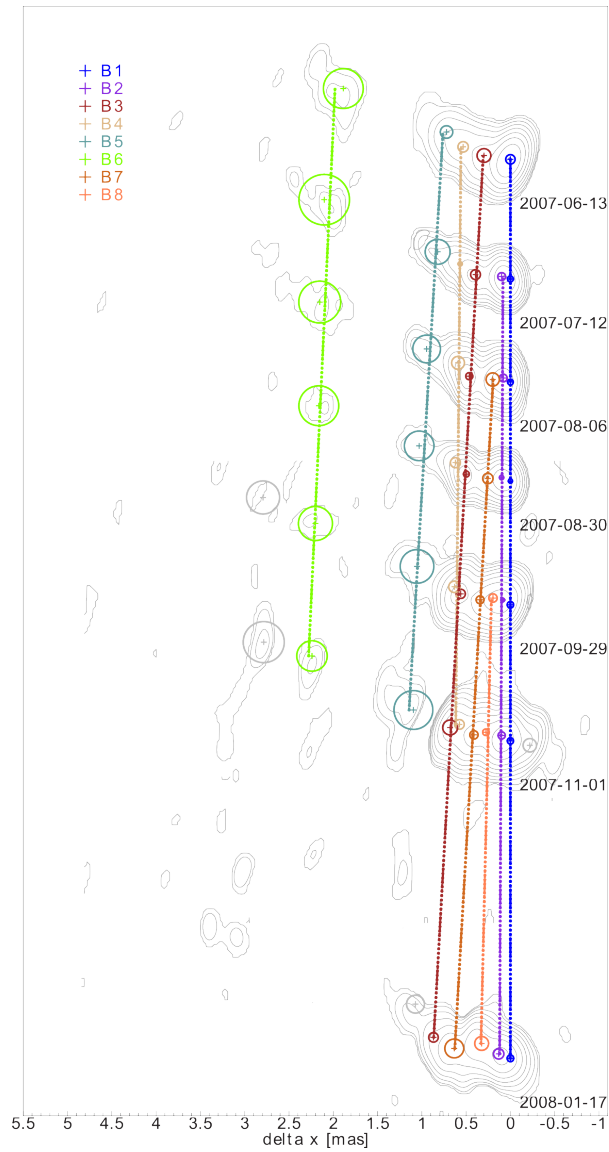
Figure 5.9.: Time evolution plot 43-GHz-VLBA from June 2007 to January 2008. Associated components are coloured and designated with a "B". Except for B1 and B2, the labels are not equivalent to those chosen for the 86-GHz GMVA components. The point of reference was set to G1 for each epoch and the horizontal scale was chosen according to Fig. 5.10. The dashed line is an interpolation of associated components. The data were obtained and calibrated by the Blazar Group (BG) at Boston University. Due to the CLEAN-image fidelity the lowest contour levels had to be set to 15σ of the rms noise to minimise noise overlapping neighbouring CLEAN-images.
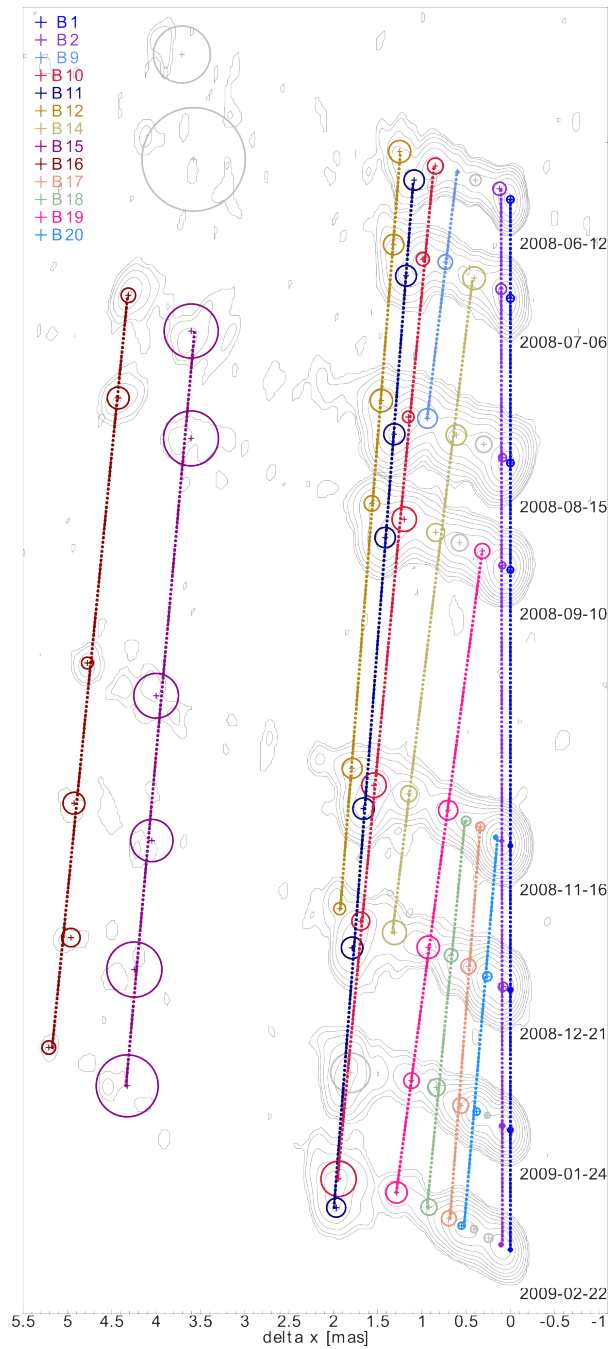
Figure 5.10.: Continuation of the time evolution plot of Fig. 5.9 for 43-GHz BG epochs after January 2008 up to February 2009. The image fidelity has improved, so it was possible to set the minimum contour level to 5σ.
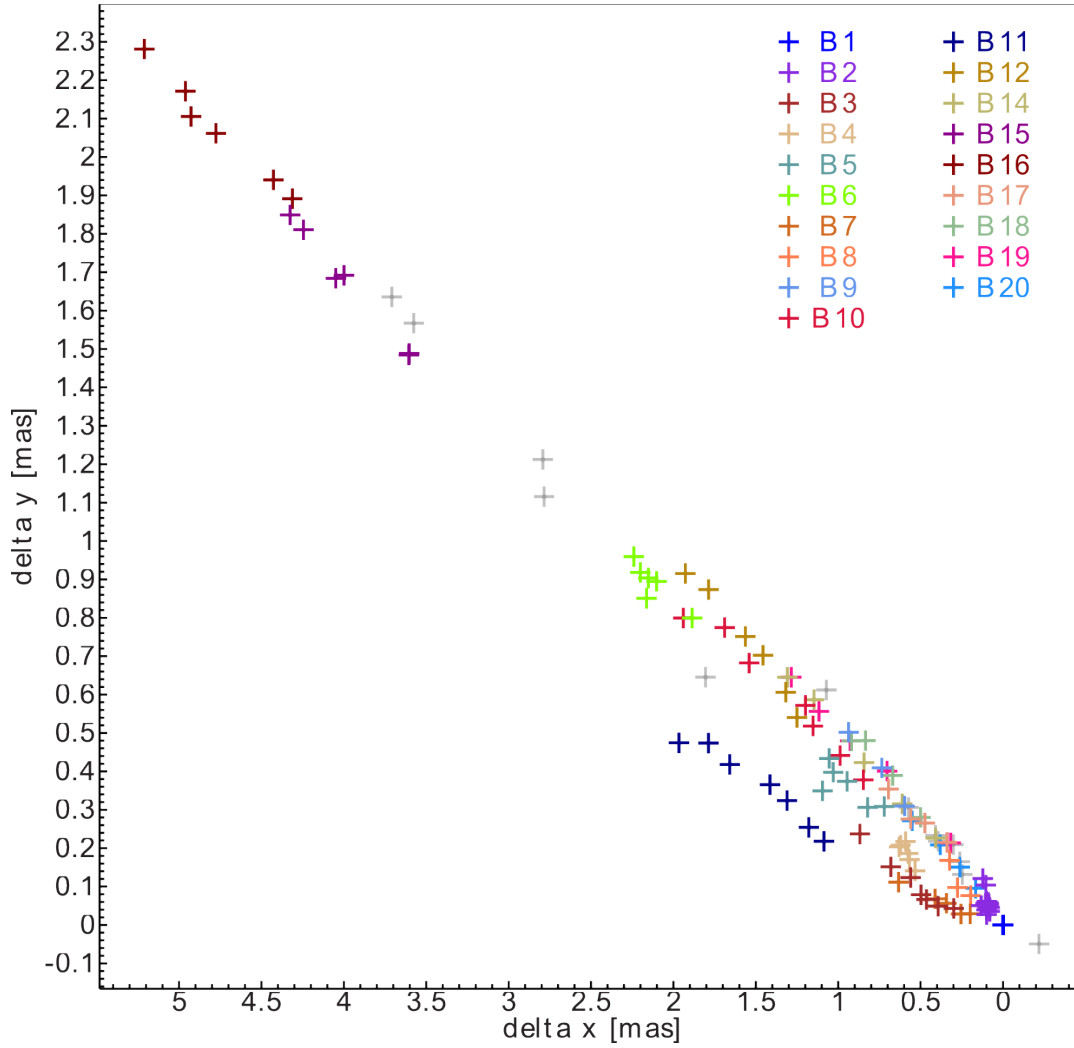
Figure 5.11.: Analogue to Fig. 5.7, all model-fitted components are plotted with relative distance from the core. Coloured components indicate associations.
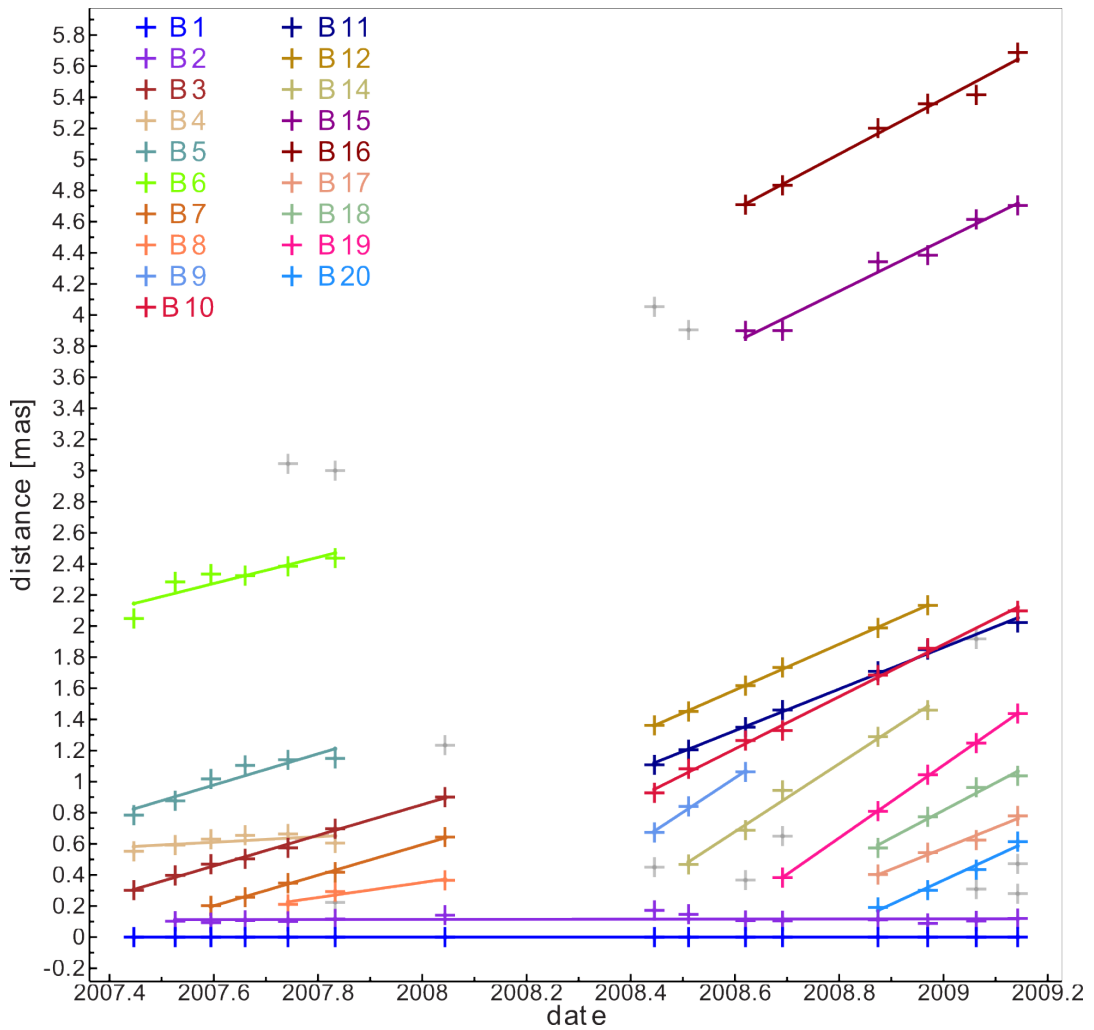
Figure 5.12.: Analogue to Fig. 5.7, all 43-GHz BG model-fits are plotted in radial distance from the core over time. Coloured components indicate associations.
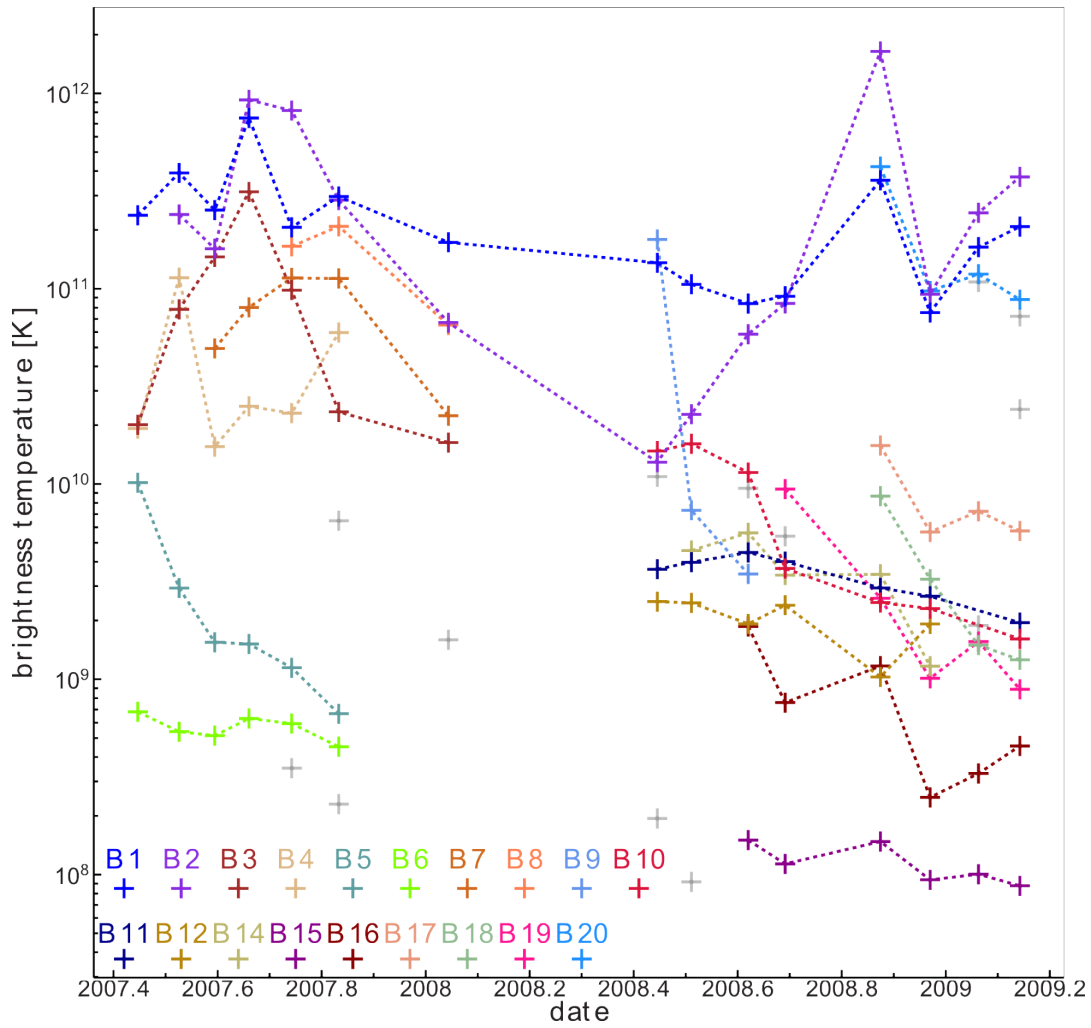
Figure 5.13.: Brightness temperature is plotted over time following Fig. 5.8 for all model-fit components at 43 GHz.

Name	$v_{\text{app,est}}$ [mas yr^{-1}]	β_{est} [c]	$t_{0,\text{est}}$ [yr]	σ_{d} [mas]	count
B2	0.003 ± 0.011	0.010 ± 0.035		0.024	14
B3	0.986 ± 0.033	3.06 ± 0.10	2007.135 ± 0.020	0.016	7
B4	0.18 ± 0.12	0.55 ± 0.36	2004.2 ± 2.3	0.037	6
B5	1.00 ± 0.18	3.11 ± 0.56	2006.63 ± 0.18	0.057	6
B6	0.84 ± 0.22	2.61 ± 0.69	2004.90 ± 0.72	0.071	6
B7	0.984 ± 0.028	3.050 ± 0.085	2007.395 ± 0.011	0.096	5
B8	0.48 ± 0.13	1.50 ± 0.40	2007.27 ± 0.17	0.029	3
B9	2.20 ± 0.14	6.84 ± 0.44	2008.136 ± 0.025	0.018	3
B10	1.679 ± 0.046	5.20 ± 0.14	2007.879 ± 0.025	0.029	7
B11	1.339 ± 0.033	4.15 ± 0.10	2007.608 ± 0.029	0.021	7
B12	1.474 ± 0.015	4.570 ± 0.047	2007.522 ± 0.012	0.069	6
B14	2.18 ± 0.13	6.77 ± 0.39	2008.289 ± 0.027	0.047	5
B15	1.65 ± 0.13	5.11 ± 0.41	2006.28 ± 0.21	0.061	6
B16	1.78 ± 0.12	5.52 ± 0.36	2005.97 ± 0.19	0.053	6
B17	1.34 ± 0.13	4.17 ± 0.41	2008.576 ± 0.045	0.027	4
B18	1.77 ± 0.19	5.49 ± 0.58	2008.540 ± 0.051	0.037	4
B19	2.336 ± 0.018	7.243 ± 0.055	2008.5269 ± 0.0034	0.0062	5
B20	1.55 ± 0.17	4.81 ± 0.53	2008.764 ± 0.029	0.034	4

Table 5.3.: Overview the kinematic results for all associated BG components analogue to Tab. 5.1. The last column indicates, how many individual components belong to each association. Results for association with less than three components have to be considered as estimates according to Lister et al. (2009).

5.3. Combining GMVA and BG Model-Fits

The combination of the GMVA and BG Model-Fits are shown in Fig. 5.14. The coloured data points resemble the BG fits with the same label as in Fig. 5.12, whereas the GMVA data is labelled black and components are distinguished by specific symbols. At this point the core at 86 GHz was aligned with the one at 43 GHz under the assumption, that a core shift does not occur. The following analysis will try to show, whether this is a valid approach. In general a core shift analysis can be done, by taking one model of each frequency from observation as close in time as possible and shift one model until optically thin features overlap. For example, this is possible for the dual-frequency monitoring program TANAMI Müller et al. (2011). However, since the 43 and 86 GHz observations are separated by about one month in average, such a procedure is not chosen here. Instead, prominent components are chosen at both frequencies. The components at 43 GHz are used as a reference point, because of the better sampling. The linear regression fit at 43 GHz is used to calculate the theoretical distance of a feature at the time of the 86-GHz observations. In a consecutive step, the obtained distance is subtracted from the distance of the component at 86 GHz, which is supposed to resemble the same feature. The resulting value is denoted $\delta_{43,86}$. The linear regression calculates the standard error of the fitted components from the fit itself ($\sigma_{\rm d}$ in Tab. 5.3) and is used to evaluate $\delta_{43,86}$.

The most prominent components at 86 GHz are those G3, G4 and G5. The best BG components for a comparison are B2, B7, B8, B10, B11 and B12. The shift is calculated for each GMVA epoch separately. Tab. 5.4 lists the components and calculated values for each epoch. Taking the average of the minor beam axis of all three 86 GHz observation as the maximal achievable resolution ($\sim$0.057 mas), only those shifts can be considered, which are resolved. It leaves only one shift-value for epoch one and three, which suggests, that the other components are in good agreement with the 43 GHz. In contrast to that, the shifts in the second epoch at 86 GHz is significant for all three components. Especially, G4 and G5 show a shift higher than all other components. Since, it was not possible to ascertain the uncertainties of these value such a comparison is difficult. In order to estimate the overall shift, the average values for each shift are calculated (Tab. 5.5, Fig. A.6). However, due to the limited statistics, the biased introduced by selecting certain components, the dominance of the shifts in the second epoch and the consistency of two of three components in the first and second epoch with the model at 43 GHz, the calculated core shift is not considered to be reliable. It is not clear, why the chosen components in the second epoch are shifted so much more.

Nevertheless, the chosen components indicate that the model at 43 and 86 GHz is consistent within the aforementioned limitations. G5 can be associated with B3 and B12, G4 with B7 and B11, G3 with B3 and B12. The acceleration, which is apparent between B3 and B12 cannot be seen at 86 GHz, because the limited number of epochs over the period of one year. Therefore, the 43-GHz-components are averaged in apparent speed and ejection time (Tab. 5.6), except for G4 the apparent velocities are consistent

with each other, while the ejection time is consistent for G3. The latter is not expected, because the light curve rises first at higher frequency, which would suggest, that the ejection of a new component should be seen first at higher frequency. From this, it seems, that G3 and G4 can be associated with the outburst in 2007.

GMVA epoch	GMVA comp	BG comp	$\delta_{43,86}$ [mas]	$\delta_{43,86}/\sigma_{d,43}$ $[\sigma_{d,43}]$
2007-10-15	G3	B7	-0.080	2.8
2007-10-15	G4	B6	-0.048	
2007-10-15	G5	B2	-0.023	
2008-05-11	G3	B12	-0.086	3.0
2008-05-11	G4	B13	-0.109	5.3
2008-05-11	G5	B14	-0.164	23
2007-10-14	G3	B12	-0.023	
2007-10-14	G4	B13	-0.052	2.5
2007-10-14	G5	B14	-0.011	

Table 5.4.: Overview components used in the core shift analysis. Column: (2) component at 86 GHz, (3) component at 43 GHz, whose linear regression fit is used, (4) $\delta_{43,86}$ denotes the relative difference between the distance from the core of the 86-GHz component the calculated 43-GHz value from the linear regression fit at the same time, (5) ratio of $\delta_{43,86}$ to the standard error of the linear regression fit σ_d

av GMVA-1 [mas]	av GMVA-2. [mas]	av GMVA-3 [mas]	av GMVA [mas]
-0.080	-0.12	-0.052	-0.084

Table 5.5.: Averaged shift from Tab. 5.4 for each GMVA epoch (column one to three) and for all epochs (last column)

Name	β_{app} [c]	t_0 [yr]
G3	3.70 $\pm$ 0.48	2007.54$\pm$0.11
av(B8,B10)	3.23 $\pm$ 0.21	2007.575$\pm$ 0.089
G4	3.696 $\pm$ 0.012	2007.4233$\pm$ 0.0031
av(B7,B11)	3.600 $\pm$ 0.067	2007.502$\pm$ 0.016
G5	3.74 $\pm$ 0.14	2007.225$\pm$ 0.044
av(B3,B12)	3.815 $\pm$ 0.055	2007.329 $\pm$ 0.012

Table 5.6.: Summary of association between components at 43 and 86 GHz with the 43 GHz components averaged in apparent velocity and ejection time for better comparison
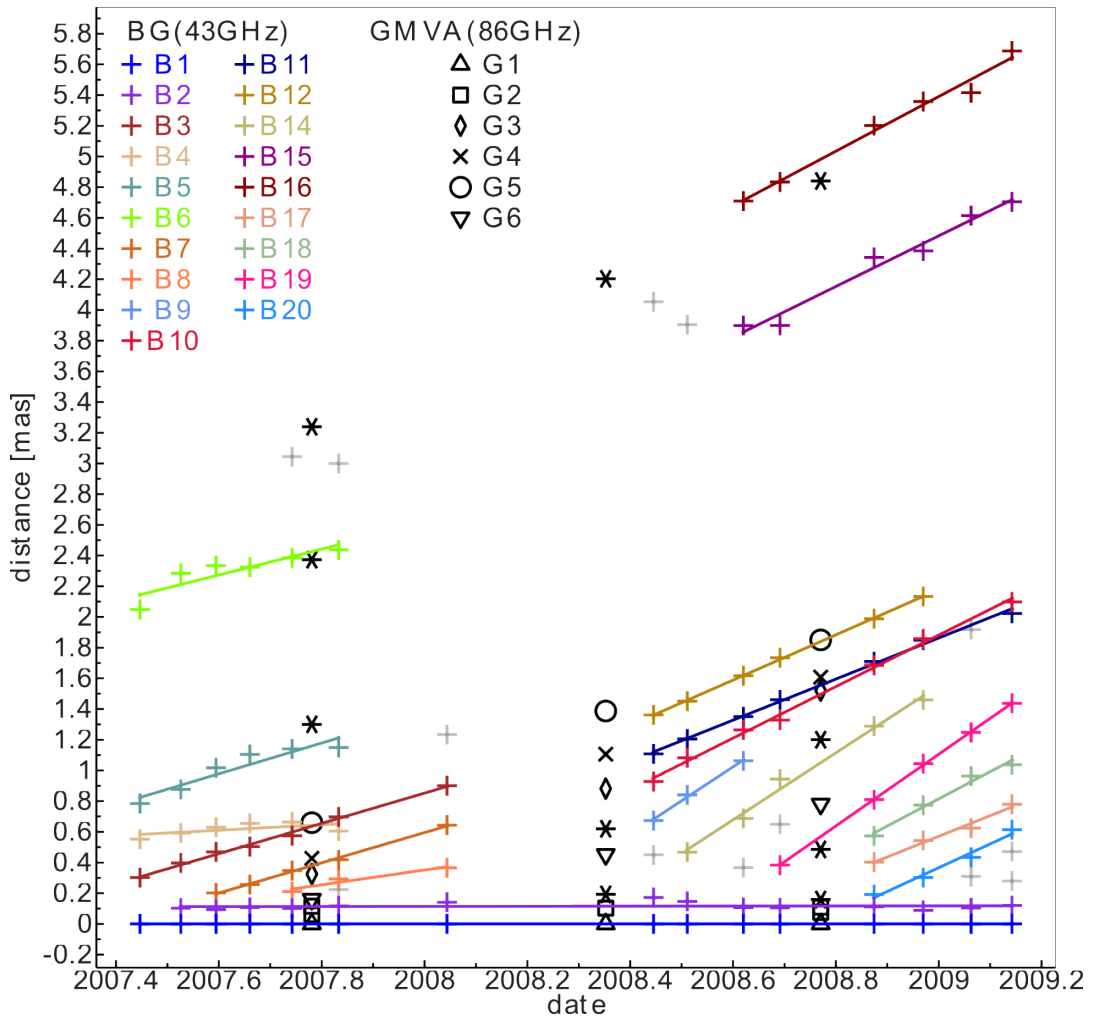
Figure 5.14.: 43 and 86 GHz components are plotted with radial distance from the core over time

5.4. Jet Precession and Collimation

The final section discusses jet collimation and precession at 43 and 86 GHz. To this purpose, the position angle of each component is plotted over time. The line between two data points is neither a fit nor an interpolation, but a straight connection.

The distribution of the components at 43 GHz and 86 GHz are shown in Fig. 5.15 and Fig. 5.16, respectively. The former plot neglects one model-fit component of epoch five at 43 GHz, which is located westwards from the core. Because it is the only one of its kind, it is not considered further. A plot including this component can be found in Fig. A.5 of Appendix A.

The stationary 43-GHz component B2 undergoes the most pronounced changes varying between $\sim 75°$ and $\sim 45°$. Since B1 (the core) and B2 exhibit a great deal of variability over the observed time range, the change in position angle is probably connected to the activity. However, a direct correlation such that a change in brightness temperature or flux is directly reflected by change in position angle cannot be concluded from the inspection of Fig. 5.15 and Fig. 5.13 (Fig. A.4). A more detailed correlation analysis would give a better answer. G2 is the stationary component at 86 GHz increases its position angle by $\sim 15°$, taking the average of each of the two association for G2 in epoch one and three. As there are no 43-GHz data available roughly at the same time of the GMVA observation a direct comparison is not possible.

At 86 GHz the bend is made of components G3, G4 and G5, whereas at 43 GHz it comprises of B3, B7 and B8 up to January 2008 and B10,B11 and B12 afterwards (Fig. 5.5, Fig. 5.9, Fig. 5.10). In Subsect. 5.2.2 B7 was associated with B11 as the component at the southern part of the bend. The minor changes in the position angle of both components support this conclusion. G4 being the 86-GHz version of B7 and B11 remains roughly constant as well. For B3 and B12 the change in position angle is more pronounced (of the order of 10°). Since the kinematic analysis suggests that acceleration occurs for B3 to become B12 the change in position angle may be related to it. The position angle of the corresponding 86-GHz component G5 decreases as well.

All in all, the majority of components at 43 GHz is distributed between 60° and 70° with most prominent exceptions being the stationary component B2 and the components B7 and B11 of the bend, which are associated with the outburst in 2007. Hence, the data does not indicate continuous precession of the jet in the form of helical motion as discussed in Subsect. 3.2.1 is not. Instead the jet seems to be well collimated. Following the model (Fig. 3.3) of the structure and emission of a quasar by Marscher (2009) this would put the mm-jet of 3C111 in the area of roughly 10^6 Schwarzschild radii. It of course a very simplified conclusion. A detailed core shift analysis as it was performed for example by Hada et al. (2011) for M87 would make it possible to put tighter constrain on the distance between the radio jet and its origin.
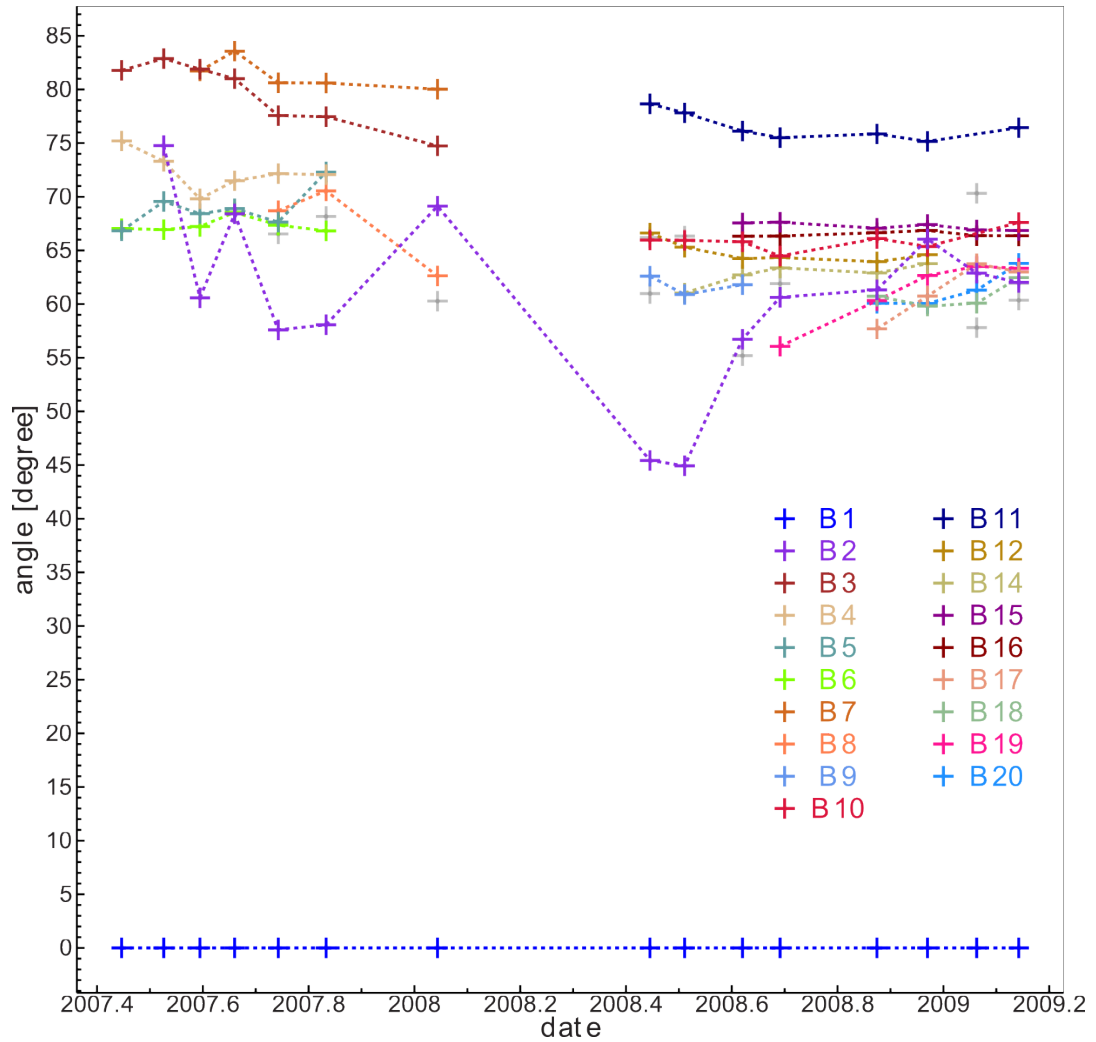
Figure 5.15.: The position angle with respect to the core are plotted over time for all BG modelfits. One model-fit of epoch 6 at 43 GHz is left out, because it extends westwards from the core leading to large negative angle. It is the only one of its kind and is thus neglected. A plot including this component is shown in Fig. A.5
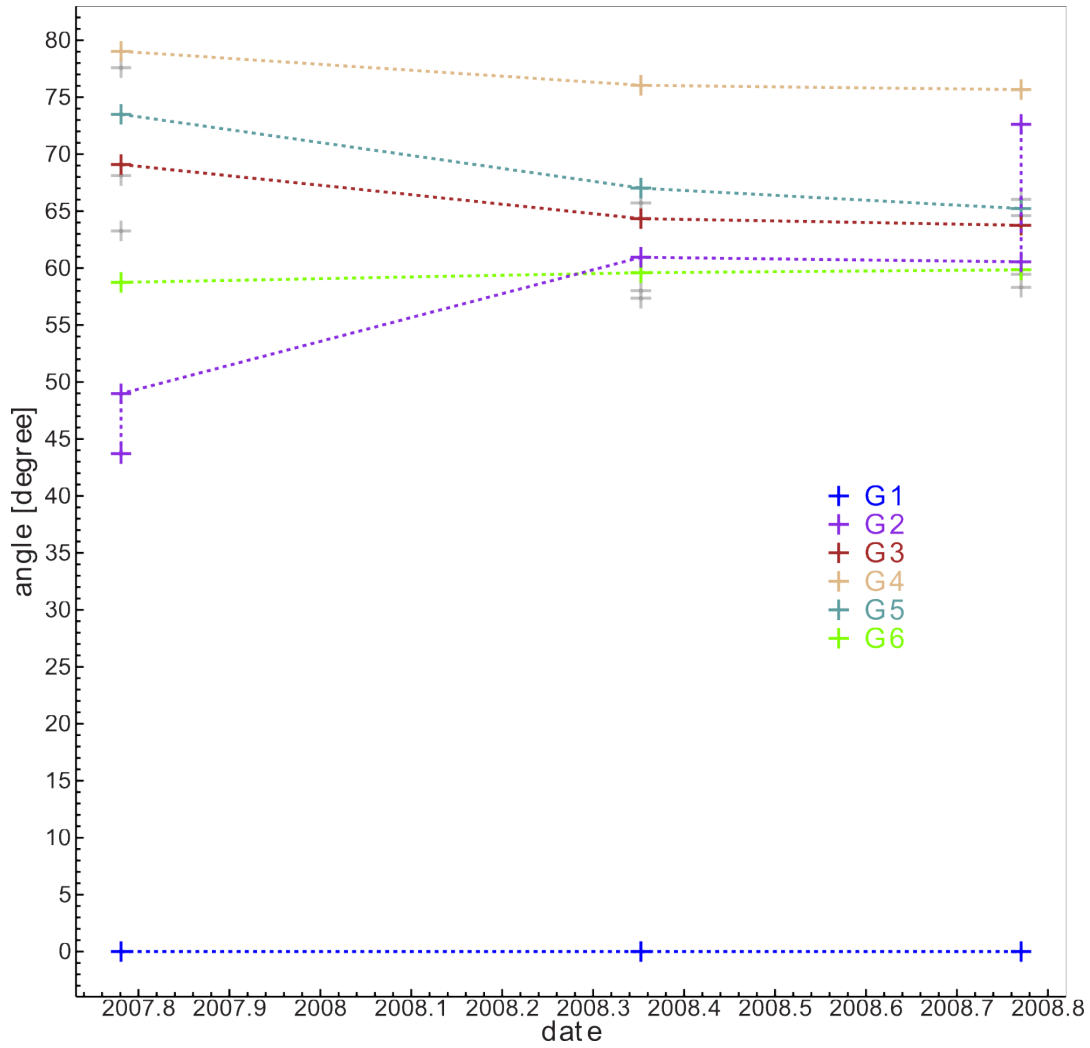
Figure 5.16.: Position angle of the model-fit components st 86 GHz is plotted over time

6. Summary and Outlook

Three high-resolution VLBI observations in October 2007, May and October 2008 of the broad-line radio galaxy 3C111 at 86 GHz with the Global mm-VLBI Array (GMVA) were conducted after a major flux density outburst. A one-sided jet is resolved down to 50 mpc (projected onto the plane of the sky) into several distinct optically thin features with unprecedented fidelity. A self-consistent multi-frequency, multi-epoch model of the jet with circular Gaussian components was constructed using additional 15 epochs of 43 GHz VLBA data between June 2007 and February 2009. Although a large gap in the sampling the 43 GHz required components before and after the gap to be treated separately first and associated afterwards, it also revealed ongoing acceleration along the jet, which has been reported before (Jorstad et al. 2005, Kadler et al. (2008)).

The outburst in 2007 resulted in the ejection of matter into the jet stream, which formed a complex structure shaping the jet prominently. At both frequencies this structure was decomposed into distinctly traceable components and acceleration was most notably observed for these components. The complex nature of this feature and the fact, that subsequent ejections move at even faster apparent velocities without forming such a feature suggests strong interaction within the jet or the ambient medium in this case. The components of the bend travel with an apparent velocity up to 5c, though a stationary component close to the core as well as one component moving as fast as 7c are contained within the sample. The only prior mentioning of such a complex structure was associated with a flux density outburst in 1996 Jorstad et al. (2005)

A quantitative analysis of acceleration was not possible for this thesis, but should be attempted. However, a fit solely based on the radial distance travelled over time, may not account for the apparent non-radial motion of the southern component of the bend close to the core. Although the position angle of components at 43 and 86 GHz varies between 50° and 80°, the majority is located between 60° and 70° undergoing only minor changes. The components with highest and lowest position angles are associated with the bend and stationary component, respectively. Therefore, continuous jet precession is not suggested by the data. Except for the bend after the major outburst, the jet is very well collimated in the same direction as shown on images by the MOJAVE monitoring program at 15 GHz.

3C111 is an excellent object to study the evolution of a radio jet with mm-VLBI. To this purpose a proposal for a densely sampled 86 GHz VLBI campaign with the GMVA and VLBA combined with the 100m Effelsberg telescope has been submitted (PI: R. Schulz). In combination with continuous monitoring at 43 GHz with the VLBA (PI: A. Marscher), this would create a sophisticated mutli-frequency data base.

Such data could be used to study a possible shift of the self-absorbed part of the jet between the two frequencies. The sampling of the data at 43 and 86 GHz for this thesis prevented a conclusive result on this subject. Because 3C111 can be well resolved even at higher radio frequencies, VLBI observations at three to four frequencies may constrain the core shift dependency of 3C111 on the frequency as was performed for M87 by Hada et al. (2011). Since 3C111 is considerably further away, VLBI observations above 86 GHz should be used, which are currently only possible for strong radio-loud quasars. However, calibration and sensitivity of mm-VLBI are continuously developed.

A counter-jet has not been detected in the GMVA data. Instead, the most westward component at 43 and 86 GHz was defined as the core and first component eastwards was identified as a stationary component. These are the brightest components within the jet. The low viewing angle of 18° (Jorstad et al. 2005) to the line of sight, probably causes the emission from the counter-jet to be highly de-boosted, preventing currently any means of detection.

The study of 3C111 is also a study of the connection between blazars and radio galaxies in general. The aforementioned low viewing angle and the blazar-like spectral energy distribution (Hartman et al. 2008) allows to draw conclusions for both types of AGN by observing 3C111 across the electromagnetic spectrum.

A. Additional Images and Tables
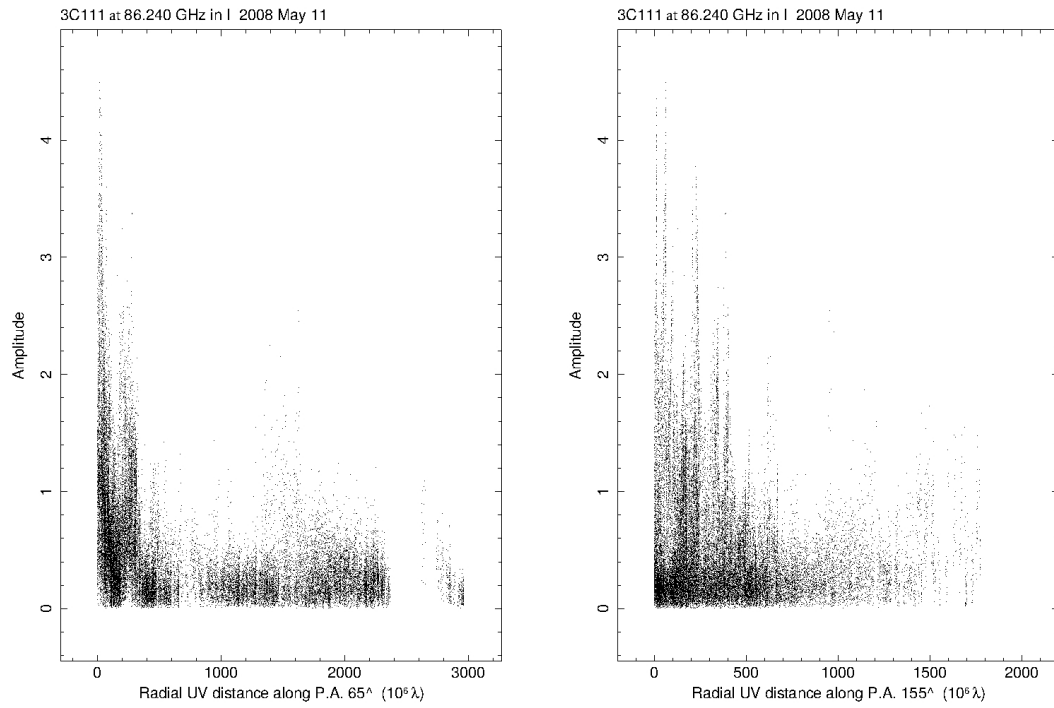
Figure A.1.: Visibilities of the 2nd GMVA epoch at angles of 65° and 155° in the (u, v)-plane before first amplitude self-calibration
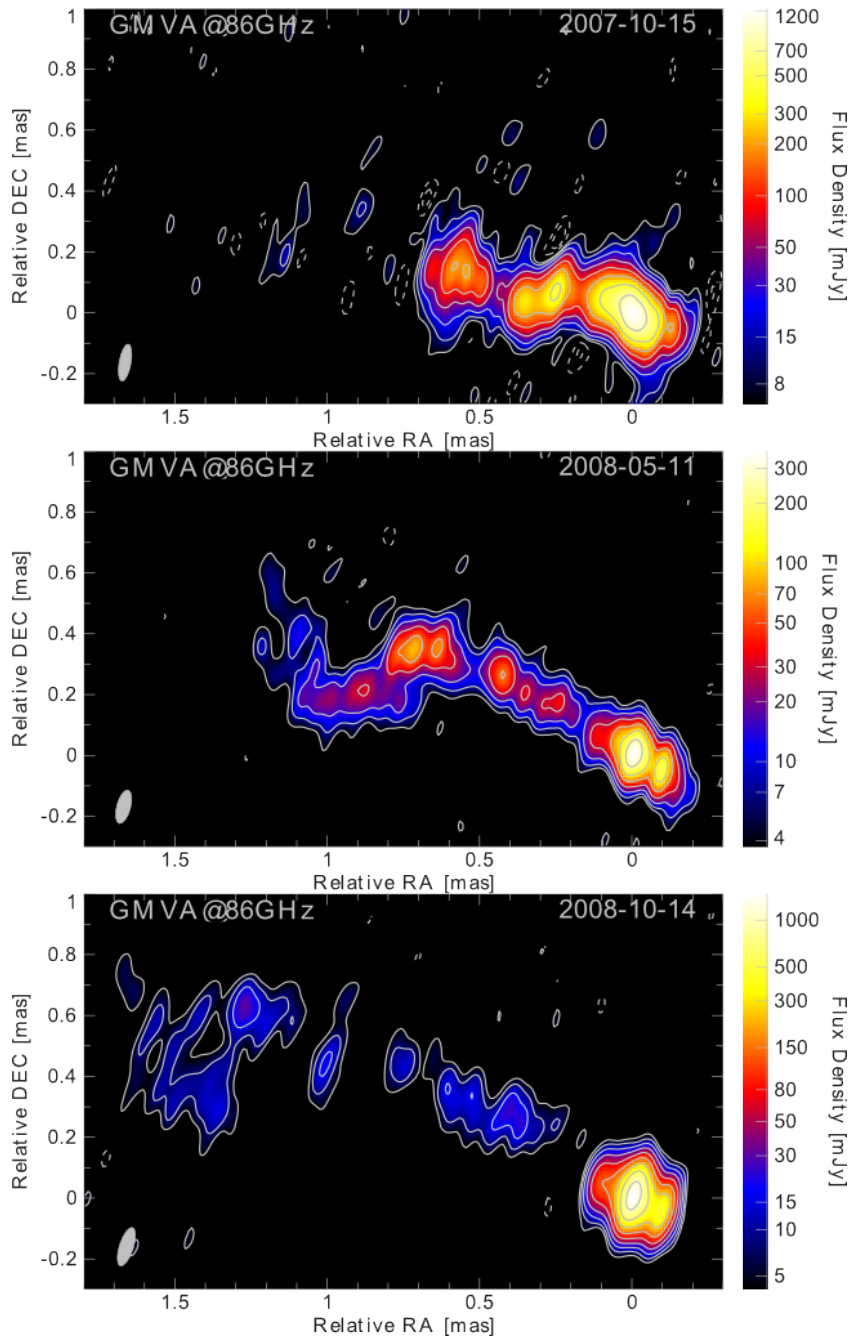
Figure A.2.: The same setting as in Fig. 5.3, except that all three images were obtained with uniform weighting. The decrease in sensitivity due to uniform weighting is visible, but the increase in resolution shows even finer sub-structure. All three images are convoluted with their intrinsic beam, i.e. $(0.12\text{x}0.038)$ mas (top), $(0.011\text{x}0.045)$ mas (middle), $(0.13\text{x}0.046)$ mas(bottom). A list of the relevant image parameters is given in Tab. A.1.
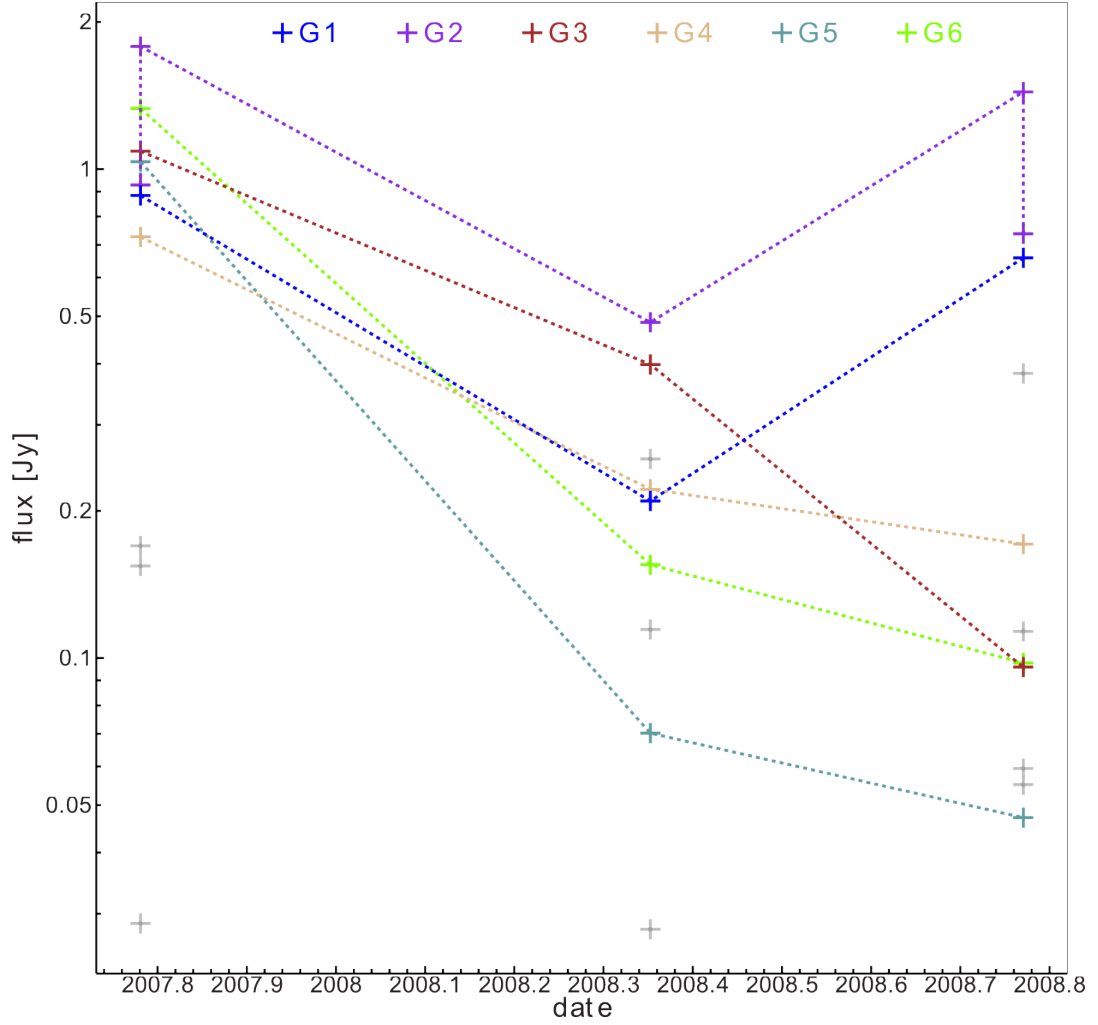
Figure A.3.: The flux density of all 86-GHz GMVA components is plotted on a logarithmic scale against their time of observation. The dashed line is simply a direct connection of data point and not a fit.
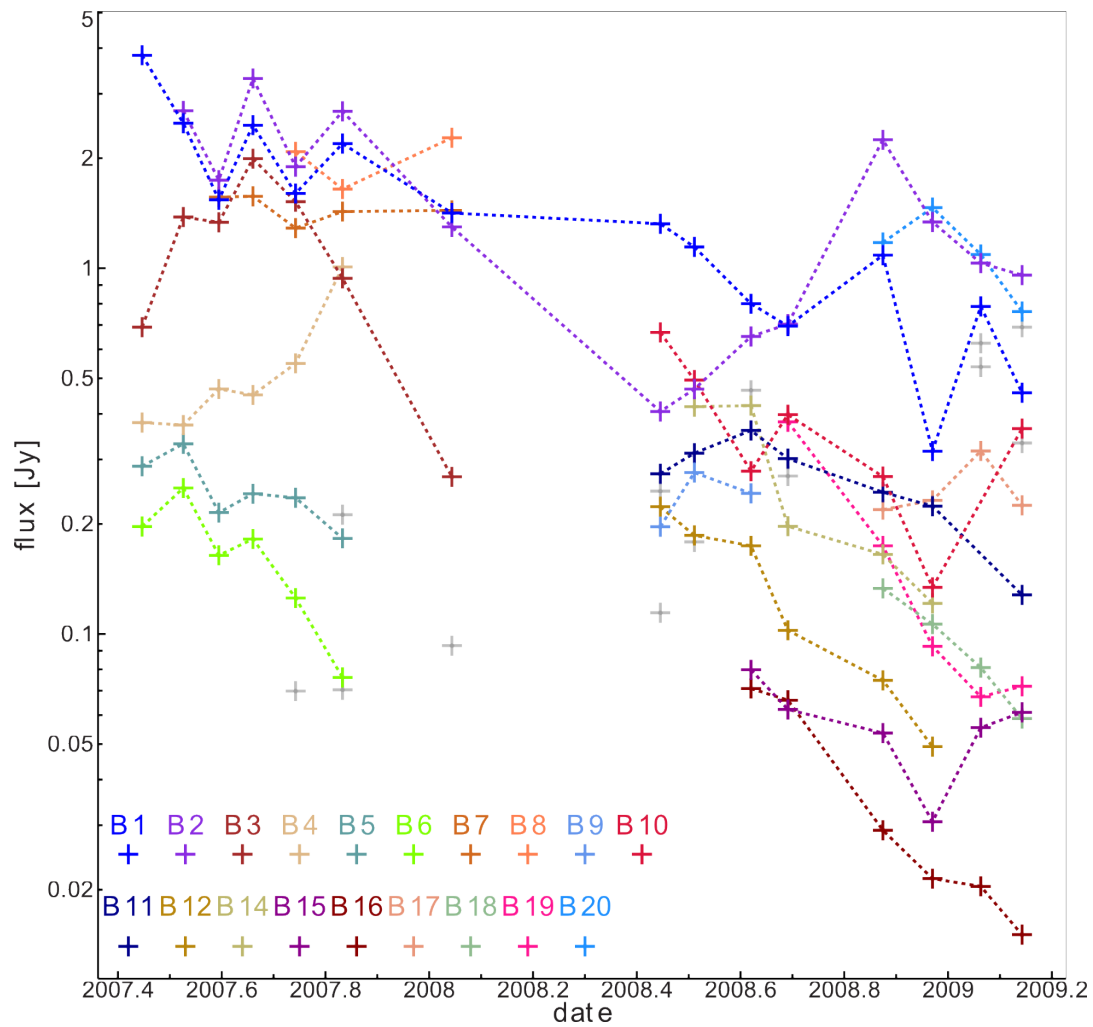
Figure A.4.: Flux over time of observation of all 43-GHz components is plotted over time analogue to Fig. A.3.
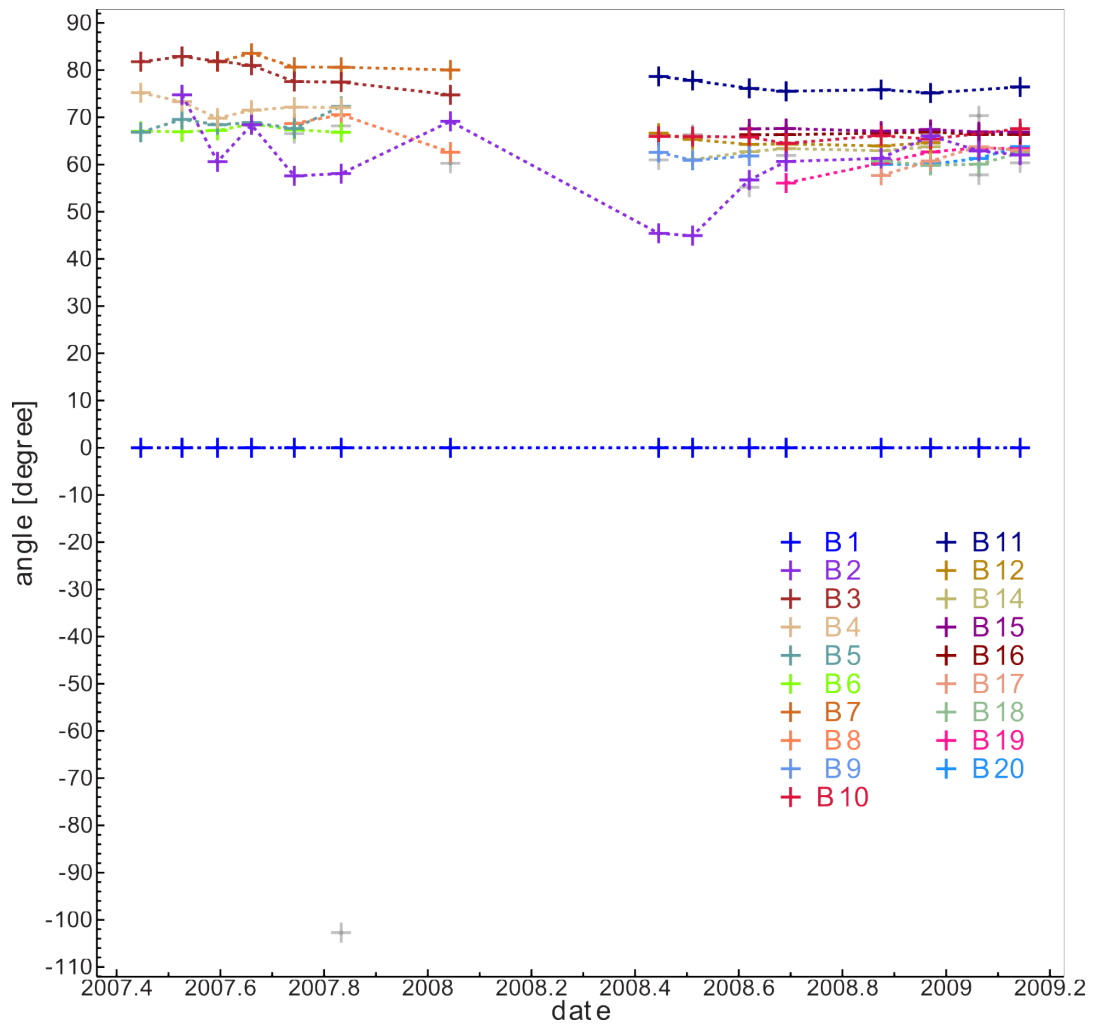
Figure A.5.: 43-GHz components are plotted with their position angle over time.
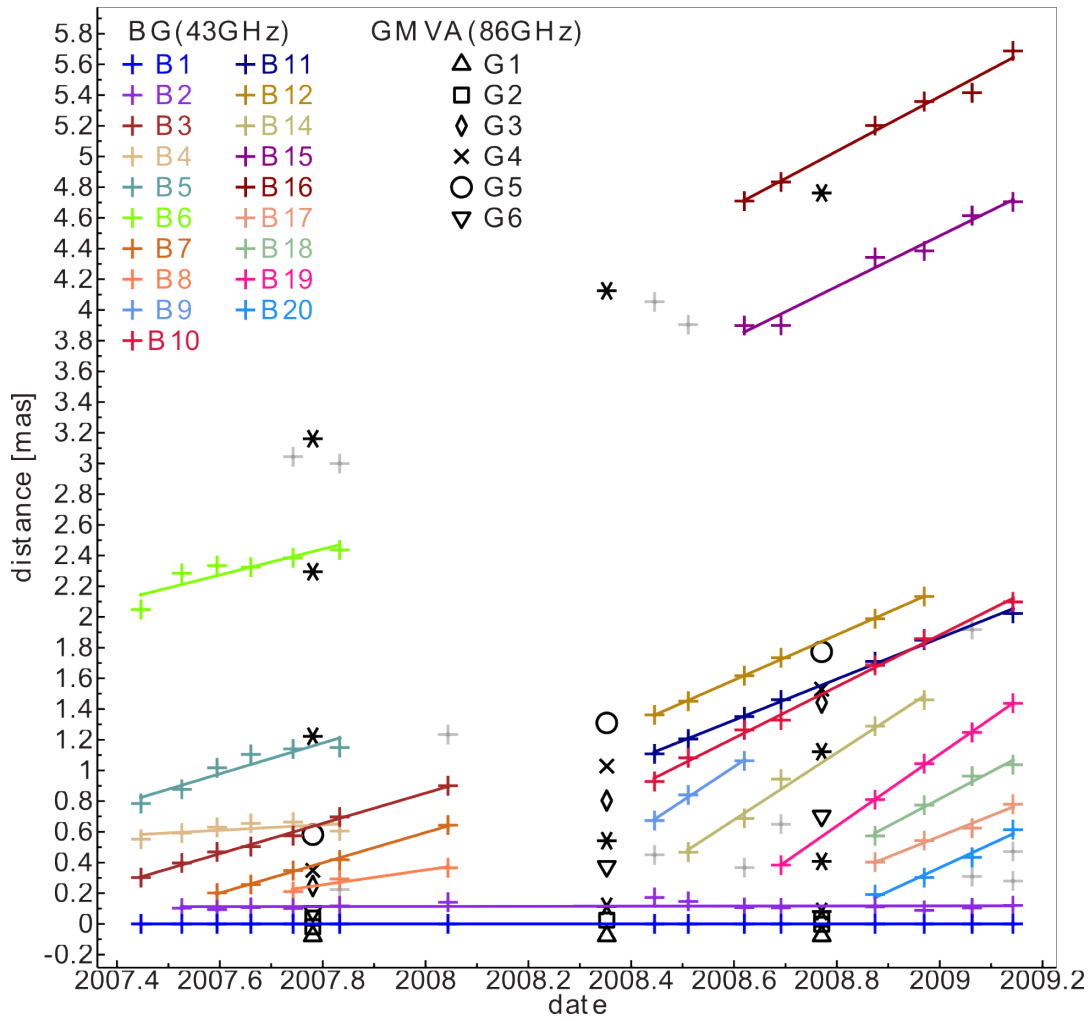
Figure A.6.: Radial distance over time of all 43 and 86-GHz components, with the latter shifted by the average core shift

Epoch yyyy-mm-dd	weighting	RMS [mJy beam^{-1}]	$S_{\rm peak}$ [Jy beam^{-1}]	$S_{\rm total}$ [Jy]	$S_{86,\rm SD}$ [Jy]	$b_{\rm maj}$ [mas]	$b_{\rm min}$ [mas]	PA [°]	σ
2007-10-15	natural	0.76	1.50	8.10	12.06 ± 0.22	0.15	0.045	-10.8	0.97
	uniform	1.16	1.24	8.05	12.06 ± 0.22	0.12	0.038	-10.1	1.04
2008-05-11	natural	0.73	0.39	1.90	4.06 ± 0.16	0.15	0.059	-15.5	0.87
	uniform	1.41	0.368	1.88	4.06 ± 0.16	0.11	0.045	-15.0	0.87
2007-10-14	natural	1.07	1.87	3.78	4.06 ± 0.21	0.17	0.067	-18.2	0.77
	uniform	1.70	1.48	3.59	4.06 ± 0.21	0.13	0.046	-17.8	0.78

Table A.1.: Image Parameters of all three GMVA observations at 86 GHz with uniform and natural weighting, the RMS is taken from DIFMAP , $\sigma = \sqrt{\chi^2_{\rm red}}$ after the last phase self-calibration, The single dish flux density is taken from data of the F-GAMMA monitoring program

Flux density Jy	Distance [mas]	P.A. [°]	b_{maj} [mas]	T_{b} [K]	Name
0.88	0.000	0.0	0.039	1.0e+11	G1
1.78	0.059	49.0	0.043	1.7e+11	G2
0.93	0.116	43.7	0.038	1.1e+11	G2
1.33	0.160	58.7	0.082	3.5e+10	G6
1.09	0.325	69.1	0.065	4.5e+10	G3
0.73	0.427	79.0	0.074	2.3e+10	G4
1.04	0.660	73.5	0.127	1.1e+10	G5
0.17	1.300	77.6	0.454	1.4e+08	
0.04	2.373	68.1	0.060	1.4e+09	
0.15	3.239	63.3	0.518	1.0e+08	

Table A.2.: A list of parameters of all model-fit components used in the first 86-GHz GMVA epoch (2007-10-15), i.e. flux density in Jy, the radial distance from the core in mas, the position angle in degrees with respect to the core, the brightness temperature of the model-fit component in Kelvin and if available the designation of its association. The quality of the fit is given by $\chi^2_{\mathrm{red}} = 2.0$

Flux density Jy	Distance [mas]	P.A. [°]	b_{maj} [mas]	T_{b} [K]	Name
0.21	0.00	0.0	0.051	1.4e+10	G1
0.49	0.103	60.9	0.057	3.8e+10	G2
0.26	0.193	57.4	0.095	4.9e+09	
0.16	0.452	59.6	0.146	1.3e+09	G6
0.11	0.620	58.0	0.060	5.5e+09	
0.40	0.881	64.3	0.164	2.6e+09	G3
0.22	1.106	76.0	0.204	9.4e+08	G4
0.07	1.387	67.0	0.237	2.2e+08	G5
0.03	4.203	65.7	0.159	1.9e+08	

Table A.3.: List of parameters for all model-fit components of the 2nd 86-GHz GMVA epoch (2008-05-11, see caption of Tab. A.2),$\chi^2_{\mathrm{red}} = 0.81$

Flux density Jy	Distance [mas]	P.A. [°]	b_{maj} [mas]	T_{b} [K]	Name
0.66	0.00000	0.0	0.039	7.6e+10	G1
0.74	0.075	72.6	0.037	9.6e+10	G2
1.44	0.109	60.6	0.024	4.4e+11	G2
0.38	0.159	59.5	0.061	1.8e+10	
0.11	0.485	58.3	0.148	9.2e+08	
0.10	0.781	59.8	0.107	1.5e+09	G6
0.06	1.200	64.6	0.082	1.5e+09	
0.10	1.520	63.8	0.110	1.4e+09	G3
0.17	1.608	75.7	0.306	3.2e+08	G4
0.05	1.851	65.2	0.201	2.1e+08	G5
0.06	4.840	66.0	0.496	3.9e+07	

Table A.4.: List of parameters for all model-fit components of the 3rd 86-GHz GMVA epoch (2008-10-14, see caption of Tab. A.2),$\chi^2_{\mathrm{red}} = 0.63$

Epoch yyyy-mm-dd	rms [mJy beam^{-1}]	S_{peak} [Jy beam^{-1}]	S_{total} [Jy]	b_{maj} [mas]	b_{min} [mas]	PA [°]	σ
2007-06-13	0.83	3.28	5.58	0.37	0.20	-22.4	3.15
2007-07-12	0.93	3.82	7.40	0.28	0.16	4.2	2.86
2007-08-06	0.77	2.68	7.05	0.30	0.15	-4.5	1.71
2007-08-30	1.32	4.29	10.16	0.27	0.16	-5.04	1.43
2007-09-29	1.17	3.36	9.45	0.36	0.18	-24.5	2.16
2007-11-01	0.60	3.67	9.83	0.36	0.17	-20.1	4.61
2008-01-17	0.80	2.01	6.91	0.31	0.18	-3.7	3.21
2008-06-12	1.58	1.19	3.52	0.31	0.15	-4.2	1.46
2008-07-06	1.70	1.10	3.43	0.35	0.15	-3.2	1.24
2008-08-15	0.61	1.07	3.51	0.37	0.18	-21.4	1.90
2008-09-10	0.77	1.06	3.17	0.31	0.18	-15.0	1.36
2008-11-16	0.68	3.32	5.91	0.30	0.18	-7.6	1.33
2008-12-21	1.01	1.38	4.17	0.33	0.18	-6.2	0.95
2009-01-24	0.95	1.38	4.65	0.28	0.16	-2.1	0.80
2009-02-22	0.99	1.13	4.18	0.29	0.17	2.2	0.824

Table A.5.: Image Parameters of all uniformly weighted 43 GHz data from the Blazar Group used in this thesis. RMS is determined by DIFMAP and $\sigma = \sqrt{\chi^2_{\text{red}}} =$ is given after a single phase self-calibration of the CLEAN-model provided by the Blazar Group

Flux density Jy	Distance [mas]	P.A. [°]	b_{maj} [mas]	T_{b} [K]	Name
3.83	0.00	0.0	0.11	2.4e+11	B1
0.69	0.30	81.8	0.16	2.0e+10	B3
0.38	0.55	75.2	0.12	1.9e+10	B4
0.29	0.78	66.8	0.14	1.0e+10	B5
0.20	2.05	67.0	0.45	6.8e+08	B6

Table A.6.: List of parameters for all model-fit components of the 1st 43-GHz BG epoch (2007-06-13, see caption of Tab. A.2), $\chi^2_{\text{red}} = 14$

Flux density Jy	Distance [mas]	P.A. [°]	b_{maj} [mas]	T_{b} [K]	Name
2.49	0.00	0.0	0.07	3.9e+11	B1
2.70	0.10	74.8	0.09	2.4e+11	B2
1.38	0.40	82.9	0.11	7.8e+10	B3
0.37	0.59	73.3	0.05	1.1e+11	B4
0.33	0.88	69.6	0.28	2.9e+09	B5
0.25	2.28	66.9	0.57	5.4e+08	B6

Table A.7.: List of parameters for all model-fit components of the 1st 43-GHz BG epoch (2007-07-12, see caption of Tab. A.2), $\chi^2_{\mathrm{red}} = 9.9$

Flux density Jy	Distance [mas]	P.A. [°]	b_{maj} [mas]	T_{b} [K]	Name
1.54	0.00	0.0	0.07	2.5e+11	B1
1.74	0.09	60.6	0.09	1.6e+11	B2
1.57	0.20	81.7	0.15	4.9e+10	B7
1.34	0.47	81.9	0.08	1.5e+11	B3
0.47	0.63	69.8	0.15	1.6e+10	B4
0.21	1.02	68.4	0.31	1.5e+09	B5
0.16	2.33	67.2	0.47	5.1e+08	B6

Table A.8.: List of parameters for all model-fit components of the 3rd 43-GHz BG epoch (2007-08-06, see caption of Tab. A.2), $\chi^2_{\mathrm{red}} = 4.4$

Flux density Jy	Distance [mas]	P.A. [°]	b_{maj} [mas]	T_{b} [K]	Name
2.46	0.00	0.0	0.05	7.5e+11	B1
3.30	0.11	68.4	0.05	9.3e+11	B2
1.57	0.26	83.6	0.11	8.0e+10	B7
1.99	0.50	81.0	0.07	3.1e+11	B3
0.45	0.67	71.5	0.11	2.5e+10	B4
0.24	1.10	68.9	0.33	1.5e+09	B5
0.18	2.32	68.5	0.45	6.3e+08	B6

Table A.9.: List of parameters for all model-fit components of the 4th 43-GHz BG epoch (2007-08-30, see caption of Tab. A.2), $\chi^2_{\mathrm{red}} = 4.5$

Flux density Jy	Distance [mas]	P.A. [°]	b_{maj} [mas]	T_{b} [K]	Name
1.60	0.00	0.0	0.07	2.1e+11	B1
1.70	0.10	57.6	0.04	8.2e+11	B2
2.08	0.21	68.7	0.09	1.6e+11	B8
1.29	0.35	80.6	0.09	1.1e+11	B7
1.52	0.57	77.6	0.10	9.8e+10	B3
0.55	0.66	72.2	0.13	2.3e+10	B4
0.24	1.14	67.6	0.38	1.1e+09	B5
0.13	2.38	67.4	0.38	5.9e+08	B6
0.07	3.04	66.5	0.37	3.5e+08	

Table A.10.: List of parameters for all model-fit components of the 5th 43-GHz BG epoch (2007-09-29, see caption of Tab. A.2), , $\chi^2_{\mathrm{red}} = 4.9$

Flux density Jy	Distance [mas]	P.A. [°]	b_{maj} [mas]	T_{b} [K]	Name
0.21	0.22	-102.7	0.15	6.5e+09	
2.19	0.00	0.0	0.07	3.0e+11	B1
2.69	0.12	58.1	0.08	2.8e+11	B2
1.65	0.29	70.5	0.07	2.1e+11	B8
1.43	0.42	80.6	0.09	1.1e+11	B7
1.01	0.60	72.1	0.11	6.0e+10	B4
0.94	0.70	77.5	0.17	2.3e+10	B3
0.18	1.15	72.3	0.44	6.7e+08	B5
0.08	2.44	66.8	0.34	4.5e+08	B6
0.07	3.00	68.2	0.46	2.3e+08	

Table A.11.: List of parameters for all model-fit components of the 6th 43-GHz BG epoch (2007-11-01, see caption of Tab. A.2), , $\chi^2_{\mathrm{red}} = 9.8$

Flux density Jy	Distance [mas]	P.A. [°]	b_{maj} [mas]	T_{b} [K]	Name
1.42	0.00	0.0	0.08	1.7e+11	B1
1.30	0.14	69.1	0.12	6.7e+10	B2
2.27	0.37	62.6	0.16	6.5e+10	B8
1.44	0.64	80.0	0.21	2.2e+10	B7
0.27	0.90	74.7	0.11	1.6e+10	B3
0.09	1.23	60.3	0.20	1.6e+09	

Table A.12.: List of parameters for all model-fit components of the 7th 43-GHz BG epoch (2008-01-17, see caption of Tab. A.2), $\chi^2_{\mathrm{red}} = 16$

Flux density Jy	Distance [mas]	P.A. [°]	b_{maj} [mas]	T_{b} [K]	Name
1.32	0.00	0.0	0.08	1.4e+11	B1
0.41	0.17	45.4	0.15	1.3e+10	B2
0.25	0.45	61.0	0.13	1.1e+10	
0.20	0.67	62.6	0.03	1.8e+11	B9
0.67	0.93	66.0	0.18	1.5e+10	B10
0.27	1.11	78.7	0.23	3.7e+09	B11
0.22	1.36	66.6	0.25	2.5e+09	B12
0.11	4.05	66.2	0.64	1.9e+08	

Table A.13.: List of parameters for all model-fit components of the 8th 43-GHz BG epoch (2008-06-12, see caption of Tab. A.2), $\chi^2_{\mathrm{red}} = 4.8$

Flux density Jy	Distance [mas]	P.A. [°]	b_{maj} [mas]	T_{b} [K]	Name
1.14	0.00	0.0	0.09	1.1e+11	B1
0.47	0.15	44.9	0.12	2.3e+10	B2
0.42	0.47	61.0	0.25	4.6e+09	B14
0.28	0.84	60.9	0.16	7.3e+09	B9
0.49	1.08	65.9	0.15	1.6e+10	B10
0.31	1.21	77.8	0.23	4.0e+09	B11
0.19	1.45	65.3	0.23	2.5e+09	B12
0.18	3.90	66.3	1.17	9.2e+07	

Table A.14.: List of parameters for all model-fit components of the 9th 43-GHz BG epoch (2008-07-06, see caption of Tab. A.2), $\chi^2_{\mathrm{red}} = 4.0$

Flux density Jy	Distance [mas]	P.A. [°]	b_{maj} [mas]	T_{b} [K]	Name
0.80	0.00	0.0	0.08	8.4e+10	B1
0.65	0.11	56.7	0.09	5.8e+10	B2
0.46	0.37	55.2	0.18	9.5e+09	
0.42	0.69	62.7	0.23	5.6e+09	B14
0.24	1.06	61.8	0.22	3.5e+09	B9
0.28	1.26	65.8	0.13	1.1e+10	B10
0.36	1.35	76.1	0.24	4.5e+09	B11
0.17	1.62	64.2	0.25	1.9e+09	B12
0.08	3.90	67.6	0.61	1.5e+08	B15
0.07	4.71	66.3	0.16	1.9e+09	B16

Table A.15.: List of parameters for all model-fit components of the 10th 43-GHz BG epoch (2008-08-15, see caption of Tab. A.2), $\chi^2_{\mathrm{red}} = 4.9$

Flux density Jy	Distance [mas]	P.A. [°]	b_{maj} [mas]	T_{b} [K]	Name
0.70	0.00	0.0	0.07	9.1e+10	B1
0.70	0.10	60.6	0.08	8.4e+10	B2
0.38	0.38	56.1	0.17	9.4e+09	B19
0.27	0.65	61.9	0.19	5.4e+09	
0.20	0.94	63.4	0.20	3.4e+09	B14
0.40	1.33	64.5	0.27	3.7e+09	B10
0.30	1.46	75.5	0.23	4.0e+09	B11
0.10	1.73	64.3	0.17	2.4e+09	B12
0.06	3.90	67.6	0.62	1.1e+08	B15
0.07	4.83	66.3	0.25	7.6e+08	B16

Table A.16.: List of parameters for all model-fit components of the 11th 43-GHz BG epoch (2008-09-10, see caption of Tab. A.2), $\chi^2_{\mathrm{red}} = 2.7$

Flux density Jy	Distance [mas]	P.A. [°]	b_{maj} [mas]	T_{b} [K]	Name
1.09	0.00	0.0	0.05	3.6e+11	B1
2.25	0.11	61.3	0.03	1.6e+12	B2
1.18	0.19	60.1	0.04	4.2e+11	B20
0.22	0.40	57.7	0.10	1.6e+10	B17
0.13	0.57	60.7	0.10	8.7e+09	B18
0.17	0.81	60.3	0.22	2.6e+09	B19
0.17	1.29	62.9	0.18	3.5e+09	B14
0.27	1.68	66.1	0.28	2.5e+09	B10
0.24	1.71	75.8	0.24	2.9e+09	B11
0.07	1.99	63.9	0.23	1.0e+09	B12
0.05	4.34	67.1	0.50	1.5e+08	B15
0.03	5.20	66.7	0.13	1.2e+09	B16

Table A.17.: List of parameters for all model-fit components of the 12th 43-GHz BG epoch (2008-11-16, see caption of Tab. A.2), $\chi^2_{\mathrm{red}} = 2.3$

Flux density Jy	Distance [mas]	P.A. [°]	b_{maj} [mas]	T_{b} [K]	Name
0.31	0.00	0.0	0.05	7.5e+10	B1
1.34	0.09	66.1	0.10	9.4e+10	B2
1.47	0.30	60.1	0.10	9.7e+10	B20
0.23	0.54	60.7	0.17	5.7e+09	B17
0.11	0.77	59.8	0.15	3.3e+09	B18
0.09	1.04	62.7	0.25	1.0e+09	B19
0.12	1.46	63.8	0.27	1.2e+09	B14
0.22	1.85	75.2	0.24	2.7e+09	B11
0.13	1.86	65.4	0.20	2.3e+09	B10
0.05	2.13	64.6	0.13	1.9e+09	B12
0.03	4.38	67.4	0.48	9.4e+07	B15
0.02	5.36	66.9	0.25	2.5e+08	B16

Table A.18.: List of parameters for all model-fit components of the 13th 43-GHz BG epoch (2008-12-21, see caption of Tab. A.2), $\chi^2_{\mathrm{red}} = 1.1$

Flux density Jy	Distance [mas]	P.A. [°]	b_{maj} [mas]	T_{b} [K]	Name
0.79	0.00	0.0	0.06	1.6e+11	B1
1.03	0.10	62.9	0.05	2.4e+11	B2
0.62	0.31	57.8	0.06	1.1e+11	
1.09	0.43	61.3	0.08	1.2e+11	B20
0.32	0.62	63.8	0.17	7.3e+09	B17
0.08	0.96	60.1	0.19	1.5e+09	B18
0.07	1.25	63.5	0.17	1.6e+09	B19
0.54	1.92	70.3	0.45	1.9e+09	
0.06	4.61	66.9	0.62	1.0e+08	B15
0.02	5.42	66.4	0.21	3.3e+08	B16

Table A.19.: List of parameters for all model-fit components of the 14th 43-GHz BG epoch (2009-01-24, see caption of Tab. A.2), $\chi^2_{\mathrm{red}} = 2.6$

Flux density Jy	Distance [mas]	P.A. [°]	b_{maj} [mas]	T_{b} [K]	Name
0.46	0.00	0.0	0.04	2.1e+11	B1
0.96	0.12	62.0	0.04	3.7e+11	B2
0.33	0.28	61.9	0.10	2.4e+10	
0.69	0.47	60.4	0.08	7.2e+10	
0.76	0.61	63.8	0.08	8.8e+10	B20
0.23	0.78	63.0	0.17	5.8e+09	B17
0.06	1.04	62.5	0.18	1.3e+09	B18
0.07	1.45	63.3	0.24	8.9e+08	B19
0.13	2.02	76.4	0.21	2.0e+09	B11
0.36	2.10	67.6	0.40	1.6e+09	B10
0.06	4.70	66.9	0.70	8.8e+07	B15
0.02	5.69	66.4	0.15	4.6e+08	B16

Table A.20.: List of parameters for all model-fit components of the 15th 43-GHz BG epoch (2008-02-22, see caption of Tab. A.2), $\chi^2_{\mathrm{red}} = 1.0$

B. Evolution of the Radio Light Curve

The F-Gamma program provides flux density measurements between 2.64 GHz and 43.05 GHz using the Effelsberg 100-m telescope and at 86 GHz, 142 GHz obtained with the IRAM 30-m antenna (Angelakis et al. (2012)). The authors of this paper classified 3C111 as type 3b in their proposed scheme based on 4.5 yrs of measurements. This type is characterized by a quasi-constant flux at the lowest frequencies and the maximum flux being comparable to the amplitude at the lowest frequency. The spectrum shows variability and a convex distribution between the lowest frequency and the highest frequency peak. Due to the variability the slope can become almost constant after the lowest flux turnover frequency in a state of low activity. The flux after the maximum amplitude frequency seems to be either holding or decreasing (Fig. B.1).

In Fig. B.2 the temporal evolution of the light curve of 3C111 between 32.00 142.33 is displayed based on F-Gamma data. Whereas, the bottom panel in Fig. B.3 shows the light curve from Chatterjee et al. (2011). The data were obtained with the 26 m dish at the Radio Astronomy Observatory of the University of Michigan (14.5 GHz), 13.7 m telescope of the Metsähovi Radio Observatory (37 GHz) and the Submillimeter Array (SMA, $^{230}/\text{GHz}$). Fig B.2 shows the outburst clearly exceeding the low-state flux by a factor of ~ 3, peaking first and highest at the highest frequency, while the maximum amplitude is lower at higher wavelengths. This behaviour is not entirely confirmed by Fig. B.3. Although the outburst occurs first at the highest frequency and the scale and timing at 230 GHz and 14.5 GHzis consistent, the 37 GHz flux exceeds the 32 GHz flux of the F-Gamma program by ~ 3 Jy. The F-Gamma data seems to show a slightly different behaviour.

Chatterjee et al. (2011) suggested that the delay between 37 GHz 230 GHz comes from the larger optical depth at lower frequencies. They interpreted the amplitude and distribution of the light curve in terms of the synchrotron-loss stage of the shock-in-jet model by Marscher & Gear (1985), which predicts the maximum amplitude to remain approximately constant with frequency.

Another problem with the interpretation of the light curve is the location of the detected emission in 3C111. Since the angular resolution of the telescopes is very high, it is likely that emission from the radio lobes contribute to the flux (see Fig. 2.4, C. Grossberger private communication).
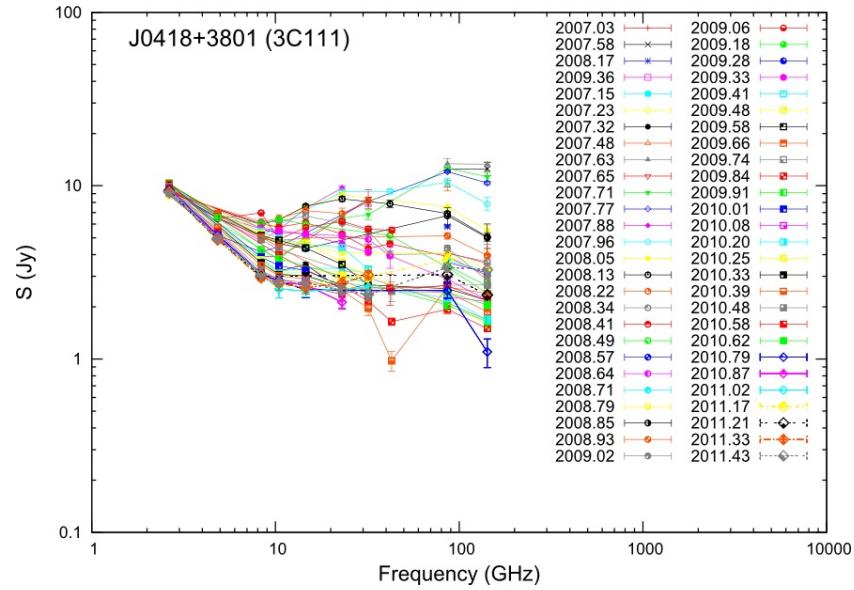
Figure B.1.: Spectrum of 3C111 of the F-GAMMA monitoring programm from Angelakis et al. (2012)
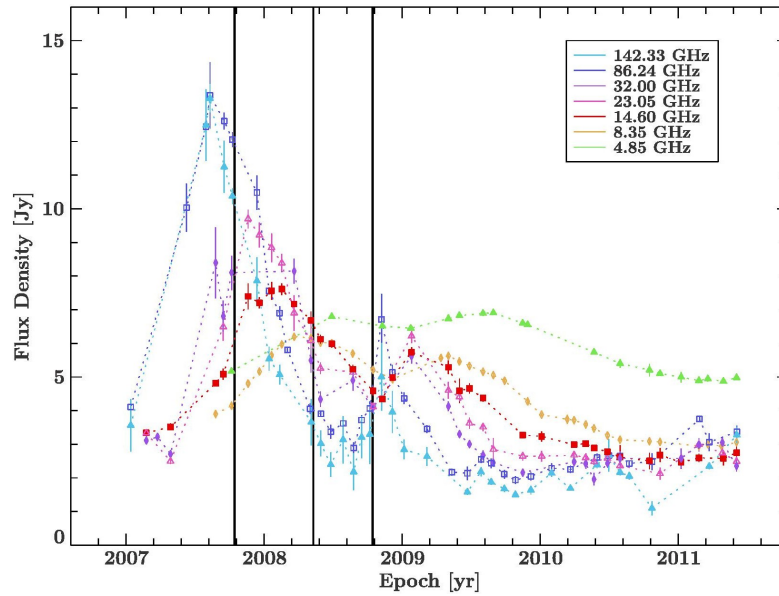
Figure B.2.: Radio light curve of 3C111 with vertical lines indicating the time of observation of the GMVA, Image by C. Grossberger, data from the F-GAMMA monitoring program
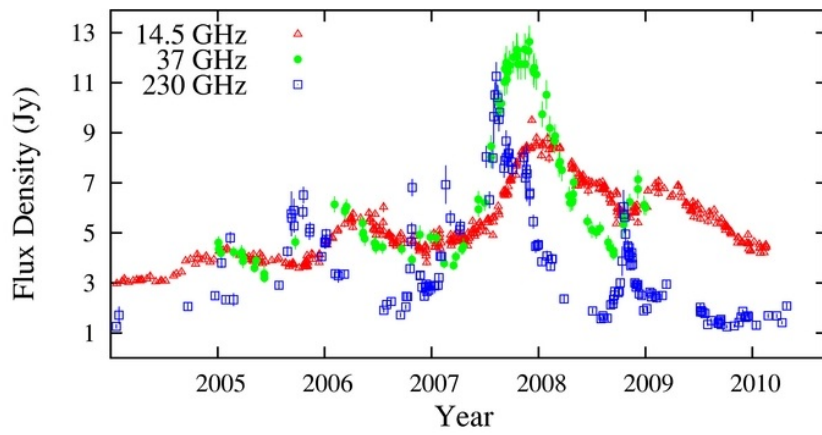
Figure B.3.: Radio light curve of 3C111 at 14.5 GHz, 37 GHz and 230 GHz (bottom panel of Fig. 4 in Chatterjee et al. 2011)

List of Figures

List of Tables

Bibliography

Abdo A.A., Ackermann M., Ajello M., et al., 2010, ApJS 188, 405

Abdo A.A., Ackermann M., Ajello M., et al., 2009a, ApJ 699, 976

Abdo A.A., Ackermann M., Ajello M., et al., 2009b, ApJL 707, L142

Agudo I., Bach U., Krichbaum T.P., et al., 2007, A&A 476, L17

Alef W., Preuss E., Kellermann K.I., Gabuzda D., 1998, In: Zensus J.A., Taylor G.B., Wrobel J.M. (eds.) IAU Colloq. 164: Radio Emission from Galactic and Extragalactic Compact Sources, Vol. 144. Astron. Soc. Pacific, Conf. Ser., p. 129

Aloy M.Á., Martí J.M., Gómez J.L., et al., 2003, ApJL 585, L109

Angelakis E., Fuhrmann L., Nestoras I., et al., 2012, Journal of Physics Conference Series 372, 012007

Antonucci R., 1993, ARA&A 31, 473

Antonucci R.R.J., Miller J.S., 1985, ApJ 297, 621

Begelman M.C., Blandford R.D., Rees M.J., 1984, Rev. Mod. Phys. 56, 255

Bennett A.S., 1962, Mem. R. Astron. Soc. 68, 163

Blandford R.D., Königl A., 1979, ApJ 232, 34

Blandford R.D., Payne D.G., 1982, MNRAS 199, 883

Blandford R.D., Znajek R.L., 1977, MNRAS 179, 433

Bolton J.G., Stanley G.J., Slee O.B., 1949, Nat 164, 101

Burke B.F., Graham-Smith F., 2010, An Introduction to Radio Astronomy, Cambridge University Press

Chatterjee R., Marscher A.P., Jorstad S.G., et al., 2011, ApJ 734, 43

Colina L., Perez-Fournon I., 1990, ApJS 72, 41

Cotton W.D., 1995, In: Zensus J.A., Diamond P.J., Napier P.J. (eds.) Very Long Baseline Interferometry and the VLBA, Vol. 82. Astron. Soc. Pacific, Conf. Ser., p. 189

Doeleman S., 2008, Journal of Physics Conference Series 131, 012055

Doeleman S.S., Weintroub J., Rogers A.E.E., et al., 2008, Nat 455, 78

Eckart A., Genzel R., 1996, Nat 383, 415

Eracleous M., Halpern J.P., 2004, ApJS 150, 181

Fanaroff B.L., Riley J.M., 1974, MNRAS 167, 31P

Ghez A.M., Morris M., Becklin E.E., et al., 2000, Nat 407, 349

Götz M.M.A., Alef W., Preuss E., Kellermann K.I., 1987, A&A 176, 171

Grandi P., Torresi E., Stanghellini C., 2012, ApJL 751, L3

Grossberger C., Kadler M., Wilms J., et al., 2012, Acta Polytechnica 52, 010000

Hada K., Doi A., Kino M., et al., 2011, Nat 477, 185

Hardee P.E., 2006, In: Miller H.R., Marshall K., Webb J.R., Aller M.F. (eds.) Blazar Variability Workshop II: Entering the GLAST Era, Vol. 350. Astron. Soc. Pacific, Conf. Ser., p. 205

Hartman R.C., Bertsch D.L., Bloom S.D., et al., 1999, ApJS 123, 79

Hartman R.C., Kadler M., Tueller J., 2008, ApJ 688, 852

Haslam C.G.T., Salter C.J., Stoffel H., Wilson W.E., 1982 47, 1

Hewish A., Bell S.J., Pilkington J.D.H., et al., 1968, Nat 217, 709

Högbom J.A., 1974, A&AS 15, 417

Hogbom J.A., 1979, A&AS 36, 173

Jansky K.G., 1933, Nat 132, 66

Jorstad S.G., Marscher A.P., Lister M.L., et al., 2005, AJ 130, 1418

Kadler M., Krichbaum T.P., Ros E., et al., 2007, 3C 111 in Outburst (Target of Oportunity), GMVA ToO Proposal

Kadler M., Ros E., Perucho M., et al., 2008, ApJ 680, 867

Kataoka J., Stawarz Ł., Takahashi Y., et al., 2011, ApJ 740, 29

Kellermann K.I., Kovalev Y.Y., Lister M.L., et al., 2007, Ap&SS 311, 231

Kellermann K.I., Lister M.L., Homan D.C., et al., 2004, ApJ 609, 539

Khachikyan É.Y., Weedman D.W., 1971, Astrophysics 7, 231

Kharb P., Gabuzda D., Alef W., et al., 2003 47, 621

Komossa S., Voges W., Xu D., et al., 2006, AJ 132, 531

Kovalev Y.Y., Kellermann K.I., Lister M.L., et al., 2005, AJ 130, 2473

Kovalev Y.Y., Lobanov A.P., Pushkarev A.B., Zensus J.A., 2008, A&A 483, 759

Krolik J.H., 1999, Active galactic nuclei : from the central black hole to the galactic environment, Princeton University Press

Laing R.A., Bridle A.H., 2002, MNRAS 336, 328

Laing R.A., Bridle A.H., Parma P., et al., 2008, MNRAS 386, 657

Leahy J.P., Black A.R.S., Dennett-Thorpe J., et al., 1997, MNRAS 291, 20

Lee S.S., Lobanov A.P., Krichbaum T.P., et al., 2008, AJ 136, 159

Levenberg K., 1944, Quarterly of Applied Mathematics 2 164

Lewis K.T., Eracleous M., Gliozzi M., et al., 2005, ApJ 622, 816

Lind K.R., Blandford R.D., 1985, ApJ 295, 358

Linfield R., 1987, ApJ 317, 121

Linfield R., Perley R., 1984, ApJ 279, 60

Lister M.L., Cohen M.H., Homan D.C., et al., 2009, AJ 138, 1874

Lobanov A.P., 1998, A&A 330, 79

Lobanov A.P., Krichbaum T.P., Graham D.A., et al., 2000, A&A 364, 391

Longair M.S., 2011, High Energy Astrophysics, Cambridge University Press

Longair M.S., Gunn J.E., 1975, MNRAS 170, 121

Mackay C.D., 1969, MNRAS 145, 31

Marscher A.P., 2006, Astron. Nachr. 327, 217

Marscher A.P., 2009, ArXiv e-prints 0909.2576

Marscher A.P., Gear W.K., 1985, ApJ 298, 114

Marshall F.E., Mushotzky R.F., Boldt E.A., et al., 1978, Nat 275, 624

Martel A.R., Baum S.A., Sparks W.B., et al., 1999, ApJS 122, 81

Martí-Vidal I., Krichbaum T.P., Marscher A., et al., 2012, A&A 542, A107

Miller J.S., 1994, In: Bicknell G.V., Dopita M.A., Quinn P.J. (eds.) The Physics of Active Galaxies, Vol. 54. Astron. Soc. Pacific, Conf. Ser., p. 149

Mitton S., 1970, Astrophy. Letters 6, 161

Müller C., Kadler M., Ojha R., et al., 2011, A&A 530, L11

Nolan P.L., Abdo A.A., Ackermann M., et al., 2012, ApJS 199, 31

NRAO 2011, AIPS COOKBOOK available from http://www.aips.nrao.edu/CookHTML/CookBook.html

Pauliny-Toth I.I.K., Preuss E., Witzel A., et al., 1976, A&A 52, 471

Pearson T.J., 1995, In: Zensus J.A., Diamond P.J., Napier P.J. (eds.) Very Long Baseline Interferometry and the VLBA, Vol. 82. Astron. Soc. Pacific, Conf. Ser., p. 268

Pearson T.J., Readhead A.C.S., 1984, ARA&A 22, 97

Penzias A.A., Wilson R.W., 1965, ApJ 142, 419

Perucho M., Agudo I., Gómez J.L., et al., 2008, A&A 489, L29

Preuss E., Alef W., Kellermann K.I., 1988, In: Reid M.J., Moran J.M. (eds.) The Impact of VLBI on Astrophysics and Geophysics, Vol. 129. IAU Symposium, p. 105

Pudritz R.E., Hardcastle M.J., Gabuzda D.C., 2012, Space Sci. Rev. 41

Rantakyro F.T., Baath L.B., Backer D.C., et al., 1998, A&AS 131, 451

Reber G., 1988, J. Roy. Astron. Soc. Can. 82, 93

Rees M.J., 1966, Nat 211, 468

Reynolds C.S., Iwasawa K., Crawford C.S., Fabian A.C., 1998, MNRAS 299, 410

Rybicki G.B., Lightman A.P., 1979, Radiative processes in astrophysics, New York, Wiley-Interscience

Sargent W.L.W., 1977, ApJL 212, L105

Schmidt M., 1963, Nat 197, 1040

Schneider P., 2008, Einführung in die extragalaktische Astronomie und Kosmologie, Springer Berlin

Schwab F.R., Cotton W.D., 1983, AJ 88, 688

Seyfert C.K., 1943, ApJ 97, 28

Sguera V., Bassani L., Malizia A., et al., 2005, A&A 430, 107

Shepherd M.C., 1997, In: Hunt G., Payne H. (eds.) Astronomical Data Analysis Software and Systems VI, Vol. 125. Astron. Soc. Pacific, Conf. Ser., p. 77

Shepherd M.C., Pearson T.J., Taylor G.B., 1994, In: BAAS, Vol. 26. BAAS, p.987

Shields G.A., 1999, ArXiv e-prints astro-ph/9903401

Taylor G., 1997, The Difmap Cookbook available from ftp://ftp.astro.caltech.edu/pub/difmap/cookbook.ps.Z

Taylor G.B., Carilli C.L., Perley R.A., (eds.) 1999, Synthesis Imaging in Radio Astronomy II, Vol. 180 of *Astron. Soc. Pacific, Conf. Ser.*, Astron. Soc. Pacific, Conf. Ser.

Thompson A.R., Moran J.M., Swenson, Jr. G.W., 2001, Interferometry and Synthesis in Radio Astronomy, 2nd Edition, New York : Wiley

Tombesi F., Sambruna R.M., Marscher A.P., et al., 2012, ArXiv e-prints

Trippe S., Krips M., Piétu V., et al., 2011, A&A 533, A97

Walker R.C., 1989, In: Perley R.A., Schwab F.R., Bridle A.H. (eds.) Synthesis Imaging in Radio Astronomy, Vol. 6. Astron. Soc. Pacific, Conf. Ser., p. 355

Whitney A.R., Shapiro I.I., Rogers A.E.E., et al., 1971, Sci 173, 225

Wilkes B., 2004, In: Richards G.T., Hall P.B. (eds.) AGN Physics with the Sloan Digital Sky Survey, Vol. 311. Astron. Soc. Pacific, Conf. Ser., p. 37

Wills B.J., 1975, ApJL 202, L59

Wozniak P.R., Zdziarski A.A., Smith D., et al., 1998, MNRAS 299, 449

Wyndham J.D., 1966, ApJ 144, 459

Danksagung

Im Folgenden möchte ich mich bei allen Menschen bedanken, die zum Gelingen dieser Masterarbeit beigetragen haben.

Zu Beginn geht ein herzliches Dankeschön an Prof. Dr. Matthias Kadler für die Bereitstellung und Betreuung dieses spannenden Projektes, bei der er mir stets mit Rat und Tat zur Seite stand. Darüber hinaus danke ich ihm dafür, dass er meine Neugier für die Radioastronomie geweckt hat und für seine unermütliche Hilfe bei meinen ersten Schritten in der Welt des VLBI. Seine Förderung ermöglichte es mir frühzeitig auch in weiteren aktuellen Projekte mitzuwirken und so einen Platz in seiner Arbeitsgruppe finden zu können.

Ich bedanke mich bei Prof. Dr. Karl Mannheim für die Übernahme des Zweitgutachtens und die Unterstützung, die ich seit dem Beginn meiner Mitarbeit am Lehrstuhl mit meiner Bachelorarbeit erfahren habe.

Dr. Thomas Krichbaum vom Max-Planck-Institut für Radioastronomie in Bonn danke ich für die Zeit, die er sich für mich in Bonn genommen hat, um mir die A-priori Kalibrierung der GMVA Daten in AIPS zu zeigen und für die Fertigstellung dieser Kalibrierung sowie für die Hinweise in der Interpretation der Daten.

Ich bedanke mich vielmals bei Prof. Dr. Eduardo Ros für die vielen Ratschläge zu meinem ersten Proposal als PI, welches auf den Ergebnissen dieser Arbeit beruht, und die unkomplizierte Zusammenarbeit bei weiteren Projekten noch bevor wir uns das erste Mal persönlich getroffen haben.

Ein ganz besonderer Dank geht auch an die "Bamberger Connection" von der Dr. Karl Remeis Sternwarte Bamberg, die nicht ausschließlich auf die berufliche Ebene beschränkt ist. Allen voran danke ich Cornelia Müller für die vielen Hinweise und Diskussionen rund um VLBI und die vielen Korrekturen, die sie zu meiner Arbeit beigetragen hat. Ich bedanke mich vielmals bei Christoph Grossberger für die ausgedehnten Gespräche zum Thema VLBI und 3C111, sowie die Bereitstellung von ausführlichen ISIS-Scripten. Darüber hinaus gilt mein Dank Tobias Beuchert, Moritz Boeck und Anne-Kathrin Bazcko. Ich bedanke mich außerdem bei allen Bambergern für die Einführung von ISIS am Lehrstuhl, welches für mich nicht mehr von hier wegzudenken ist.

Mein Dank gilt außerdem Marcus Langejahn und Jonas Trüstedt von nebenan für die vielen Diskussion weit über das Thema dieser Arbeit hinaus.

Eigenständigkeitserklärung

Hiermit bestätige ich, Robert Frank Schulz, dass ich die vorliegende Arbeit selbstständig verfasst und keine anderen als die angegebenen Hilfsmittel benutzt habe. Die Stellen der Arbeit, die dem Wortlaut oder dem Sinn nach anderen Werken entnommen sind, wurden von mir unter Angabe der Quelle kenntlich gemacht.

....

Ort, Datum   Unterschrift